UNIVERSITY OF CALIFORNIA SAN DIEGO

Integration of atomically thin transition metal dichalcogenides for nanophotonic and biosensing applications

A Dissertation submitted in partial satisfaction of the requirements
for the degree Doctor of Philosophy

in

Nanoengineering

by

Chawina De-Eknamkul

Committee in charge:

Professor Ertugrul Cubukcu, Chair
Professor Prabhakar Bandaru
Professor Zhaowei Liu
Professor Donald Sirbuly
Professor Oscar Vazquez-Mena

2022

The Dissertation of Chawina De-Eknamkul is approved, and it is acceptable in quality and form for publication on microfilm and electronically.

University of California San Diego

2022

DEDICATION

To my parents, my sister, my grandmother, and Josh.

TABLE OF CONTENTS

LIST OF FIGURES

ACKNOWLEDGEMENTS

I am deeply grateful to my advisor and committee chair, Dr. Ertugrul Cubukcu, for sharing his expertise and providing support throughout my PhD program. Through his guidance and advice, I have acquired a wide range of research skills and grown into a well-rounded engineer. I would like to extend my gratitude to Dr. Duygu Kuzum for her direction and insights in our collaborated work. Finally, I would like to thank my committee members, Dr. Prabhakar Bandaru, Dr. Zhaowei Liu, Dr. Donald Sirbuly, and Dr. Oscar Vazquez-Mena for their time and support throughout the program.

My projects would not have been possible without the help of past and current Cubukcu lab members, Wenzhuo Huang, Xingwang Zhang, Yundong Ren, Eric Lee-Wang and Shinhyuk Choi. I would also like to acknowledge members of Kuzum lab, Jeonghoon Kim and Madison Wilson for their collaboration.

Chapter 2, in part, is currently being prepared for submission for publication of the material as it appears in Directional propagation of self-resonant exciton-polariton in atomically thin tungsten disulfide waveguide. De-Eknamkul, Chawina; Huang, Wenzhuo; Zhang, Xingwang; Cubukcu, Ertugrul. 2022. The dissertation author was the primary investigator and author of this material.

Chapter 3, in full, is a reprint of the material as it appears in MoS_2-enabled dual-mode optoelectronic biosensor using a water soluble variant of μ-opioid receptor for opioid peptide detection. De-Eknamkul, Chawina; Zhang, Xingwang; Zhao, Meng-Qiang; Huang, Wenzhuo; Liu, Renyu; Johnson, A. T. Charlie; Cubukcu, Ertugrul. 2D Materials, 2020. The dissertation author was the primary researcher and author of this paper.

Chapter 4, in part, is currently being prepared for submission for publication of the material as it appears in Optical voltage sensing of electrophysiological signals with monolayer MoS_2. De-Eknamkul, Chawina; Kim, Jeonghoon; Huang, Wenzhuo; Ren, Yundong; Wilson, Madison; Puppo, Francesca; Patne, Meenashki; Muotri, Alysson R.; Kuzum, Duygu; Cubukcu, Ertugrul. The dissertation author and Jeonghoon Kim were the primary investigator and author of this material.

VITA

2015 Bachelor of Science in Chemical Engineering, University of California Los Angeles
2018 Master of Science in Nanoengineering, University of California San Diego
2022 Doctor of Philosophy in Nanoengineering, University of California San Diego

PUBLICATIONS

Chawina De-Eknamkul, Jeonghoon Kim, Wenzhuo Huang, Yundong Ren, Madison Wilson, Francesca Puppo, Meenashki Patne, Alysson R. Muotri, Duygu Kuzum, and Ertugrul Cubukcu. "Optical voltage sensing of electrophysiological signals with monolayer MoS_2." In preparation.

Chawina De-Eknamkul, Wenzhuo Huang, Xingwang Zhang, and Ertugrul Cubukcu. "Directional propagation of self-resonant exciton-polariton in atomically thin tungsten disulfide waveguide." In preparation.

Xingwang Zhang, Wenzhuo Huang, **Chawina De-Eknamkul**, Kedi Wu, Meng-qiang Zhao, Sefaattin Tongay, Alan T. Charlie Johnson, and Ertugrul Cubukcu. 2021. "Azimuthally Polarized and Unidirectional Excitonic Emission from Deep Subwavelength Transition Metal Dichalcogenide Annular Heterostructures." ACS Photonics. 8: 2861-2867. doi: 10.1021/acsphotonics.1c01033.

Chawina De-Eknamkul, Xingwang Zhang, Meng-Qiang Zhao, Wenzhuo Huang, Renyu Liu, A. T. Charlie Johnson, and Ertugrul Cubukcu. 2020. "MoS2-Enabled Dual-Mode Optoelectronic Biosensor Using a Water Soluble Variant of Mu-Opioid Receptor for Opioid Peptide Detection." 2D Materials. 7: 014004. doi: 10.1088/2053-1583/ab5ae2.

David Ding, Yichen Lu, Ruoyu Zhao, Xin Liu, **Chawina De-Eknamkul**, Chi Ren, Armaghan Mehrsa, Takaki Komiyama, and Ertugrul Cubukcu. 2020. "Evaluation of Durability of Transparent Graphene Electrodes Fabricated on Different Flexible Substrates for Chronic In Vivo Experiments." IEEE Transactions on Biomedical Engineering, vol. 67, no. 11, pp. 3203-3210. doi: 10.1109/TBME.2020.2979475.

Xingwang Zhang, **Chawina De-Eknamkul**, Jie Gu, Alexandra L Boehmke, Vinod M Menon, Jacob Khurgin, and Ertugrul Cubukcu. 2019. "Guiding of Visible Photons at the Ångström Thickness Limit." Nature Nanotechnology. 14: 844-850. doi:10.1038/s41565-019-0519-6.

Wenzhuo Huang, **Chawina De-Eknamkul**, Xingwang Zhang, Eric Leewong, and Meng-qiang Zhao, A. T. Charlie Johnson,and Ertugrul Cubukcu. 2019. "Monolayer Excitonic Emission for Imaging Spatial Dispersion of Photonic Crystals." ACS Photonics. 6: 2312–19. doi:10.1021/acsphotonics.9b00820.

Xingwang Zhang, Nicolas Biekert, Shinhyuk Choi, Carl H Naylor, **Chawina De-Eknamkul**, Wenzhuo Huang, Xiaojie Zhang, Xiaorui Zheng, Dake Wang, A T Charlie Johnson, and Ertugrul Cubukcu. 2018. "Dynamic Photochemical and Optoelectronic Control of Photonic Fano Resonances via Monolayer MoS_2 Trions." Nanoletters. 18: 957–63. doi:10.1021/acs.nanolett.7b04355

ABSTRACT OF THE DISSERTATION

Integration of atomically thin transition metal dichalcogenides for nanophotonic and biosensing applications

by

Chawina De-Eknamkul

Doctor of Philosophy in Nanoengineering

University of California San Diego, 2022

Professor Ertugrul Cubukcu, Chair

Atomically thin transition metal dichalcogenides (TMDCs), such as MoS_2 and WS_2, are two-dimensional layered semiconductors that exhibit a unique combination of electronic and optical properties, lattice structure, mechanical stability, biocompatibility, and large specific

surface area. Because of the large direct bandgap and 2D confinement, charge carriers in TMDCs experience enhanced electrostatic interactions and can respond strongly to incident light despite the materials' atomically thin form factor. This phenomenon gives TMDCs a range of unusual optical characteristics, such as high absorption, tunable photoluminescence emission, and large refractive indices in the visible spectrum. As promising materials with diverse properties, TMDCs have been integrated into nanoscale platforms to enable unprecedented performance and functionalities unattainable by traditional materials.

This dissertation explores the function of few-layer and monolayer TMDCs in nanophotonic and biosensing platforms. In chapter 2, I discuss the light-matter interaction in an atomically thin three-layer WS_2 waveguide that enables external control over light propagation direction. Chapters 3 and 4 examine the roles of monolayer MoS_2 as an active biosensing element. In chapter 3, I discuss the development of a dual-mode optoelectronic biosensor based on monolayer molybdenum disulfide (MoS_2) capable of producing simultaneous electrical and optical readouts of biomolecular signals. The integration of electrical and optical sensors on the same chip can offer flexibility in read-out and improve the accuracy in detection of low concentration targets. Chapter 4 presents a novel monolayer MoS_2-based platform as a label-free approach for optical electrophysiology. I discuss how susceptibility of MoS_2 excitons to charges can be utilized to convert electrical activity into photoluminescence signals. This first work investigates MoS_2's voltage-tunable photoluminescence, fluorescence imaging capability, photostability and biocompatibility with neuron cultures. Results demonstrate the feasibility of this approach for recording millisecond-scale neuronal action potentials.

CHAPTER 1 - INTRODUCTION

1.1 Background

Single layer transition metal dichalcogenides (TMDCs), such as molybdenum sulfide (MoS_2) and tungsten disulfide (WS_2), are among the thinnest semiconductors that possess a unique combination of inherent characteristics that are not found in their bulk layered counterparts. Despite being less than one nanometer thick, monolayer MoS_2 and WS_2 can interact strongly with visible light due to the presence of an optical bandgap that emerges from the in-plane quantum confinement effects. Their two-dimensionality further makes their optical, electrical, and optoelectronic properties sensitive to a wide range of external stimuli, such as light, electric fields, charge density and dielectric environment. Because of these fascinating properties, studies of atomically thin TMDCs have tremendously grown over the last decade as researchers began to explore these materials in a variety of novel nanoscale platforms. In this dissertation, I characterized the light-matter interactions in monolayer WS_2 waveguides (chapter 2) and studied the monolayer MoS_2's tunable optical properties towards multimodal biosensing applications (chapters 3 and 4).

1.2 Structure of two-dimensional TMDCs

MoS_2 and WS_2 belongs in the TMDC family characterized by the chemical formula MX_2. M is a transition metal from group VI elements of the periodic table such as molybdenum (Mo) and tungsten (W), and X is a chalcogen such as sulfur (S) and selenium (Se). Structurally, TMDCs are layered crystal with strong intralayer bonds and weaker interlayer van der Waals attraction. Each layer consists of covalently bonded X-M-X units that form a three-atom-thick hexagonal sheet (Figure 1.1).

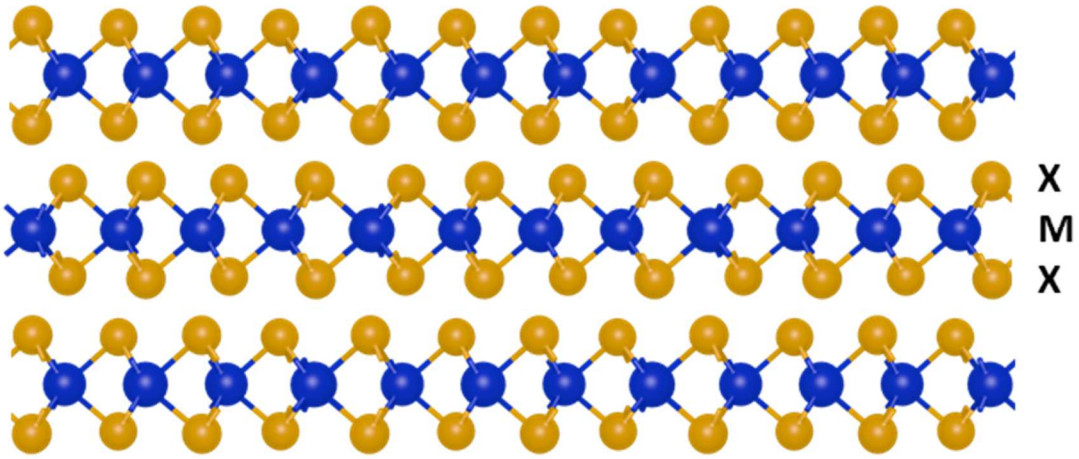

Figure 1.1: Crystal structure of layered TMDC.
Group VI transition metal (M = Mo, W) and chalcogen (X = S, Se) atoms are shown in blue and yellow, respectively.

1.3 Layer-dependent photoluminescence

One of the most intriguing optical properties of 2D TMDCs is the layer-dependent photoluminescence (PL) emission. Figure 1.2 shows the characteristics PL spectra of mechanically exfoliated WS_2 regions with decreasing number of layers down to the monolayer limit. Four-layer WS_2 shows two distinct emission peaks 630 nm and ~850 nm, corresponding to at direct and indirect band gap transitions, respectively. As the number of layers is reduced, the material band structure changes dramatically. The indirect band gap grows, shifting the indirect emission peak towards higher energy. At monolayer thickness, WS_2 (and other TMDCs) becomes a direct band gap semiconductor and emits one single PL peak at 620 nm with increased quantum yield of several orders of magnitude larger than the bulk counterpart.[1] This intrinsic indirect-to-direct transition mechanism is unique to TMDCs and not observed in other low dimensional semiconductors.[2]

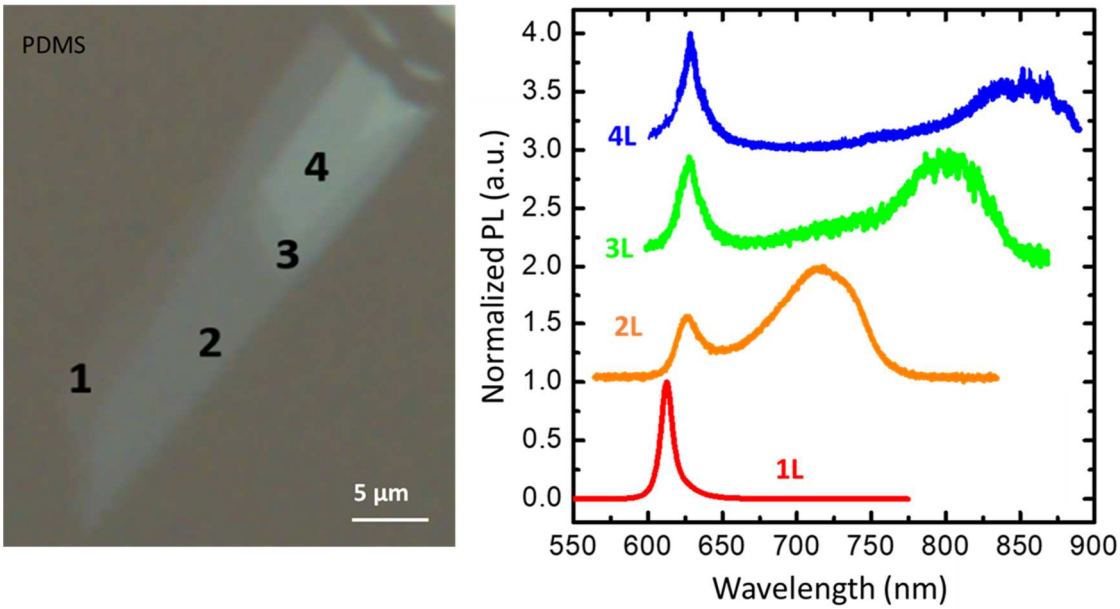

Figure 1.2: Tungsten disulfide thickness-dependent photoluminescence.
PL spectra (right) of a mechanically exfoliated WS_2 sample on PDMS (left) as a function of number of layers.

1.4 Excitons in two-dimensional TMDCs

The strong PL emission in monolayer TMDCs originates from the radiative recombination of photo-excited excitons. An exciton is a pair electron and hole that are bound together by the electrostatic Coulomb force. When a material absorbs a photon that is higher energy than its bandgap, an electron is excited to the conduction band and a positively charged hole is created. The photo-generated electron and hole have opposite changes and are, therefore, inherently attracted to each other. In conventional bulk semiconductors, this attraction force is screened by the surrounding charges, resulting in small exciton binding energies that is less than the energy of thermal fluctuations at room temperature. In few-layer and monolayer TMDCs, photo-excited excitons experience significantly reduced dielectric screening as there is less surrounding material which then leads to enhanced Coulomb attraction between excited electron-hole pairs. These excitons are, therefore, said to be strongly bound having large binding energies of hundreds of

meV.[3,4] For this reason, optical properties of 2D TMDCs are heavily dominated by the behaviors of bound excitons observable even at room temperature. The robust excitonic effects account for monolayer TMDCs' large absorption, strong PL emission and high refractive index.

1.5 Trions in two-dimensional TMDCs

Consisting of electrostatically bound electron and hole, excitons have hydrogen-like bound states and can become ionized by gaining an additional electron or hole. Combined with the enhanced Coulomb forces in atomically thin TMDCs, an exciton can bind to a free electron to form a negatively charged exciton known as trion. While a trion can either be positive or negative, monolayer TMDCs like MoS_2 and WS_2 typically form negative trions due to their n-doped nature from intrinsic defects formed during growth. Trion binding energies are 15-45 meV in monolayer TMDCs.[5,6] Compared to exciton, trion emission is lower in energy (redshift) and less luminescent due to the higher effective mass and non-radiative decay pathways. Increased electron density promotes exciton-to-trion conversion and decreases exciton-to-trion ratio upon photoexcitation. This, in turn, leads to an overall reduction in photoluminescence emission intensity.

1.6 Valley polarization and valley coherence in two-dimensional TMDCs

Because of the lack of inversion symmetry in its crystal structure, we have energy-degenerate but inequivalent K and K' points in the reciprocal lattice (Figure 1.3). In the band structure, direct exciton transitions occur at these K and K' valleys. Excitation with left or right hand circularly polarized light results in exciton transitions in one of the valleys, but not the other. The subsequent PL emission from recombination of valley polarized excitons then maintains the same circular polarization as that of the excitation light. Linearly polarized light can be

decomposed into the superposition of two equal-amplitude circularly polarized components. If we have a linearly polarized pump, then we excite excitons from both valleys equally. The excitons maintain a coherent superposition of K and K' states so the subsequent PL emission can be linearly polarized along the same axis as the polarization of excitation. This means that the linear polarization of the pump can be preserved in the excitonic PL emission. This phenomenon is very difficult to observe in a monolayer at room temperature. This is because the valley polarization lifetime is shorter than the exciton lifetime and so intervalley scattering occurs to mix up the polarization. In thicker layers this effect is much more pronounced and can be seen at room temperature.

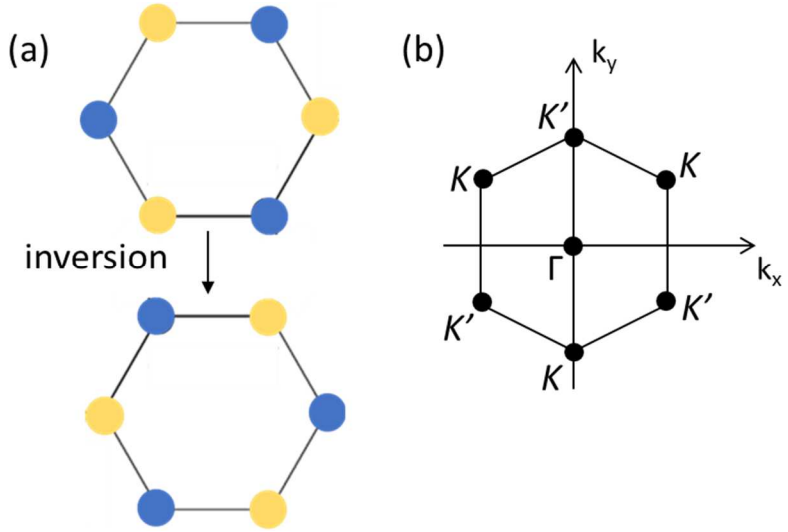

Figure 1.3: Hexagonal lattice symmetry of TMDCs.
(a) Lack of inversion symmetry in TMDC lattice. Blue and yellow circles correspond to transition metal and chalcogen atoms, respectively. (b) Brillouin zone of TMDC lattice with K and K' valleys.

CHAPTER 2 - DIRECTIONAL PROPAGATION OF SELF-RESONANT EXCITON-POLARITON IN ATOMICALLY THIN TUNGSTEN DISULFIDE WAVEGUIDE

2.1 Introduction

In two-dimensional transition-metal dichalcogenides (2D TMDCs), excitons dominate the electromagnetic response in the visible regime due to quantum confinement effects.[4,7] Excitons are pairs of photoexcited electron and hole bound together by electrostatic Coulomb attraction. This interaction is unusually strong in 2D TMDCs as in-plane confinement decreases the average separation between the electron and hole, and the excitons experienced reduced dielectric screening of the low dielectric permittivity environment.[4] These effects lead to large exciton binding energies of hundreds of meV that make the excitonic features observable at room temperature. The large in-plane excitonic dipoles can strongly couple to the continuum of electromagnetic modes to generate hybrid light-matter modes called exciton-polaritons.[8] This distinct hybridization between TMDC excitons and photons brings about unique physical phenomena that are simultaneously photon- and exciton-like, including large propagation distances, long-range coherence, and valley-coherent coupling.[9] The study of TMDC exciton-polaritons promises unprecedented ways to confine and control subwavelength light-matter interaction for nanophotonic applications in the infrared and optical regime.

In our previous work, we experimentally demonstrated guiding of visible light in sub-nanometer thick WS_2 waveguides suspended in air.[10] The guided mode is transverse electric (TE) polarized with electric fields polarized in the plane of the material and evanescent decay in the out-of-plane direction (section 2.4.1). Near the exciton resonance, we expect guided photons to couple with in-plane excitons, producing 2D exciton-polaritons that propagate within the plane of atomically thin WS_2.[11] Because of the hybrid nature of exciton-polariton, we also expect the

waveguide mode in WS_2 to exhibit characteristics of the strongly bound excitons. Several groups have realized TMDCs-embedded photonic cavities and demonstrated that the cavity exciton-polaritons inherit exciton's valley polarization, allowing for manipulation of valley polarization in coherent light and matter states.[12–14] However, the valley degree of freedom in in-plane propagating exciton-polaritons has not yet been explored.

In this work, we investigated the characteristics of 2D propagating exciton-polariton in a three-layer (3L) WS_2 waveguide. We employed a photonic crystal (PhC) structure patterned directly into the suspended WS_2 to enable far-field probing of the dark in-plane modes.[10] The PhC acts as a 2D grating that efficiently couples light in and out of the 2 nm-thick waveguide, allowing us to observe the modes as guided-mode resonances that radiate into free space. Using this approach, we first studied the dispersion and propagation length of exciton-polariton using angle-resolved transmission and back focal plane measurements. We further showed experimentally that the TE-nature of the atomically thin waveguides facilitate the spatial separation of valley-coherent excitons. By coupling to WS_2 excitons, the propagation direction of light can be controlled using the polarization of excitation light.

Excitons in 2D TMDCs exhibit unique valley characteristics because of the 2D hexagonal lattice structure that lacks a spatial inversion symmetry within each TMDC layer. This creates two energy-degenerate K and K' valleys in the first Brillouin zone where direction exciton transitions occur.[15] These two valleys are non-equivalent, as strong spin-orbit coupling in TMDCs leads to spin splitting having opposite signs in each valley. This spin-valley coupling gives rise to a new valley degree of freedom, allowing each valley to be excited by either left- or right-handed (σ^+ or σ^-) circularly polarized light. Depending on the intervalley scattering dynamics and exciton lifetime, the emitted photoluminescence (PL) can bear a large degree of circular polarization, with

few-layer WS_2 exhibiting as high as 90% at cryogenic temperatures and 60% at room temperature.[16,17] More interestingly, several works showed that TMDC excitons also display a degree of valley coherence.[16,18,19] In this case, the linear polarization of the excitation source is preserved in the coherent superposition of K and K' valley-polarized excitons, and the resulting PL emission possesses a preferred direction of linear polarization corresponding to that of the excitation source. Several groups have successfully create chiral interfaces capable of spatially separating excitons based on their valley polarization, creating a pathway to utilizing the valley degree of freedom for information storage and processing.[20–22]

2.2 Results and Discussions

We showed in our previous work that suspending atomically thin WS_2 in air forms a symmetric waveguide structure and allows the material to support guided modes confined to the plane of the waveguide with no cutoff thickness.[23] Suspending the material in air ensures matching refractive indices on both sides, forming a symmetric waveguide that supports exciton-polariton modes (section 2.4.1).[8] The hole array acts as a 2D grating propagating modes and allows a small portion of light to couple out of the plane into free space via momentum matching. Specifically, the introduction of periodic modulation of the refractive index folds the waveguide mode dispersion to the first Brillouin zone, which lies above the light line. The result is a quasi-bound guided-mode resonance characterized by an asymmetric line shape observable in the far field. Figure 2.1a illustrates a square array of air holes etched into the freestanding 2-nm-thick WS_2 supported by a SiN/Si window. The sample can be viewed as a modulated waveguide, where the index difference $\Delta\varepsilon$ determines the strength of modulation. In the case of few-nanometer-thick 3L WS_2 PhC, the modulation is said to be small due to the majority of the mode volume residing in

air.[11] Within the weak modulation PhC limit, the locations of the guided-mode resonances reflect the exciton-polariton resonant dispersion in the corresponding unmodulated slab waveguide (unpatterned WS_2).[24] The mode has an in-plane propagation constant $\beta = n_{eff}k_0$, where n_{eff} is the complex effective mode index, with imaginary part representing the diffraction and absorption losses. Using Rigorous Coupled-Wave Analysis (RCWA, section 2.4.2),[25] we derive the momentum matching conditions for the guided-mode resonance in the XY plane and the in-plane components the free-space wavevector (k_0):

$$\left(n_{eff}\right)^2 = \left(\frac{k_x}{k_0} + m\frac{2\pi}{\Lambda k_0}\right)^2 + \left(\frac{k_y}{k_0} + n\frac{2\pi}{\Lambda k_0}\right)^2, m, n = 0,1,2,\ldots \quad (1)$$

where Λ is the period of modulation, and m and n are the order of space harmonic. From Equation 1, we can see that the guided-mode resonance forms arcs in the back focal plane (momentum space) centered at $\left(-m\frac{2\pi}{\Lambda k_0}, -n\frac{2\pi}{\Lambda k_0}\right)$ with a radius of n_{eff}.

The atomically thin 3L WS_2 flake was patterned and suspended using a novel fabrication technique developed in the previous work (section 2.4.3).[26] Figure 2.1b shows a scanning electron micrograph (SEM) of such suspended 3L WS_2 photonic crystal. The photonic crystal here has a period of 700 nm and hole diameter 340 nm. Figure 2.1c shows the transmission spectrum of the 3L WS_2 photonic crystal at normal incidence. The spectrum shows two distinct peaks at 624 nm and 705 nm, corresponding to A-exciton absorption and guided-mode resonance of the photonic crystal, respectively. Valley coherence in 3L WS_2 PL emission can be observed at room temperature by near-resonance excitation using linearly polarized 594 nm continuous wave laser. To analyze the polarization of the PL emission, we used an analyzer to measure emission spectra polarized parallel (co) and perpendicularly (cross) to the linear polarization of the excitation laser (section 2.4.7). Figure 2.1d shows the measured polarized-resolved PL spectra in blue and orange,

respectively. Each spectrum shows two peaks centered around 630 nm and 785 nm, corresponding to the direct excitonic and indirect bandgap transitions, respectively, which are consistent with the emission of 3L WS_2.[27] Comparing the two spectra, we can see that exciton emission peak exhibits a preferred polarization that is parallel to the polarization of the excitation. Valley coherence is defined as $(I_{\parallel}-I_{\perp})/(I_{\parallel}+I_{\perp})$ where $I_{\parallel}$ and $I_{\perp}$ is the emission intensity of co and cross polarized emission, respectively. The spectra revealed up to 60% degree of valley coherence over the A-exciton linewidth (620-650 nm), while the indirect transition exhibits no valley coherence. We note that the sharp peaks at 607 nm and 609 nm correspond to the Raman peaks of the 3L WS_2 exhibiting the same polarization as the pump laser.[28] The suspended atomically thin WS_2 PhC slab supports both material's excitonic resonance and optical guided-mode resonance, providing a platform for probing the strong interaction between exciton and guided photon.

We first performed angle-resolved transmission measurements using a collimated white light source to observe the dispersion of exciton-polariton guided mode. Figure 2.2a shows transmission spectra measured at varying angles of incidence from 0°-17°. The dispersion shows the guided-mode resonance blue-shifting towards the exciton resonance at 1.99 eV (~624 nm), as the incident angle increases. When the two resonances approach each other, the dispersion exhibits an anti-crossing (black solid lines) which is a result of strong coupling between the in-plane exciton and guided mode resonance. We further analyzed the mode in dispersion color maps of RCWA simulated and experimental transmission shown in Figure 2.2b and Figure 2.2c, respectively. Data in both plots are normalized along all angles at fixed energies. At 8° incidence, the photonic resonance overlaps the A-exciton resonance. Here, an anomalous dispersion emerges as a result of strong coupling between the exciton and guided resonances in the WS_2 slab. In the real frequency space, this interaction manifests itself as a back-bending in the mode dispersion, suggesting that

the interaction is in the strong coupling regime.[29] White crosses indicate the simulated dispersion of the same photonic mode in a non-excitonic material (section 2.4.4). It is clear that coupling between excitons and photons leads to a modulated dispersion when the energies of the two modes are degenerate. The positions of exciton-polariton resonance were determined from Figure 2.2c by fitting a Lorentzian curve over the angular spectrum at a fixed energy (black solid line). Using Equation 1 and the extracted resonance positions, we calculated the real part of n_{eff} as shown in Figure 2.2d.

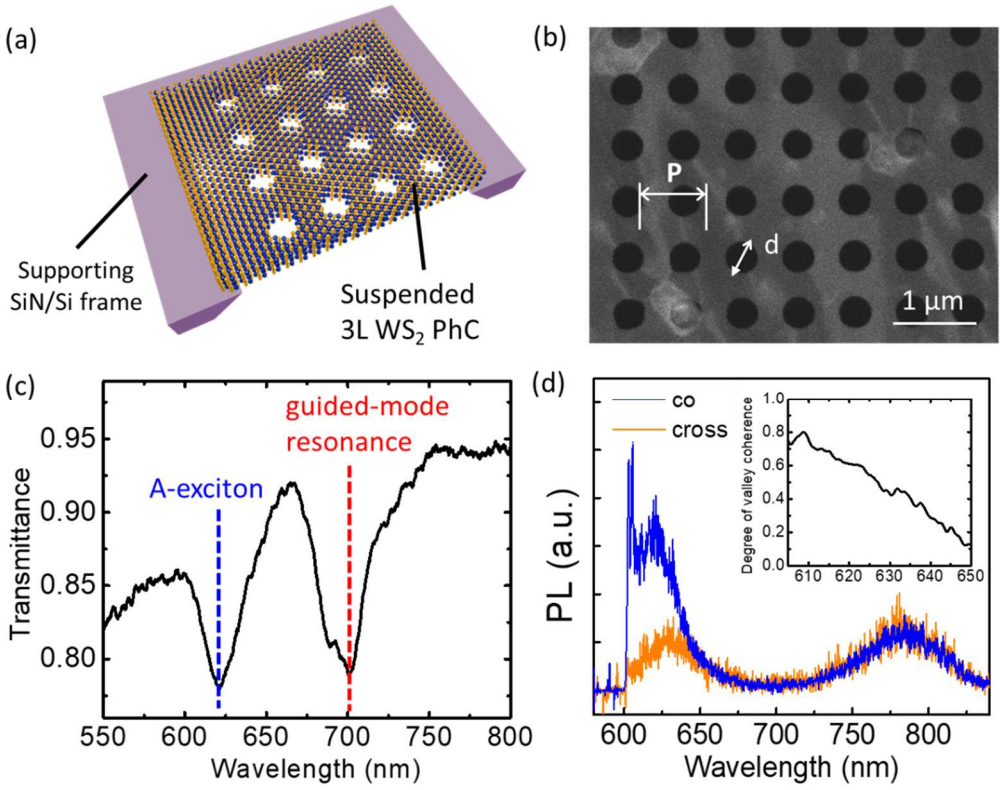

Figure 2.1: Sample schematic and characterization.
(a) Schematic of free-standing three-layer WS_2 photonic crystal supported by a SiN/Si frame. (b) SEM of the suspended WS_2 photonic crystal. P and d are the period and hole diameter. (c) Transmission spectrum of 3L WS2 photonic crystal with P = 700 nm and d = 340 nm. The spectrum shows two resonances at 624 nm and 705 nm, corresponding to the A-exciton absorption and guided-mode resonance of the photonic crystal, respectively. (d) Polarization-resolved PL emission spectrum ex(d by linearly polarized laser beam at 594 nm at room temperature. Blue and orange spectra indicate polarized emission parallel and perpendicular to the polarization of excitation, respectively.

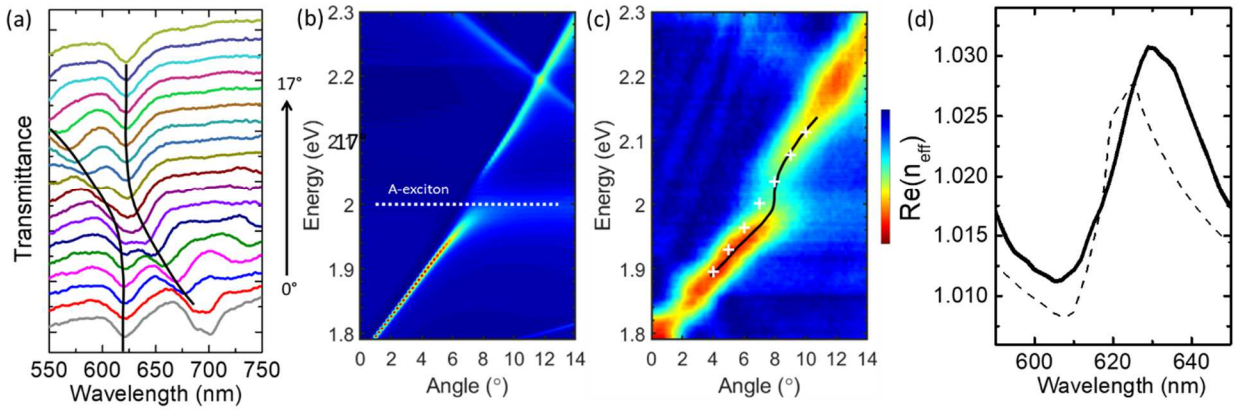

Figure 2.2: Dispersion of 3L WS_2 photonic crystal guided-mode resonance.
(a) Measured transmission spectra at different angle of incidence of 3L WS_2 photonic crystal. (b) Color map of RCWA simulated angle-resolved transmission of 2 nm thick WS_2 photonic crystal with P = 700 nm and d = 340 nm. The data was normalized by maximum at each wavelength. White dotted line represents the A-exciton energy. (c) Color map of measured angle-resolved transmission. Data was taken at 0.2° incidence interval and normalized by maximum at each wavelength. Overlaid crosses show the dispersion of the same guided-mode resonance of the same photonic crystal made from a material without an excitonic oscillator. Black solid line traces the angular position of the resonances. (d) Real part of the effective mode index, n_{eff}, extracted from dispersion in (b) and (c). Solid and dotted lines show simulated and measured data, respectively.

Next, we directly probed the propagation lengths of exciton-polariton in the 3L WS_2 waveguide using the photoluminescence of WS_2 as a near-field light source. To increase the intensity of the exciton emission, we adopted a laser-thinning technique to generate a local emitter with monolayer-like emission.[30] The thinning procedure and PL comparison are detailed in section 2.4.5. We note that this treatment only changed the PL locally on an unpatterned region of the suspended WS_2 PhC, while material properties on the PhC patterned region remained the same. Using this monolayer-like PL as a near-field emitter, we analyzed the evolution of the PL spectra several microns away from the excitation spot. The collection system was composed of a 0.9 NA objective, real-space aperture, back focal plane (BFP) lens, and BFP aperture (Figure 2.8). As illustrated in Figure 2.3a, an unpatterned area of suspended WS_2 was excited by a focused 532 nm

laser with a spot size of approximately 500 nm. At a distance r_1 away from the laser spot, we opened a narrow real-space aperture across the PhC with a slit width of $\Delta r = r_2 - r_1 \approx 2$ μm. In the back focal plane, we fixed the aperture to around the middle portion of the arc as we increased the distance between the real-space aperture and the excitation spot. Because of the fixed aperture in the back focal plane, only the PL propagated at a certain angle was collected (red area within the slit in Figure 2.3a). The in-plane propagation of exciton-polariton is approximated as a cylinder wave whose intensity follows $\exp(-r/L_p)/r$, where L_p is the propagation length and r is the distance to the source. The total power of scattered photons is proportional to the surface integral of the exciton-polariton intensity, which can be approximated as an exponential function of the distance from the excitation spot when Δr is small (section 2.4.8):

$$I_{BFP} \propto \int_{r_1}^{r_2} \frac{e^{-r/L_p}}{r} 2\theta r dr \approx 2\theta \Delta r \, e^{-\bar{r}/L_p} \tag{2}$$

where r_1, r_2 and θ are as defined in Figure 2.3a and $\bar{r} = (r_1+r_2)/2$.

Figure 2.3b shows the measured PL spectra collected from varying distances away from the pump spot. The PL intensity decreases exponentially as the distance increases, with each wavelength exhibiting varying decay constants which directly relate to the propagation lengths of the exciton-polaritons (Figure 2.3c).[31] Using Equation 2 and by fitting an exponential decay, we extracted the L_p at each photon energy within the bandwidth of the PL emitter (section 2.4.8). As seen in Figure 2.3d, L_p decreases to a minimum (~2 μm) near the A-exciton energy and increases rapidly as detuning increases. This trend is consistent with other theoretical and experimental works for atomically thin TMDC waveguides.[11,32] The propagation length L_p of exciton-polariton is directly related to the imaginary part of the propagation constant β:[8,11]

$$L_p = \frac{1}{2Im(\beta)} \tag{3}$$

Using the experimental L_p and Equation 3, we obtained the imaginary part of the effective mode index shown in Figure 2.3e. The plot shows a peak at the A-exciton resonance as absorption loss dominates. The extracted complex effective mode index of the guided-mode resonance (Figure 2.2d and Figure 2.3e) suggests a strong interaction between the slab guided mode and the material's excitonic resonance.

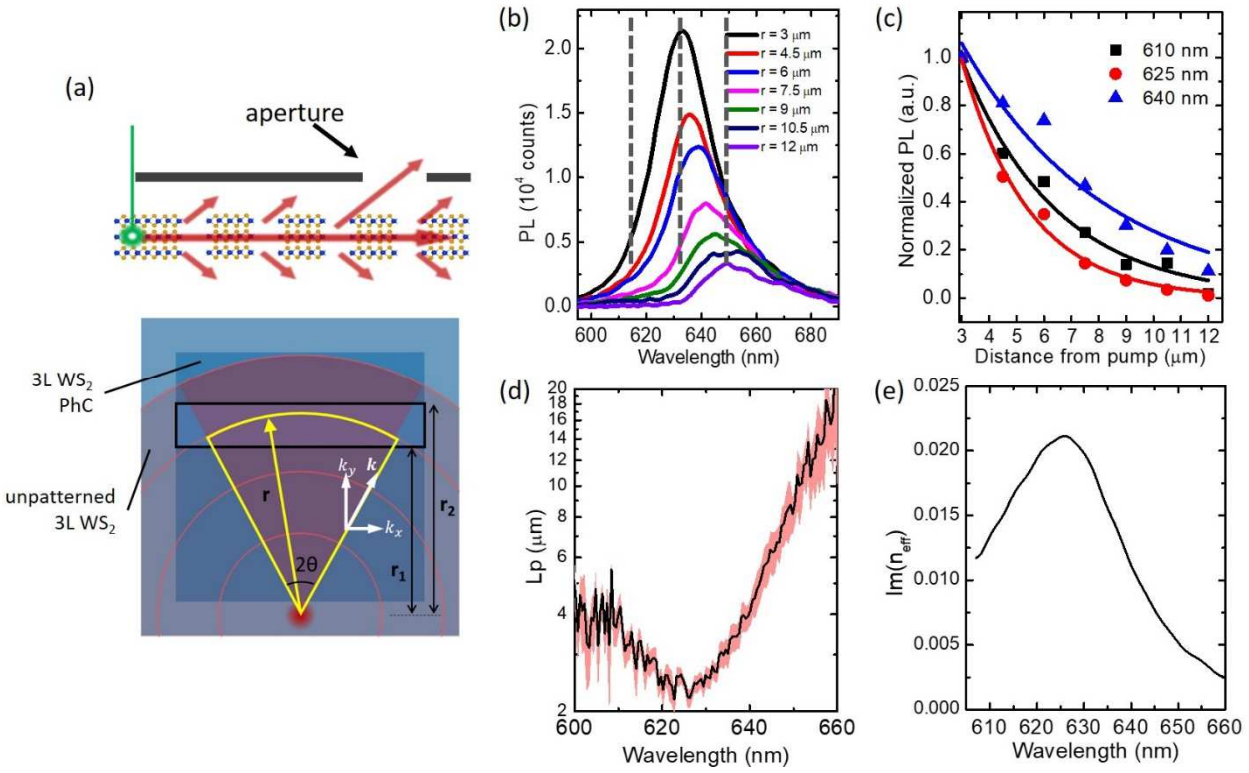

Figure 2.3: Propagation of exciton-polartion.
(a) Schematic of exciton-polariton propagation experiment. (b) PL spectra measured from a slit a fixed distance away from the excitation spot. (c) PL intensities at 610 nm, 625 nm and 640 nm as a function of distance from the excitation spot. The decay was fitted with an exponential function shown in Equation 2. (d) Experimental propagation length (L_p) of exciton-polariton extracted from PL spectra shown in (b). Red region shows fitting error. (e) Imaginary part of the effective mode index extracted from (d).

Having established the exciton-polariton dispersion, we continued to examine the polarization of the guided-mode resonance. The atomically WS_2 waveguide is TE in nature, with its electric field polarized in the plane of the material and perpendicular to the direction of propagation. As seen in Equation 1, the guided-mode resonance diffracted by the 3L WS_2 PhC forms an arc in the momentum space centered at $(-m\frac{2\pi}{\Lambda k_0}, -n\frac{2\pi}{\Lambda k_0})$ with a radius of n_{eff} and Λ=700 nm. Each point on the arc corresponds to the in-plane components, k_x and k_y, of the free-space wavevector k_0, that correlates to the in-plane direction of propagation.

To resolve the polarization of the quasi-guided mode, we used a polarizer analyzer to extract the x- and y-polarized components of the resonance measured from a slit 4 μm away from the excitation spot (Figure 2.4a and Figure 2.4d). For propagation in the x-direction (Figure 2.4a), the diffracted light forms a bright arc in the back focal plane centered at $(0, -\frac{2\pi}{\Lambda k_0})$. The back focal plane arc was obtained through an x- and y-polarized analyzers in Figure 2.4b and Figure 2.4c, respectively. Clearly, the y-component of the mode is much stronger, verifying that TE waveguide mode propagating in the x-direction is dominantly y-polarized. The inverse is true for exciton-polariton traveling in the y-direction, shown in Figure 2.4e and Figure 2.4f. As a control, we rotated the sample and slit 90° so that we can observe the guide-mode resonance emission from the same region of 3L WS_2 PhC in the y-direction. Using the same excitation power and spot, the bright arc is now centered at $(-\frac{2\pi}{\Lambda k_0}, 0)$ and the mode is x-polarized, perpendicular to the direction of propagation. The intensities of the arcs in Figure 2.4c and Figure 2.4e are also comparable, indicating a uniform propagation of unpolarized PL in all directions. Slight differences in intensities are attributed to the inherent polarization-dependent attenuation in the collection path. This polarization-dependent propagation provides a platform for spatial separation of valley-coherent exciton-polaritons.

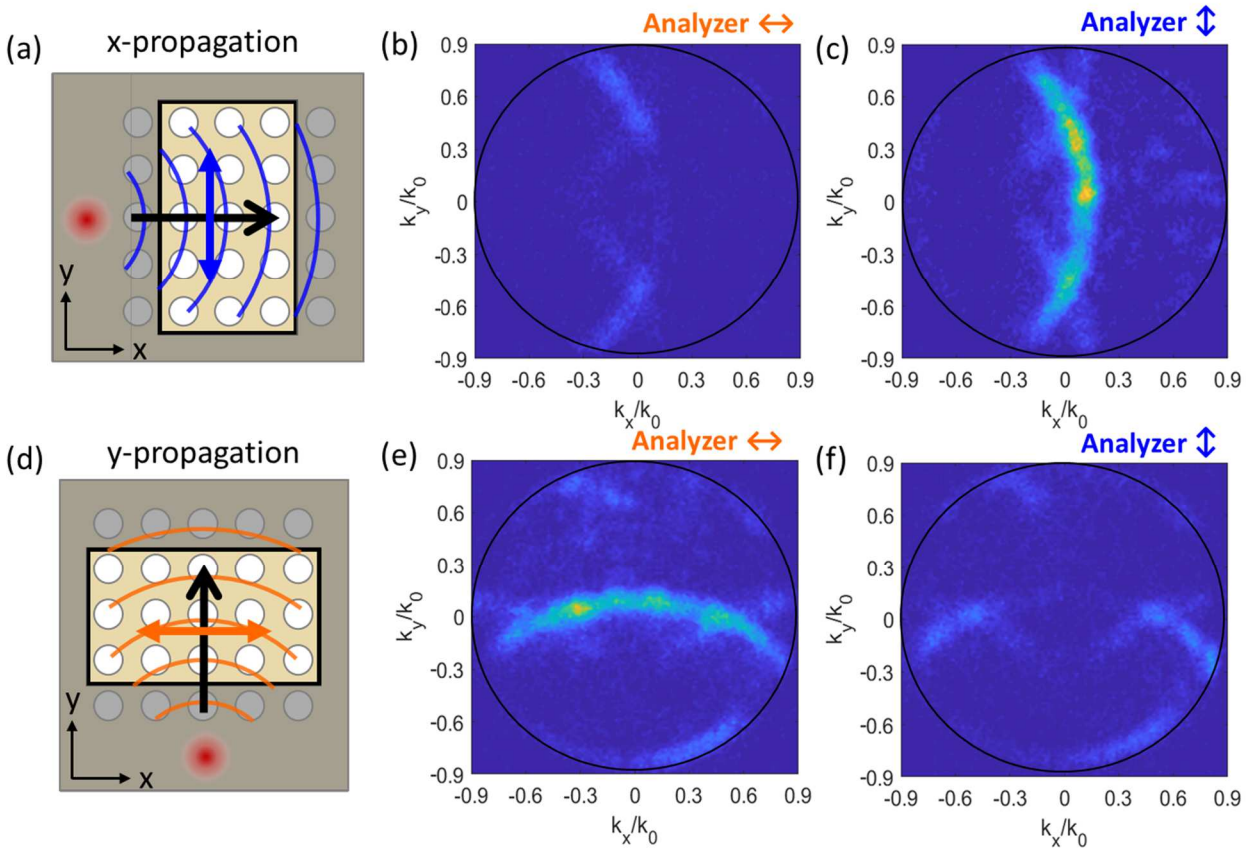

Figure 2.4: Polarization-dependent propagation of the guided-mode resonance. (a) Schematic of the measurement where propagation in the x-direction is observed. (b),(c) Measured back focal plane emission with an x- and y-polarized analyzer, respectively. (d) Schematic of the measurement where propagation in the y-direction is observed. (e),(f) Measured back focal plane emission with an x- and y-polarized analyzer, respectively.

Moving the excitation source to the center of the 3L WS_2 PhC, we probed the directional transport of exciton-polariton by placing two spatial apertures centered 4 μm above (aperture 1) and to the right (aperture 2) of the excitation spot, as shown in Figure 2.5a and Figure 2.5d. When the pump laser is x-polarized (Figure 2.5a), we observed guided-mode resonance emission in the back focal plane from apertures 1 and 2 (Figure 2.5b and Figure 2.5c, respectively). It is evident that the emission is stronger in aperture 1, indicating that the mode extends primarily in the y-direction when the pump laser is x-polarized. In Figure 2.5d, the polarization of the pump laser

was rotated 90° and the excitation power was kept constant. Comparing Figure 2.5e and Figure 2.5f, we see that the mode instead expands in the x-direction as the intensity of the arc is now stronger from aperture 2. We note that as x- and y-polarized components undergo different degrees of attenuation in the collection path of our optical set up, we normalized the back focal plane measurements by the maximum counts of each aperture. This allows us to directly compare the guided-mode resonance obtained from the two apertures.

To evaluate the spatial valley coherence of the guided-mode resonance, we employed the same calculation to the back focal plane arc intensities for propagation in the x- (aperture 2) and y-direction (aperture 1). Figure 2.5g and Figure 2.5h show the degree of valley coherence of 30-60% on the back focal plane arcs for both propagation directions. This is consistent with the valley coherence of the PL at the excitation source, which suggests the valley coherence of the PL is transferred to the spatial separation of exciton-polariton guided-mode resonance. Our results show efficient coupling of valley-coherent exciton-polariton to the TE waveguide mode in atomically thin WS_2, with direction of propagation locked to the linear polarization of the exciton-polariton.

2.3 Conclusion

We have demonstrated in this work directional propagation of self-resonant exciton-polariton via guided-mode resonance in a suspended 3L WS_2 PhC. On this platform, the slab WS_2 waveguide is weakly modulated by the presence of a nanohole array, which acts as 2D gratings that scatter out the previously dark exciton-polariton modes into the radiation continuum as guided-mode resonances. This allows us to obtain the mode dispersion and propagation lengths of the exciton-polaritons. Furthermore, the TE-polarized nature of the structure allows it to spatially separate the valley coherent exciton-polaritons into perpendicular directions. Our unique approach

enables the inherent control of exciton-polariton propagation without utilizing an external interface, allowing for high directional coupling efficiency. This work provides a platform for manipulation of valley excitons in coherent light-matter states for exploring hybrid valley-dependent photonic devices.

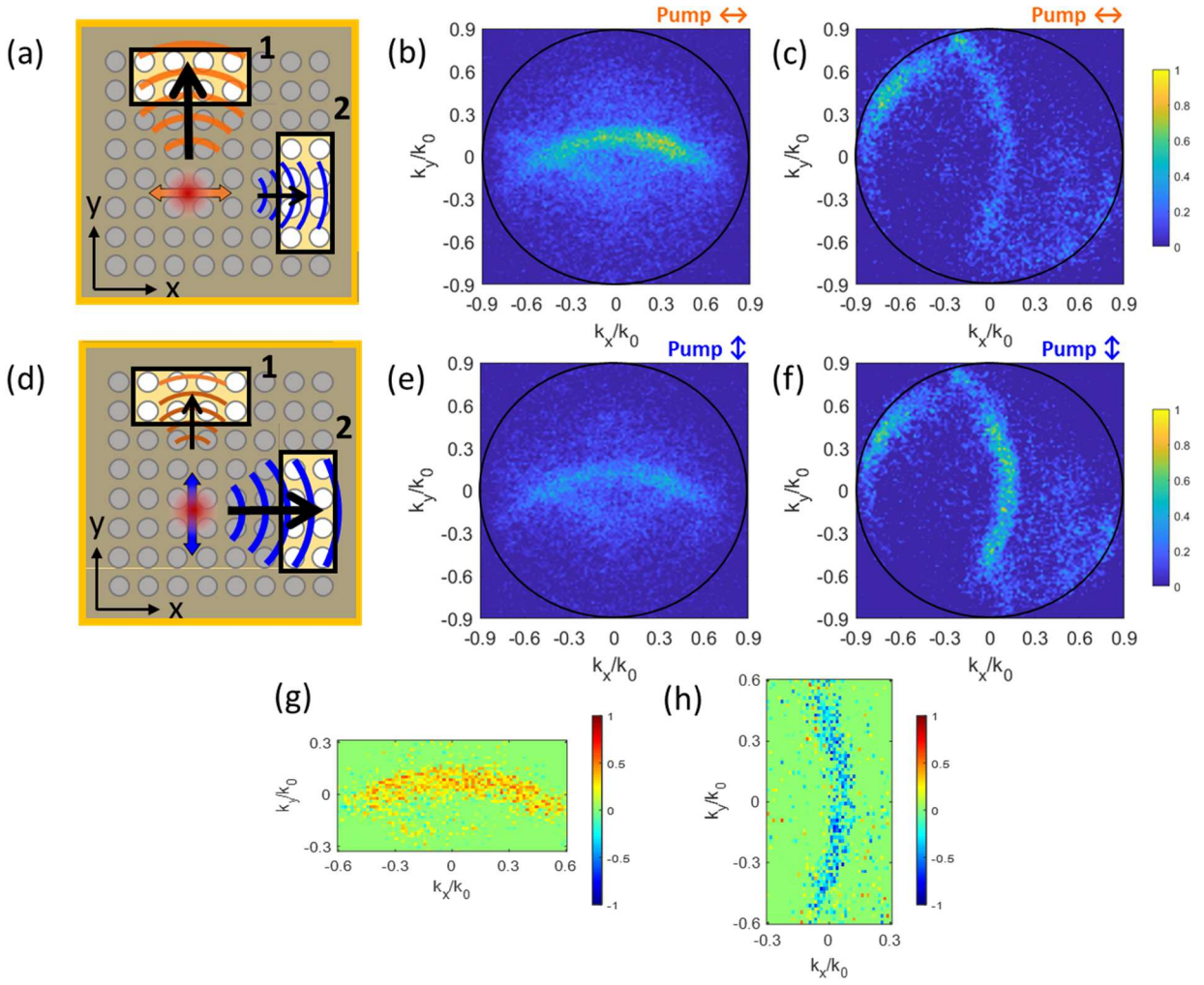

Figure 2.5: Control of propagation direction based on polarization of excitation. (a,d) Schematic of directional propagation of exciton-polariton when the 594 nm excitation source is x-polarized (a) and y-polarized (d). (b,e) Measured back focal plane emission from aperture 1 in (a,d) with x- and y-polarized excitation, respectively. Data was normalized by the maximum count in (b). (c,f) Measured back focal plane emission from aperture 2 in (a,d) with x- and y-polarized excitation, respectively. Data was normalized by the maximum count in (f). (g,h) Valley coherence of the exciton-polariton guided-mode resonance in the focal plane emission obtained from apertures 1 (g) and 2 (h).

2.4 Methods

2.4.1 Transverse electric guided modes in a thin symmetric slab waveguide

Suspended WS_2 in the yz-plane can be treated as an infinitely large slab waveguide with a refractive index profile

$$n(x) = \begin{cases} 1 & x > 0 \\ n_2 & -h < x < 0 \\ 1 & x < -h \end{cases} \quad \text{(S-1)}$$

In all three regions, the general solutions to the wave equation for the transverse electric (TE) modes propagating in the +z direction can be written as

$$\boldsymbol{E_y} = \hat{y} E_{y0}(x) e^{-j(\beta z - \omega t)} \quad \text{(S-2)}$$

where β is the in-plane propagation constant, and E_y has the general form with constant coefficients A, B, C and D, and out-of-plane propagation constants u and v:

$$E_{y0}(x) = \begin{cases} Ae^{-vx} & x > 0 \\ B\cos(ux) + C\sin(ux) & -h < x < 0 \\ De^{dv(x+h)} & x < -h \end{cases} \quad \text{(S-3)}$$

where u and v can be described as

$$u = (n_2^2 k_2^2 - \beta^2)^{\frac{1}{2}} \quad \text{(S-4)}$$

$$v = (\beta^2 - k_0^2)^{\frac{1}{2}} \quad \text{(S-5)}$$

where k_0 is the free space wavevector.

Analyzing the boundary conditions at slab interfaces, we specify the constant coefficients in terms of A: B= A, $C = (-v/u)A$ and $D = A[\cos(uh) + (v/u)\sin(uh)]$. Substituting these into equations S-2 and S-3, we obtain the expressions for E_y in each medium.

$$\boldsymbol{E_y} = \hat{y}e^{-j(\beta z-\omega t)}\begin{cases} Ae^{-vx} & x > 0 \\ A\left[\cos(ux) - \left(\frac{v}{u}\right)\sin(ux)\right] & -h < x < 0 \\ Ae^{v(x+h)}\left[\cos(uh) + \left(\frac{v}{u}\right)\sin(uh)\right] & x < -h \end{cases} \quad \text{(S-6)}$$

Considering continuous $H_z = (\frac{j}{\omega\mu_0})\frac{\partial E_y}{\partial x}$ at slab boundary $x = -h$, we obtain

$$\tan(uh) = \frac{2v}{u^2 - v^2} \quad \text{(S-7)}$$

Solving this equation yields discrete values of allowed β that can exist within the waveguide. The guiding cut-off condition for this symmetric waveguide corresponds to $\beta \to k_0$, below which the mode is no longer confined within the slab. Substituting this condition into equation S-7, we find that $h_{cutoff} = 0$. In other words, the cut-off thickness for the TE symmetric slab waveguide mode is zero. Similarly, we can show that the cut-off thickness for the TM mode is also zero. However, due to the much weaker excitonic response in the out-of-plane direction in 3L WS_2, we evaluated the exciton-polariton interaction for the TE case only.

2.4.2 Guided-mode resonances and effective mode index in a photonic crystal slab

A hole array patterned into a 3L WS_2 crystal suspended in air introduces scattering loss to the in-plane guided modes. This manifests as Fano or guided-mode resonance in the far-field and allows us to probe the dispersion and propagation nature of the exciton-polariton. The presence of the air holes creates a periodic modulation of the refractive index in the slab. This leads to folding of the waveguide mode dispersion above the light line, allowing for coupling to radiation modes.[33] Now, we analyze the guided-mode resonances in a PhC slab based on Rigorous Coupled-Wave analysis (RCWA) as developed in references [24,25].

Consider light guiding in the z-direction along an infinitely large slab waveguide in the xy-plane. The dielectric constant of the slab, ϵ_2, is spatially and periodically modulated as $\epsilon_2(z+\Lambda) = \epsilon_L + (\epsilon_H - \epsilon_L)f(z)$, where $f(z) = 0\ or\ 1$. The average value of the relative permittivity of the slab is $\epsilon_g = (1-g)\epsilon_H + \epsilon_L$ where g is the filling fraction.[34]

For TE polarization, we can express the total electric field inside the slab as a Fourier expansion of harmonic fields propagating along the x-axis,

$$E_{y,2}(x,z) = \sum_{m=-\infty}^{+\infty} \hat{S}_m(z) e^{-jk_{x2}x} \tag{S-8}$$

where $k_{z,2}$ is the determined by the Floquet condition, $k_{x,2} = k_0(\sqrt{\epsilon_g}\sin\theta_2 + \frac{m\lambda}{\Lambda})$, and $\hat{S}_m(z)$ is the amplitude of the plane wave of the m[th] space harmonic, $\hat{S}_m(z) = \sum_{p=-\infty}^{+\infty} C_{p,m} e^{-j\xi_p z}$ where p is the transverse mode order. The coupled-wave equations governing the wave propagation in the PhC slab can be written as[35]

$$\frac{d^2\hat{S}_m(z)}{dz^2} + (k_0^2\epsilon_g - k_{z,2}^2)\hat{S}_m(z) + jk_0^2(\epsilon_H - \epsilon_L)\sum_{h=1,3,5}^{+\infty}\frac{1}{\pi h}\left[\hat{S}_{m+h}(z) - \hat{S}_{m-h}(z)\right] = 0 \tag{S-9}$$

For weakly modulated gratings, i.e. $\epsilon_H - \epsilon_L \to 0$, equation S-9 loses the last term and, therefore, the total field inside the slab has the form of the wave equation of an unmodulated dielectric waveguide:

$$\frac{d^2E_{y,2}(z)}{dz^2} + \left(k_0^2\epsilon_g - \beta^2\right)E_{y,2}(z) = 0 \tag{S-10}$$

where $\beta$is the propagation constant, $\beta = k_{x,2} = k_0(\sqrt{\epsilon_g}\sin\theta_2 + \frac{m\lambda}{\Lambda})$. Using the propagation constant and the Snell's law, we determine the momentum matching condition for coupling incident light at an angle θ_1 into a guided-mode resonance of the PhC:

$$\beta = k_0(\sqrt{\epsilon_1}\sin\theta_1 + \frac{m\lambda}{\Lambda}) \tag{S-11}$$

From equation S-11, we obtain the real part of the mode index

$$n_{eff} = \sqrt{\epsilon_1}\sin\theta_1 + m\frac{\lambda}{\Lambda}, m = 0, \pm1, \pm2, \ldots \tag{S-12}$$

For light guiding in the xy-plane of a PhC slab, we break down the momentum matching condition into two orthogonal directions: $|\beta|^2 = \left|\beta_x\vec{x} + \beta_y\vec{y}\right|^2$, where $\beta_x = k_x + m\frac{2\pi}{\Lambda}, m =$ 0,1,2 ..., and $\beta_y = k_y + n\frac{2\pi}{\Lambda}, n =$ 0,1,2 .... Therefore, we can relate the real part of the mode index to the period of modulation and wave vectors in the x- and y-directions.

$$n_{eff}^2 = \left(\frac{k_x}{k_0} + m\frac{2\pi}{\Lambda \mathrm{k}_0}\right)^2 + \left(\frac{k_y}{k_0} + n\frac{2\pi}{\Lambda \mathrm{k}_0}\right)^2 \tag{S-13}$$

From equation S-13, we can see that in the momentum space (or back focal plane) the equi-frequency contours of the guided-mode resonance are arcs centered at $(-m\frac{2\pi}{\Lambda k_0}, -n\frac{2\pi}{\Lambda k_0})$ with a radius of n_{eff}.

We note that the mode index for the guided-mode resonance is complex, i.e. $\tilde{n}_{eff} = n_{eff} - j\kappa_{eff}$, with the diffraction and absorption losses represented by the imaginary term κ_{eff}. This can be extracted from the transmission spectra in two methods to find $\kappa_{eff}(\lambda)$ and $\kappa_{eff}(\theta_1)$.[36] The first way is by fixing the angle of incidence and extracting the spectral linewidth $\delta\lambda$:

$$\kappa_{eff}(\lambda) = \frac{\delta\lambda}{2\Lambda} \tag{S-14}$$

The second method is by fixing the incident wavelength and sweeping the incident angle to obtain the angular linewidth $\delta(\sin\theta_1)$ of the resonance:

$$\kappa_{eff}(\theta_1) = \frac{\delta(\sin\theta_1)}{2} \tag{S-15}$$

2.4.3 Fabrication of suspended WS_2 photonic crystal

To fabricate the suspended 3L WS_2 PhC, a hole array with desired parameters was first milled through a 20x20 μm, 20-nm-thick suspended SiN window (Norcada) by focused ion beam (FIB).[37] Next, we transferred a mechanically exfoliated 3L WS_2 flake directly on top of the patterned SiN window using a PDMS stamp-based dry transfer technique, covering the entire suspended region. The sample was then flipped upside down and undergone reactive ion etching (RIE) for a few seconds. This process etches the regions of WS_2 suspended over holes with the patterned SiN acting as a mask. Finally, the supporting SiN was slowly etched away with HF vapor, releasing and suspending the patterned WS_2 over the 20x20 μm window. A more detailed illustration of the fabrication process is described in our previous work.[10]

2.4.4 Dispersion of 3L WS_2 photonic crystal without A-exciton resonance

Figure 2.2c in main text shows a color map of angle-resolved transmittance of a suspended 3L WS_2 PhC slab. The overlaid crosses show the simulated dispersion of the same guided-mode resonance in the same material, but with the A-exciton resonance omitted. This was done by fitting the permittivity and removing the oscillator at the A-exciton position. The complex permittivity

($\epsilon = \epsilon_0(\epsilon' - j\epsilon'')$) of this material is shown in Figure 2.6a, and the corresponding dispersion is obtained from the simulated transmittance color map in Figure 2.6b. Clearly when the A-exciton resonance is absent, we do not observe the back-bending characteristics of the exciton-polariton interaction.

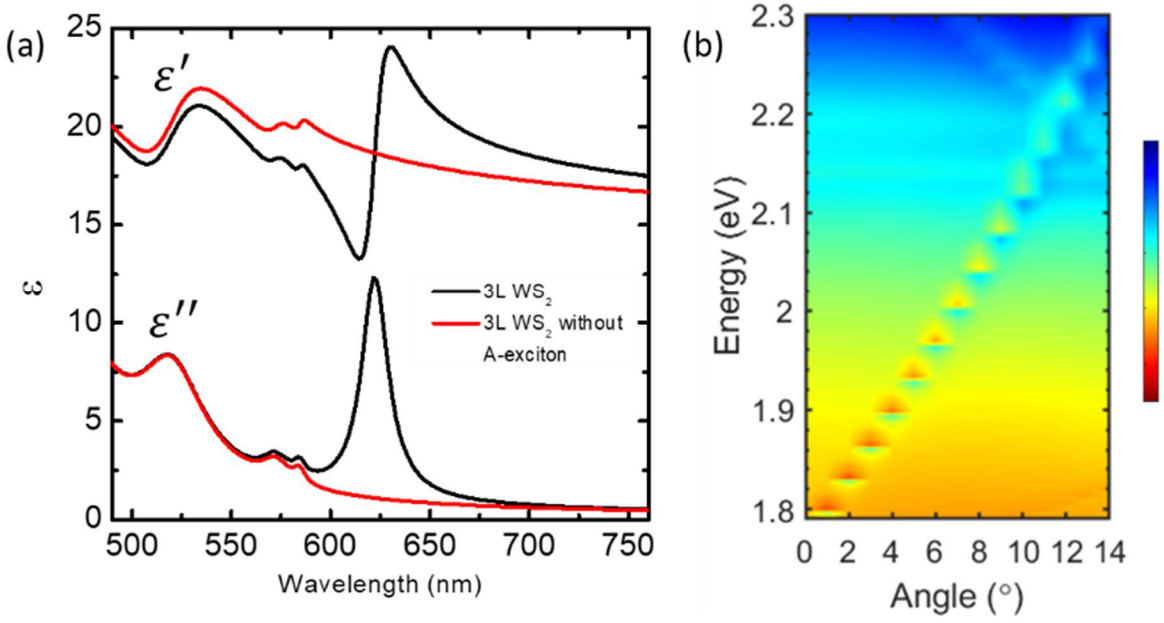

Figure 2.6: Simulated dispersion relation of 3L WS_2 PhC wihtout exciton resonance (a) Complex permittivity of a 3L WS_2 (black) and 3L WS_2 with the A-exciton oscillator omitted. (b) Angle-resolved transmittance of a suspended PhC slab of the hypothetical material with the same thickness and PhC parameters as the sample in the main text. Discontinuity is caused by simulation interval of 0.5°.

2.4.5 Optical thinning procedure of 3L WS_2

To enhance the direct bandgap excitonic emission, we exposed a suspended, unpatterned region of 3L WS_2 to a focused laser beam with high power density of ~40 mW/μm^2 for at least 2 hours. In Figure S1, we see that the direct excitonic PL substantially improved after the laser treatment, while the indirect PL was suppressed. We attributed this effect to laser-induced thinning of the 3L WS_2 to 1L WS_2. This phenomenon was previously observed and studied in MoS_2 and

WS_2 films.[30,38,39] In this work, we used this technique to controllably introduce a local 1L-like emitter with relatively high intensity near the patterned PhC. This ultimately enables us to probe the propagation lengths of exciton-polariton as detailed in the main text and Figure 3.

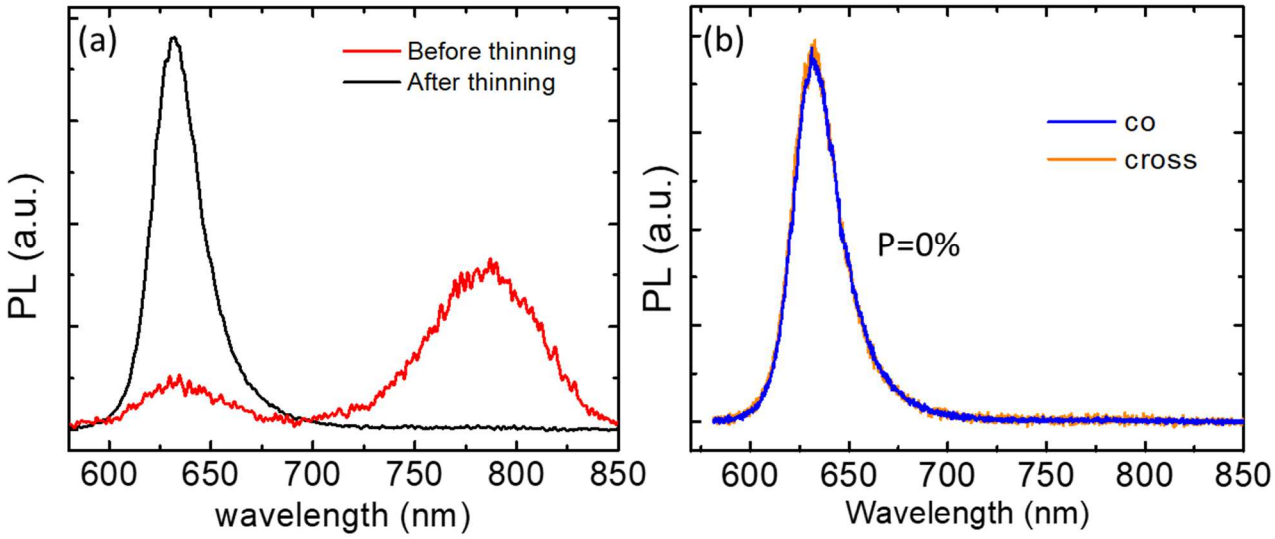

Figure 2.7: Monolayer-like photoluminescence
(a) PL spectra of 3L WS_2 before and after high power laser exposure for over 2 hours. (b) Linear polarization-resolved PL spectra of monolayer-like thinned WS_2, showing zero valley coherence

2.4.6 Polarization-resolved back focal plane imaging of guided mode resonance

To image guided-mode resonance dispersion, we set the image plane aperture a distance away from the excitation spot and captured the full back focal plane on a CCD camera (Figure 2.8a). We performed polarization-resolved measurements using a polarizer for the excitation and analyzer for the emission. Co and cross polarized emission can be obtained by fixing the polarizer and rotating the analyzer or vice versa (Figure 2.8b). WS_2 sample was excited using a 594 nm continuous wave laser focused into a spot using a 0.9 NA objective.

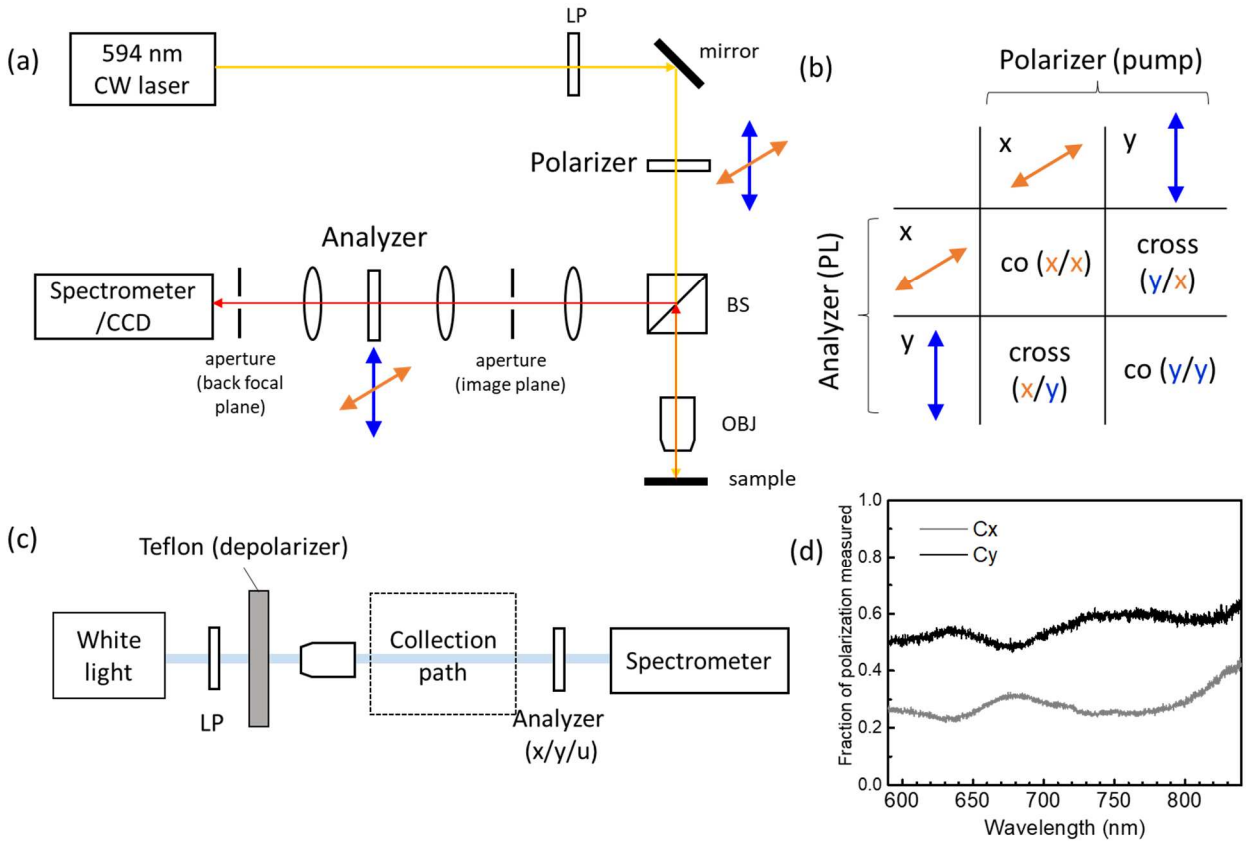

Figure 2.8: Polarization-resolved photoluminescence measurements.
(a) Polarization-resolved PL measurement setup, (b) Definition of co and cross polarization, (c) Schematic for obtaining polarized calibration coefficient. Broadband spectra can be obtained with (x and y) or without (u) an analyzer. (d) Calibration coefficients for the collection path for x- and y- polarization as a function of wavelength.

2.4.7 Polarization-resolved photoluminescence spectroscopy

Polarization-resolved PL spectra were obtained using a spectrometer in a similar setup. However, our collection path exhibits an inherent polarization bias that is also a function of wavelength. To account for polarization-dependent attenuation, we calibrated the emission intensity for x- and y-polarized light using the setup shown in Figure 2.8c. We used a slab of Teflon to depolarize the incident white light, giving us an unpolarized broadband source. We measured the transmitted spectrum of this light through the collection path 1) without an analyzer (u), 2) with an analyzer oriented along the x-axis (x), and 3) with an analyzer oriented along the y-axis

(y). Figure 2.8d shows the calibration coefficients, C_x and C_y, obtained by dividing each polarized spectrum (x and y) by the spectrum of unpolarized light (u). Therefore, polarized emission can be corrected by dividing the measured intensity by the coefficient for that polarization.

2.4.8. Back focal plane arc intensity and calculation of propagation length

To probe the propagation length of exciton-polariton, we pumped a laser-thinned area located just outside of the patterned PhC and observed the emission from the PhC through slits at a known distance away from the pump spot. The strong monolayer-like emission of laser-thinned WS_2 acts as a near-field emitter and allows us to obtain good signal several microns away from the pump. Figure 2.9 shows the schematic and the slit apertures used in this experiment. The image plane aperture (slit) extends from one side of the PhC to another and are narrow in width. In the back focal plane, we close another aperture around the center area of the arc. Effectively, this allows us to collect a portion of propagating light within angle 2θ in each slit (red regions in Figure 2.9a). By closing the back focal plane aperture around the center portion of the arc (orange box in Figure 2.9b), we can measure the spectrum of the scattered photons. The total intensity of the scattered photons is proportional to the surface integral of the exciton-polariton intensity.

$$I_{BFP} \propto \int_{r_1}^{r_2} \frac{e^{-r/L_p}}{r} dS = \int_{r_1}^{r_2} \frac{e^{-r/L_p}}{r} 2\theta r dr \tag{S-16}$$

where L_p is the propagation length and a function of wavelength λ, $r_1 = \bar{r} - \frac{\Delta r}{2}$, $r_2 = \bar{r} + \frac{\Delta r}{2}$, $\bar{r} = \frac{r_1 + r_2}{2}$ and $\Delta r = r_2 - r_1$. For small Δr, we can approximate the integral as

$$I_{BFP} \propto \int_{r_1}^{r_2} dr \cdot 2\theta e^{-\bar{r}/L_p} = 2\theta e^{-\bar{r}/L_p} \Delta r \tag{S-17}$$

Using equation S-17, we extracted the propagation length, $L_p(\lambda)$, by fitting the PL intensities with an exponential function as shown in Figure 3b and 3c in main text.

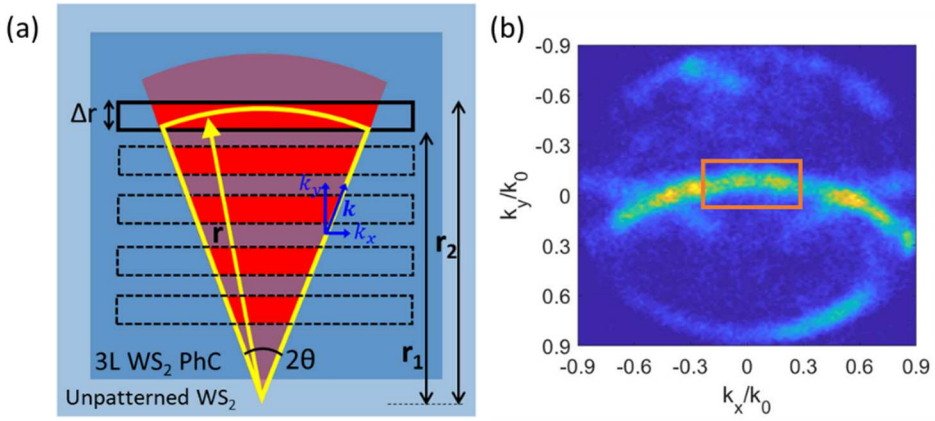

Figure 2.9: Propagation length measurements.
(a) Propagation length measurement schematic. (b) Approximate position of the back focal plane aperture for selecting propagation angles.

2.4.9 Comparison between off-resonance and near-resonance excitation

We compared the emission spectrum and propagation when MoS_2 was excited off-resonance (532 nm) and near-resonance (594 nm). In Figure 2.10, we measured polarized PL spectra excited by both wavelengths, using the setup and calibration outlined in section 2.4.6. In both cases, the indirect bandgap peak exhibits zero valley coherence. By contrast, the exciton peak exhibits a significantly higher degree of valley coherence when MoS_2 is excited closer to the exciton wavelength of ~630nm. Using 594 nm excitation, we can obtain controllable propagation direction as enabled by exciton's valley coherence. Figure 2.11 compares directional propagation of PL in both cases. The back focal plane arcs were imaged without an analyzer. For propagation along the x-axis (Figure 2.11a), there is a clear preference for y-polarized excitation when MoS_2 was excited by a 594 nm laser (Figure 2.11b and Figure 2.11c). For off-resonance excitation with 532 nm, we observe no direction dependence on the pump linear polarization.

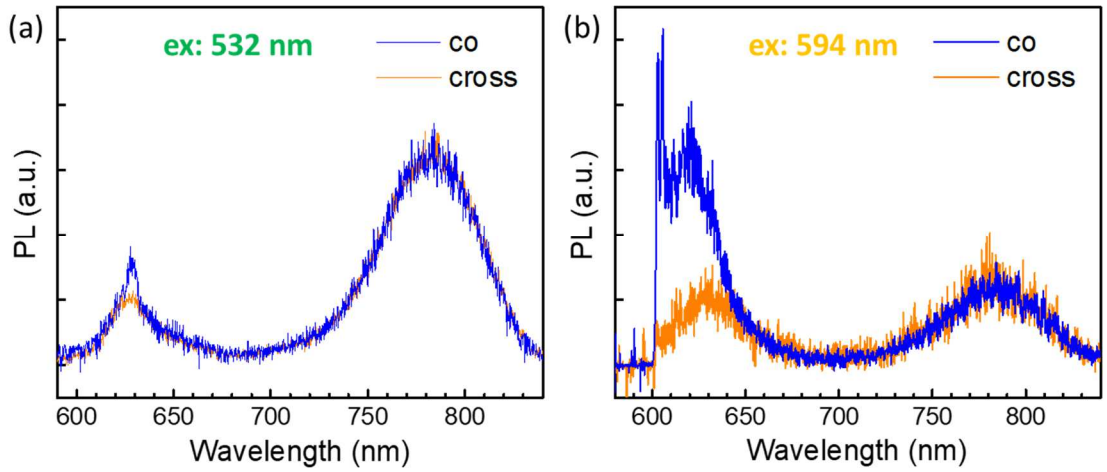

Figure 2.10: Photoluminescence comparison between off- and near-resonance excitation
Polarization resolved PL emission spectra of 3L WS_2 excited by linearly polarized 532 nm laser (a) and 594 nm laser (b).

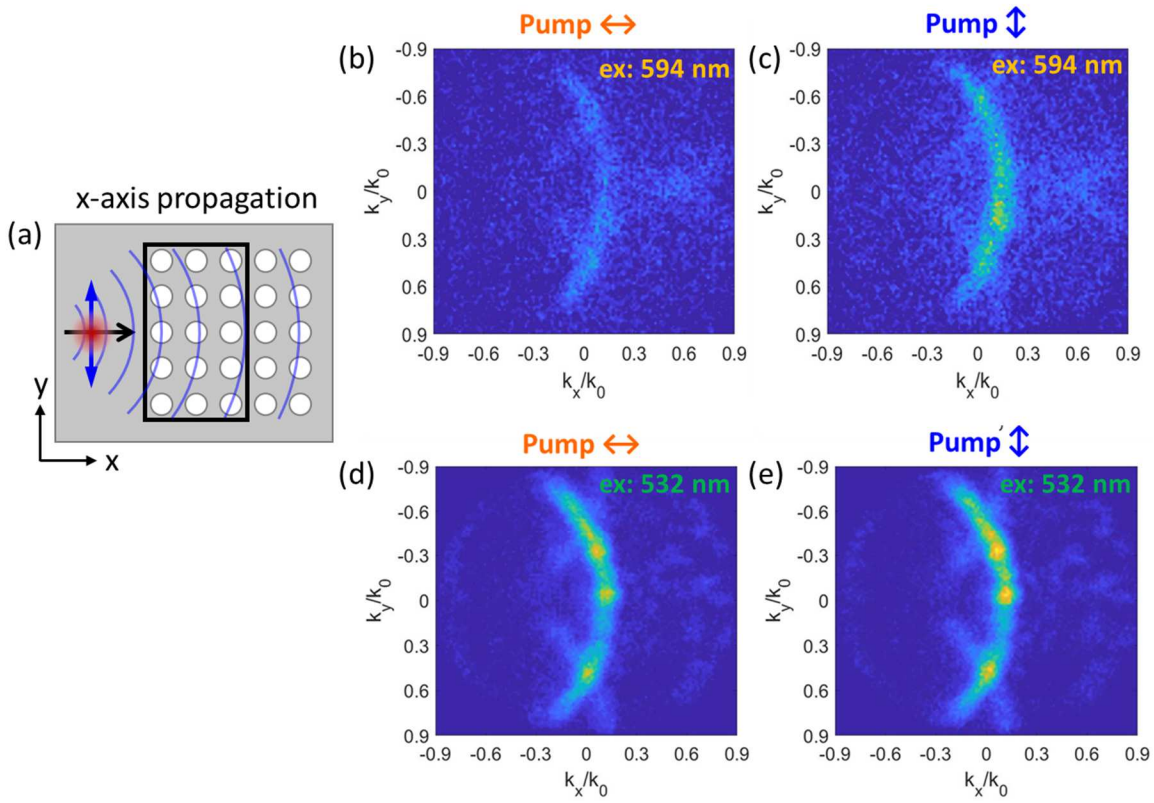

Figure 2.11: Dependence of propagation direction on pump wavelength and polarization.
(a) Sample schematic for imaging back focal plane guided mode resonance emission for x-axis propagation. Emission from the slit was imaged as arcs in the back focal plane when excitation was (b) 594 nm and x-polarized, (c) 594 nm and y-polarized, (d) 532 nm and x-polarized, and (e) 532 nm and y-polarized.

2.5 Acknowledgements

Chapter 2, in part, is currently being prepared for submission for publication of the material as it appears in Directional propagation of self-resonant exciton-polariton in atomically thin tungsten disulfide waveguide. De-Eknamkul, Chawina; Huang, Wenzhuo; Zhang, Xingwang; Cubukcu, Ertugrul. 2022. The dissertation author was the primary investigator and author of this material.

CHAPTER 3 - MoS_2-ENABLED DUAL-MODE OPTOELECTRONIC BIOSENSOR USING A WATER-SOLUBLE VARIANT OF μ-OPIOID RECEPTOR FOR OPIOID PEPTIDE DETECTION

3.1 Introduction

Two-dimensional materials such as graphene and transition metal dichalcogenides (TMDCs) have been widely studied as promising functional materials in various sensing devices.[40–44] Among these, as a naturally available material, MoS_2 stands out as a versatile candidate due to its unique properties, namely the relatively high carrier mobility, suppressed off-state current due to a large electronic bandgap, and structural and chemical stability at ambient temperatures.[45,46] In light of these properties, great efforts have been devoted to developing MoS_2-based nanoelectronic biosensors for detecting a variety of biomolecular interactions, including DNA,[47] prostate specific antigen (PSA),[41,42,48] and glucose.[43] Most of these biosensors operate in a single mode, particularly in a field-effect transistor (FET) configuration, utilizing the changes in channel conductivity and consequently the transduced electrical output as a result of binding or adsorption of target molecules. These binding events occurring near the surface also produce perturbations in the local dielectric permittivity enabling detection via electromagnetic means, which have been elusive. To this end, by coupling MoS_2 with a nanostructure exhibiting photonic resonances,[49–51] one can realize a versatile multimodal sensor capable of interrogating biomolecular interactions with simultaneously transduced electrical and optical signals in one single device platform.

Multimodal biosensors can potentially improve the overall accuracy of detection by comparing results from different mechanisms, obtaining multiple characteristics of a biomolecular binding event and providing flexibility for operation in different situations. Previous works have incorporated the two modes by fabricating plasmonic nanostructures on a TMDC surface,[52] such

that the device exhibits a photonic resonance that spectrally shifts upon attachment of target molecules.[53,54] The integration of graphene or carbon nanotubes into traditional devices have been demonstrated to enable parallel transduction of electronic, optical, and even mechanical signals. However, 2D materials in these devices merely act as a transparent substrate in the optical mode, playing no active role in optical transduction.

Here, we experimentally demonstrate a dual-mode biosensor as shown schematically in Figure 3.1a and Figure 3.1b. By integrating MoS_2 monolayers on a dielectric photonic crystal (PhC) slab with an optically transparent gate electrode, MoS_2 takes an active part in both electrical and optical detection of DAMGO ([D-Ala2, N-MePhe4, Gly-ol]-enkephalin), a synthetic opioid peptide and specific MOR agonist. We choose CVD-grown MoS_2 as the active material because the large (>50 μm lateral size) and dense crystals make it suitable for large scale fabrication of devices.[55,56] In this device, monolayer MoS_2 plays critical roles as a functionalization layer for nanophotonic sensing and FET channel for nanoelectronic sensing.

MoS_2 can be directly functionalized with a synthetic water soluble μ-opioid receptor, wsMOR, via Ni^{2+} linkers.[57,58] Monolayer MoS_2 exhibits a pristine surface with no dangling bonds, making direct functionalization difficult. Yet, proximity of binding events to the active surface is one of the factors that determines the sensitivity of a biosensor. Most MoS_2-based biosensors rely on a silanized top dielectric layer (e.g. APTES functionalization), such as Al_2O_3 and HfO_2 films,[40,42,48] to bind protein probes. This limits the probe-target interactions to occur several nanometers away from the active MoS_2 surface, reducing the expected device sensitivity. The direct functionalization method used here utilizes Ni^{2+} ions adsorbed on the MoS_2 surface to bind to the histidine tag on the wsMOR protein.[59] This allows the receptor-target interactions to take place very close to the surface of monolayer MoS_2.

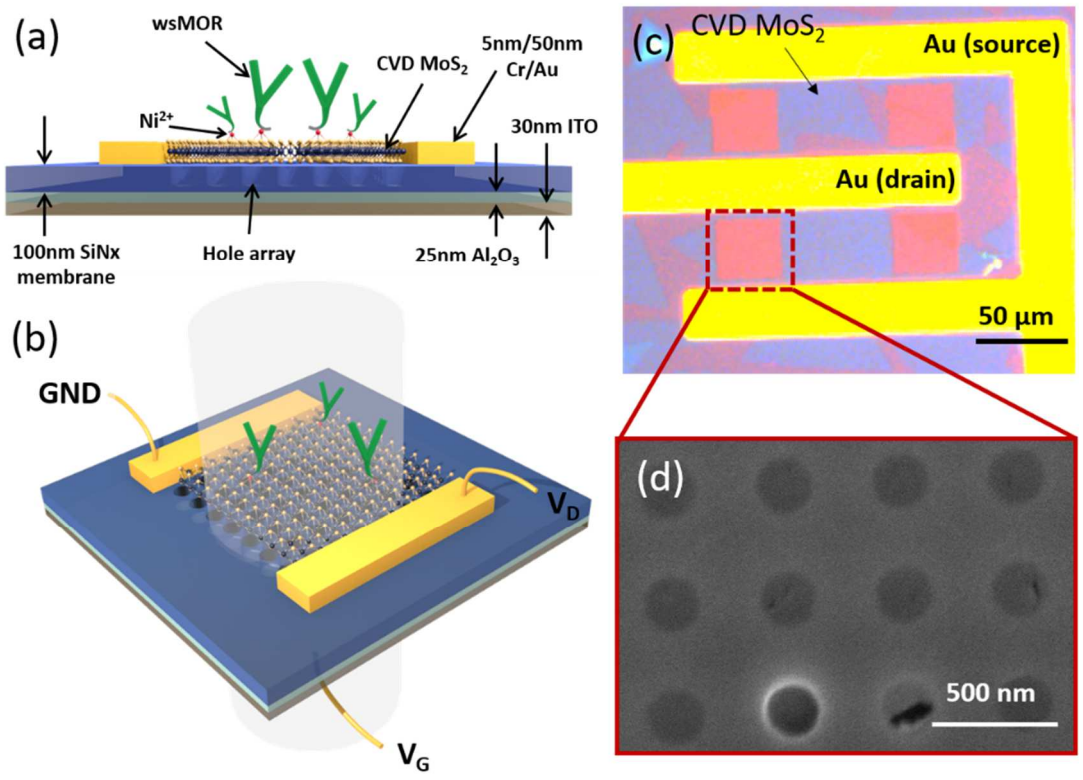

Figure 3.1: Device structure and sensing scheme.
(a) The biosensor was fabricated on a freestanding 100 nm-thick SiN membrane supported by a Si frame. On the backside of the membrane are 25 nm Al_2O_3 and 30 nm ITO. Photonic crystal slabs were fabricated directly on the SiN membrane between two Cr/Au electrodes. Large CVD MoS_2 flakes were transferred over the two electrodes and photonic crystals to create an FET and optical modulator on the same platform. (b) Sensing scheme of the dual-mode sensor with V_G and V_D connected to the gate and drain electrode, respectively, with the source electrode as a common ground. The nanohole arrays have a period of 440 nm and hole radius of 120 nm, giving rise to a Fano resonance at ~700 nm for refractive index sensing. (c) Microscope image of a device. Purple-ish blue regions are the overlaying CVD MoS_2. (d) SEM of a PhC hole array with the superimposing monolayer CVD MoS_2.

As shown in Figure 3.1c, CVD-grown MoS_2 flakes are placed over an array of nanoholes on a 100 nm thick suspended silicon nitride (SiN) membrane. Figure 3.1d shows a scanning electron micrograph (SEM) of a MoS_2-integrated square lattice hole array that makes up a PhC slab patterned lithographically between two electrodes. This PhC nanostructure exhibits optical Fano resonances which are characterized by their asymmetric line shape observable in the transmission spectra.[60] The spectral position of these Fano resonances is highly sensitive to small

changes in the local permittivity in the surrounding medium. This enables sensitive optical detection of biomolecular interactions via refractive index modulation.[61] On this device, the accumulation of target molecules on monolayer MoS_2 induces an effective increase in the refractive index surrounding the PhC slab, causing the Fano resonance peak to redshift by $\Delta\lambda$. We employ this spectral shift in the optical transmission spectra to quantify the concentration of target molecules.

Simultaneously, bound molecules modify the in-plane conductivity via electrostatic gating effects, which can be detected as a change in the channel source–drain current (ΔI_{DS}). Figure 3.1c shows a mechanically transferred MoS_2 monolayer covering the drain and source electrodes, creating a semiconducting channel. To enable nanoelectronic sensing, 25 nm alumina (Al_2O_3) and 30 nm indium tin oxide (ITO) films are deposited on the backside of the SiN PhC slab as optically transparent dielectric and back gate electrode, respectively. These crucially enable the device to support two independent modes of sensing on the same chip. Since the PhC hole arrays are etched through the SiN slab, the underlying Al_2O_3 film maintains physical and electrical isolation between MoS_2 and the ITO back gate. As a result, the device exhibits field-effect characteristics while remaining optically transparent to allow transmission measurements.

3.2 Results and Discussions

Having described the physical mechanisms involved in our sensor, we illustrate in Figure 3.1b the dual-mode operation of the device. In the FET or nanoelectronic mode, two electrical sourcemeters (Keithley 2400) were connected, respectively, to the back-gate (V_G) and drain (V_D) electrodes with the source electrode acting as the common ground. We first verified that the presence of the nanoholes on the SiN membrane did not have a significant effect on the FET characteristics. To do this, we fabricated two devices, one with PhC hole arrays etched through the

SiN_x membrane and one without. We then measured the gate-source current (I_{GS}, through ITO/Al_2O_3/SiN/MoS_2) as a function of V_G as shown in Figure 3.2a. The two devices displayed similar I_{GS} dependence on V_G, indicating that the hole arrays etched into the SiN dielectric layer did not inhibit the nanoelectric operation. The thin Al_2O_3 layer here is the key component in providing excellent electrical insulation between regions of MoS_2 suspended over nanoholes and bottom ITO back gate electrode. Without the Al_2O_3 layer, suspended monolayers can sag and come into contact with ITO under bias, which leads to electrical shorting through the structure. While this multilayer dielectric configuration provides electrical insulation on par with SiN, we still need to determine the range of voltages for which there is no dielectric breakdown for reliable operation of the dual-mode sensor. Experimental results in Figure 3.2a show that the leakage current I_{GS} increases exponentially when V_G is larger than 10 V indicating the onset of electrical breakdown. For $V_G > 20$ V, the capacitor structure can experience irreversible dielectric breakdown.[62] Therefore, for device characterization and sensing experiments, we limit the operation of the dual-mode sensor to gate voltages between $V_G = -2$ V and 5 V.

Next, we examined the transfer characteristics, I_{DS}–V_G and I_{DS}–V_D, of the MoS_2 FET. As shown in the I_{DS}–V_G curve in Figure 3.2b, we swept V_G from -2 V to 5 V at 1 V s^{-1} while keeping V_D constant, and measured I_{DS} across the electrodes. As expected, I_{DS} increased exponentially with V_G when the device is in the on-state and increasing V_D increases the channel current I_{DS}. In Figure 3.2c, we fixed V_G to obtain a relationship between I_{DS} and V_D. Device drain current I_{DS} increased linearly with V_D in the linear region and plateaued when the FET entered the saturation region at higher V_D bias. The I_G–V_{DS} and I_D–V_{DS} characteristics of our device is in good agreement with those of the previously reported MoS_2-based FETs.[63–65]

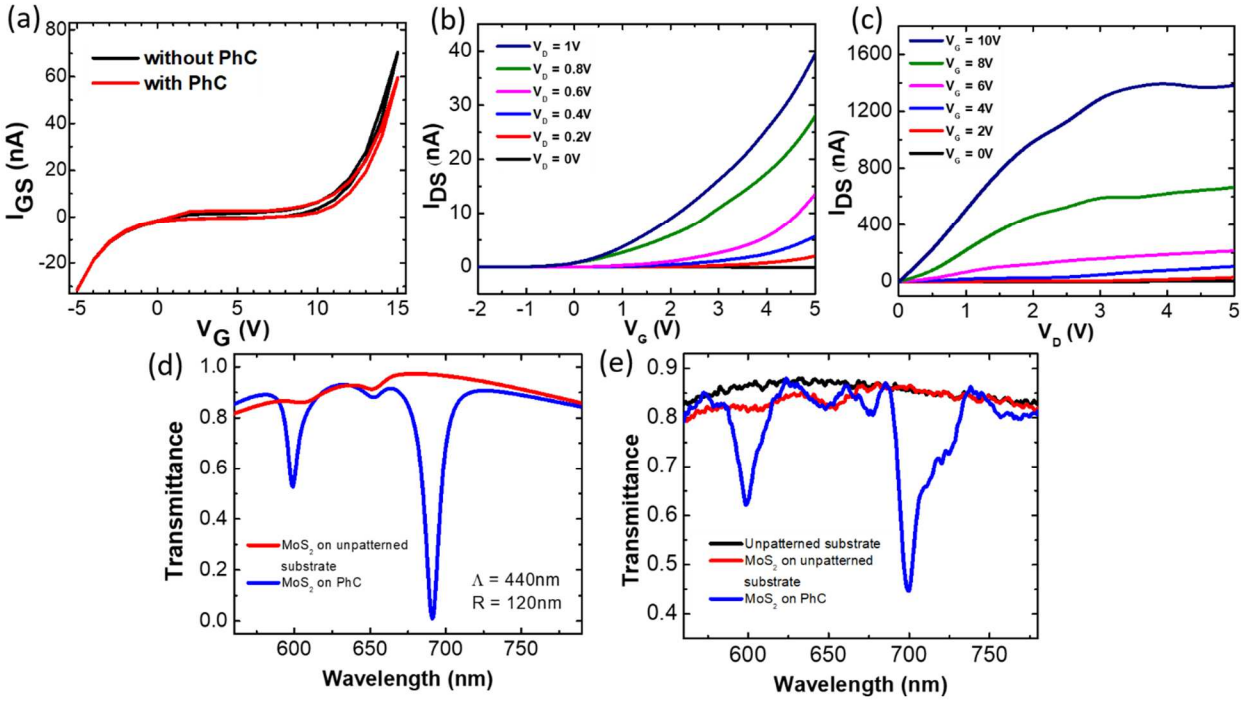

Figure 3.2: Optoelectronic device characterization.
(a) Comparison between I_{GS}-V_G curves for the device with and without PhC hole arrays. (b) I_{GS}-V_D and (c) I_{DS}-V_D characteristics for the MoS_2-based FET. (d) Simulated FDTD transmission spectra of MoS_2 on an unpatterned (red) and patterned (blue) substrate. The substrate is a 100nm-thick suspended SiN slab with 25 nm Al_2O_3 and 30 nm ITO layers on the backside. The red curve shows a slowly varying Fabry-Perot resonance due to the slab substrate. Small peaks at 650 nm and 610 nm are due to the absorption of A- and B-excitons, respectively. Patterned substrate consists of a rectangular array of nanoholes etched only through the SiN slab. The blue curve shows peaks at 690 nm and 600 nm corresponding to the first and second order Fano resonances, respectively. These resonances arise from the hybridization of 2nd order grating scattering from the nanohole array and the Fabry-Perot transmission background. (f) Measured transmission spectra for the fabricated structure. Additional peaks are attributed to nonuniformities in the fabrication process.

In the optical or nanophotonic mode, the presence of hole arrays on a suspended SiN slab gives rise to Fano guided mode resonances that can be observed via transmission measurements. Upon illumination on a SiN PhC slab, a portion of the incident light is transmitted through the uniform slab, generating a slowly varying Fabry–Perot background (red line in Figure 3.2d). This hybridizes with the remaining portion of light that excites the in-plane narrow-band guided resonance, produced by a periodic modulation in the dielectric constant over the square lattice hole

array. As a result of this interference, we observe sharp Fano-type resonances in the transmission spectra characterized by their asymmetric spectral lineshape.[66] The spectral positions of these Fano resonances can be tuned by varying the geometric parameters of the photonic crystal, such as the period and diameter of the holes.

We designed the photonic crystal to exhibit a Fano resonance at ~700 nm, spectrally away from the MoS_2 A-exciton absorption peak at 650 nm in order to minimize optical losses. Figure 3.2d shows the finite difference time domain (FDTD) method simulated transmission spectrum of a PhC consisting of a square array of holes with a radius of 120 nm and array period of 440 nm. The structure exhibits a Fano resonance at 690 nm with a theoretical quality (Q)-factor of about 60. The small spectral dip at ~650 nm corresponds to the A-exciton absorption peak of MoS_2.[2] For transmission spectrum measurements, a collimated white light source was incident on the PhC and the transmitted light was collected through a microscope objective. Figure 3.2d shows the measured transmission spectra for the fabricated structure having the same PhC parameters, with and without the MoS_2 monolayer. The spectral peaks here are in good agreement with the FDTD simulations, with the A-exciton peak at 650 nm and the first and second Fano resonances at ~700 nm and 600 nm, respectively. Additional peaks in the measured spectra are attributed to nonuniformities introduced by the fabrication process.

To demonstrate the nanoelectric and nanophotonic sensing operation in this work, we utilized a histidine-tagged water-soluble variant of the μ-opioid peptide receptor (MOR) and synthetic target opioid peptide analogue to encephalin. The native MORs are a class of opioid receptors that possess a high affinity for endogenous ligands such as enkephalin and beta-endorphin.[67] Enkephalin is a neuropeptide which serves as an important signaling molecule in the brain.[68] Sensitive detection of opioid peptides is useful in drug discovery and development.[58]

To achieve a clean surface for functionalization, a low temperature transfer method was employed as described in the methods section. This allows the PMMA layer to readily dissolve in acetone without leaving any residues on the MoS_2 surface. Atomic force microscope (AFM) images of MoS_2 surfaces before and after transfer are shown in Figure 3.8 and Figure 3.9, respectively. These confirm that the low temperature method yields a clean MoS_2 surface with very few residues. If a significant number of residues was present, functionalization would result in a lower density of immobilized probes available for detection, which would deteriorate the linear range, sensitivity, and limit of detection of the biosensor.[69] PMMA residues can also induce unintentional doping effects and scattering loss in the nanoelectronic and nanophotonic operation, respectively, which would further degrade the detection sensitivity of the sensor.[70]

Figure 3.3a illustrates the functionalization scheme for wsMOR on MoS_2 via Ni^{2+} linkers. To functionalize MoS_2, we first placed droplets of 5 mM $NiCl_2$ solution onto the device and let incubate for 1 h. In this step, Ni^{2+} ions formed coordinate bonding with sulfer atoms on the surface of MoS_2. The sample was immersed in a water bath for 5 min followed by another water bath for 20 min to remove any excess Ni^{2+} ion. Next, droplets of 10 μM wsMOR in a buffer solution were placed on the device array for 1 h, allowing the histidine tag to bind to Ni^{2+}. Finally, the sample was left in a water bath for 5 min to wash off unbound receptors and blown dry.

After functionalization, the immobilization of wsMOR was verified via atomic force microscopy. An SEM of a functionalized MoS_2 monolayer is shown in Figure 3.3b. Figure 3.3c and Figure 3.3d show the surface morphology of MoS_2 flakes before and after functionalization, respectively, indicating uniform protein coverage. The surface of transferred MoS_2 was uniform and relatively flat. The flake thickness was about ~1 nm (Figure 3.3e) which agrees well with the reported AFM measurements of CVD-grown monolayer MoS_2.[55,71,72] After functionalization with

Ni^{2+} and wsMOR protein, the thickness of MoS_2 flakes uniformly increased to ~3 nm (Figure 3.3f). This change is consistent with the 46 kDa size of wsMOR.[59] The surface of the substrate remained flat and featureless which indicates specific attachment of wsMOR on MoS_2 surface only. This mechanism of protein attachment on MoS_2 allows binding of target molecules to occur very close to the sensing surface.

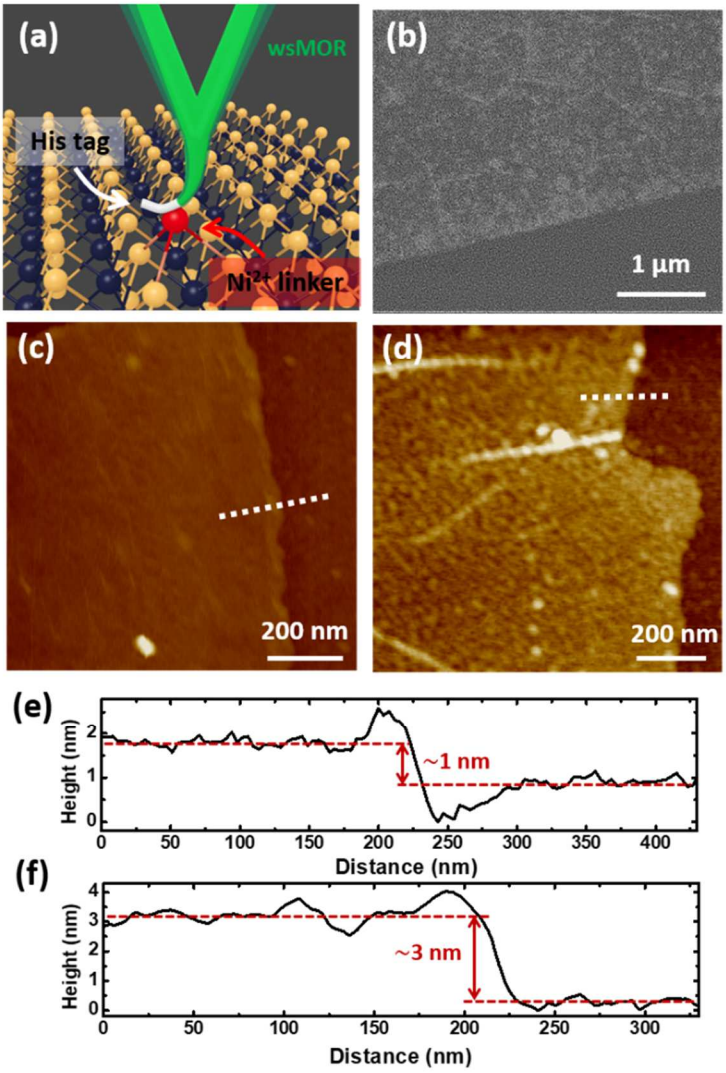

Figure 3.3: MoS_2 functionalization.
(a) Schematic for the linker chemistry for direct functionalization. The red atom represents Ni^{2+} that is bound to the sulfur atoms on MoS_2 via coordinate bonds. The white region on wsMOR represents the histidine tag that binds preferentially to the Ni^{2+} ions. (b) SEM of wsMOR-functionalized MoS_2. (c) AFM topographic image of unfunctionalized transferred CVD MoS_2 on SiO_2, (d) wsMOR-functionalized MoS_2 on SiO_2. (e,f) Height profiles of the line scan shown in (c) and (d), respectively.

As a result of wsMOR functionalization, the drain current of the device increased by ~8 times, indicating an increase in channel conductance (Figure 3.4a). The hysteretic behavior between the forward and backward voltage sweeps are attributed to adsorption of ambient molecules on the surface of MoS_2 and charge trapping between the monolayer and substrate.[73] We note that the functionalization process may either increase or decrease MoS_2 channel conductance depending on the quality and initial doping of the MoS_2 flakes. Meanwhile, the Fano resonance red-shifted by 3 nm due to the increased refractive index surrounding the MoS_2-integrated PhC slab (Figure 3.5a).

Dual-mode sensing experiments were carried out with target DAMGO synthetic opioid peptide diluted in deionized water. To test the sensor response, we exposed the device to target DAMGO in DI water at different concentrations, ranging from 0.1 nM to 10 μM. For each concentration, droplets of target DAMGO solution were placed on the device for 30 min. Then the device was rinsed in a DI water bath for 2 min and blown dry with a nitrogen gun. We note that we do not expect the target DAMGO to bind to the Ni^{2+} linkers as they do not contain histidine residues (Ni^{2+} binding sites) as in the histidine-tagged wsMOR.[74] Therefore, a blocking agent was not necessary to deactivate the linker ions.

Current and transmission measurements were carried out sequentially at each concentration to obtain the dual-mode sensor responses. The dual-mode sensing responses as a function of DAMGO concentration are presented in Figure 3.4b and Figure 3.5b, respectively, as a percent change in channel current, ΔIDS/I0, and resonance peak shift, Δλ, with respect to responses of the functionalized device. For nanoelectronic sensing, we swept V_G from −2 V to 5 V at 1 V s^{-1} and a constant V_D of 0.1 V. This small value of V_D was used to keep the channel current small in order to avoid any heating effects. The current responses for different DAMGO concentrations were

extracted at $V_G = 2.5$ V, halfway between the turn on voltage and maximum voltage applied. For nanophotonic sensing, the measured transmission spectra were first fitted near the first Fano resonance. The peak positions were then obtained from the fit for each DAMGO concentration. Both curves were fitted by the Langmuir–Hill equation

$$\theta = A\frac{[C]^n}{(K_a)^n + [C]^n} + Z \tag{3}$$

where $\theta = \Delta I_{DS}/I_{DS,0}$ or $\Delta\lambda$ is the sensor response representing the fraction of wsMOR that is bound to DAMGO, $[C]$ is the DAMGO concentration, K_a is the DAMGO concentration that produces half of the maximum response, A is the maximum response, Z is the offset response, and n is the Hill coefficient. The dissociation constant describing binding affinity is described as $K_d = (K_a)^n$.

Responses in both modes exhibit similar trend as they scale with the fraction of conjugated wsMOR on MoS surface. The electrical response in Figure 3.4b is fitted with $K_a = 1.2$ nM, $A = 145$ and $n = 0.87$, and the optical response in Figure 3.5b with $K_a = 1.0$ nM, $A = 1.86$, and $n = 0.91$. Figure 3.4c and Figure 3.5c show normalized response of three devices. We extracted averaged fitting parameters to be $K_a = 1.5 \pm 0.4$ nM and $n = 0.87 \pm 0.01$ for the nanoelectronic response, and $K_a = 1.2 \pm 0.2$ nM and $n = 0.89 \pm 0.02$ for the nanophotonic response. These yield the dissociation constants, K_d, for DAMGO-wsMOR interaction of 3.6 ± 0.5 nM and 2.5 ± 0.8 nM as obtained via electronic and optical modes, respectively. These values are also in good agreement with previously reported K_d of MOR for DAMGO.[75,76] Despite using different transduction mechanisms, we found the two K_d values to be remarkably close. This evidently demonstrates the independent operation of the two systems, allowing us to consistently probe biomolecular binding events via two distinct physical mechanisms on the same device.

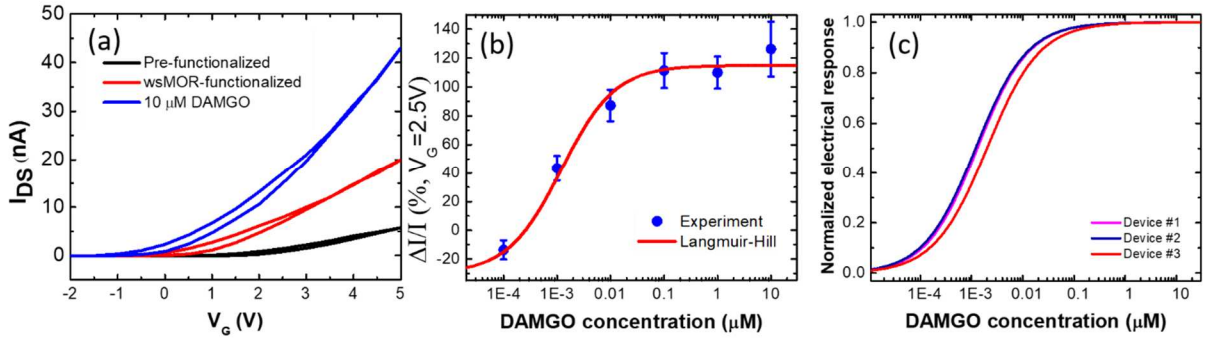

Figure 3.4: Nanoelectronic sensing.

(a) I_{DS}-V_G characteristics of the sensor pre-functionalization (black), after functionalization with wsMOR (red), and after exposure to 10 μM DAMGO (blue). V_D = 0.1 V. (b) Electronic response reported as percentage change in I_{DS} with respect to the I_{DS} of wsMOR-functionalized device, extracted from I_{DS}-V_G curve at V_G=2.5V. Error bars represent the standard deviation of the mean between three repeated measurements. The experimental data was fitted by the Langmuir-Hill isotherm to obtain the sensor calibration curve for the nanoelectronic mode (red). (c) Normalized electronic response of three different devices.

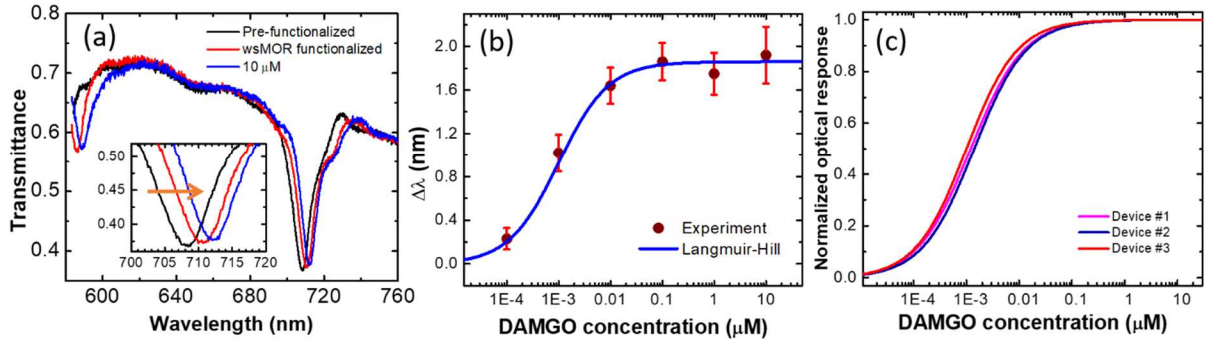

Figure 3.5: Nanophotonic sensing.

(a) Transmission spectra of the sensor pre-functionalization (black), after functionalization with wsMOR (red), and after exposure to 10 μM DAMGO (blue). (b) Optical response reported as resonance wavelength shift with respect to the resonance peak position of wsMOR-functionalized device. Error bars represent the standard deviation of the mean between three repeated measurements. The experimental data was fitted by the Langmuir-Hill isotherm to create the sensor calibration curve for the nanophotonic mode (blue). (c) Normalized optical response of three devices.

For both modes, the limit of detection is about 0.1 nM as limited by electrical noise and the spectral resolution of the instrument. Since the sensor responses both scale with surface coverage of the target peptide, the linear range of the sensor is approximately 0.1–10 nM for both modes of operations. The sensitivity of the sensor is extracted from the slope of the fit in the linear range, yielding the sensitivity as a percent change of drain current per unit target concentration of 10.5% nM^{-1}, and spectral displacement per unit concentration of 0.15 nm nM^{-1}. We also note that the sensing area and photonic crystal design on this device can be independently optimized further to improve the sensitivity while maintaining dual-mode operation. The combination of two sensing modes can further improve the accuracy of detection by reducing the margin of errors in the individual sensor responses and provide great flexibility in modes of operation.

3.3 Conclusion

In summary, we demonstrate here a dual-mode optoelectronic biosensor based on CVD-grown monolayer MoS_2 as an active multifunctional element. The device is composed of a MoS_2-based FET fabricated on a SiN PhC slab exhibiting an optical Fano resonance. ITO back gate electrode and Al_2O_3 dielectric layer keep the device transparent for transmission measurements and prevent electrical shorting through the nanoholes. These allow the device to support two modes of sensing simultaneously. The monolayer MoS_2 acts as a protein immobilization surface, active functionalization layer for nanophotonic refractive index sensing via Fano resonance tuning, and FET channel for nanoelectronic sensing. With our present design, the percent yield of working devices is about 70%, due to the flakes having to both bridge two electrodes and cover a photonic crystal hole array. We note that a different device layout could increase the yield further. Our previous work demonstrated a large scale production of similar FET biosensors using CVD-grown

MoS_2, achieving a yield of over 90%.[59] Therefore our proof-of-concept demonstration of the dual mode sensor can readily be extended to large area fabrication with reasonably high yield in the future. To demonstrate dual-mode operation, the sensor was functionalized with wsMOR, and used to determine the affinity of DAMGO as a function of concentration via electrical and optical measurements. The sensor responses were read out in terms of percent change in drain current I_{DS} and wavelength shift for the Fano resonance in the nanoelectronic and nanophotonic modes, respectively. Both responses agreed well with the Langmuir–Hill model for ligand-receptor binding and exhibited binding constants within the same range as those previously reported in literature using radio-active materials. This approach not only avoids using radio-active materials, but also combining two readouts can increase the accuracy of results by reducing uncertainty that arises from each individual mode, such as calibration and systematic errors. The design can potentially be optimized to provide extensive measurements of biomolecular processes, improved dynamic sensing range and sensitivity and flexibility in mode of operation. Our work shows that the unique physical, chemical, electronic, and optical properties of monolayer MoS_2 can open up new opportunities for the design of multimodal biosensors.

3.4 Methods

3.4.1 Device fabrication

An array of devices was fabricated on a freestanding 100 nm-thick silicon nitride membrane (Norcada), which provided a transparent substrate for transmission measurements. First, 20 nm Al_2O_3 was grown on the backside of the substrate by atomic layer deposition (ALD) at 200 °C. This was followed by deposition of 30 nm ITO by RF sputtering. Next, we used photolithography to pattern electrodes on the front side of the substrate; 5 nm Cr and 50 nm Au

were deposited via electron-beam evaporation and lifted off to form electrodes. Hole arrays were patterned in between electrodes on the SiN membrane via electron-beam lithography. The holes were formed by dry etching through the SiN slab via reactive ion etching (RIE) with O_2 and CHF_3 gases with Al_2O_3 layer on the back side acting as an etch stop layer.

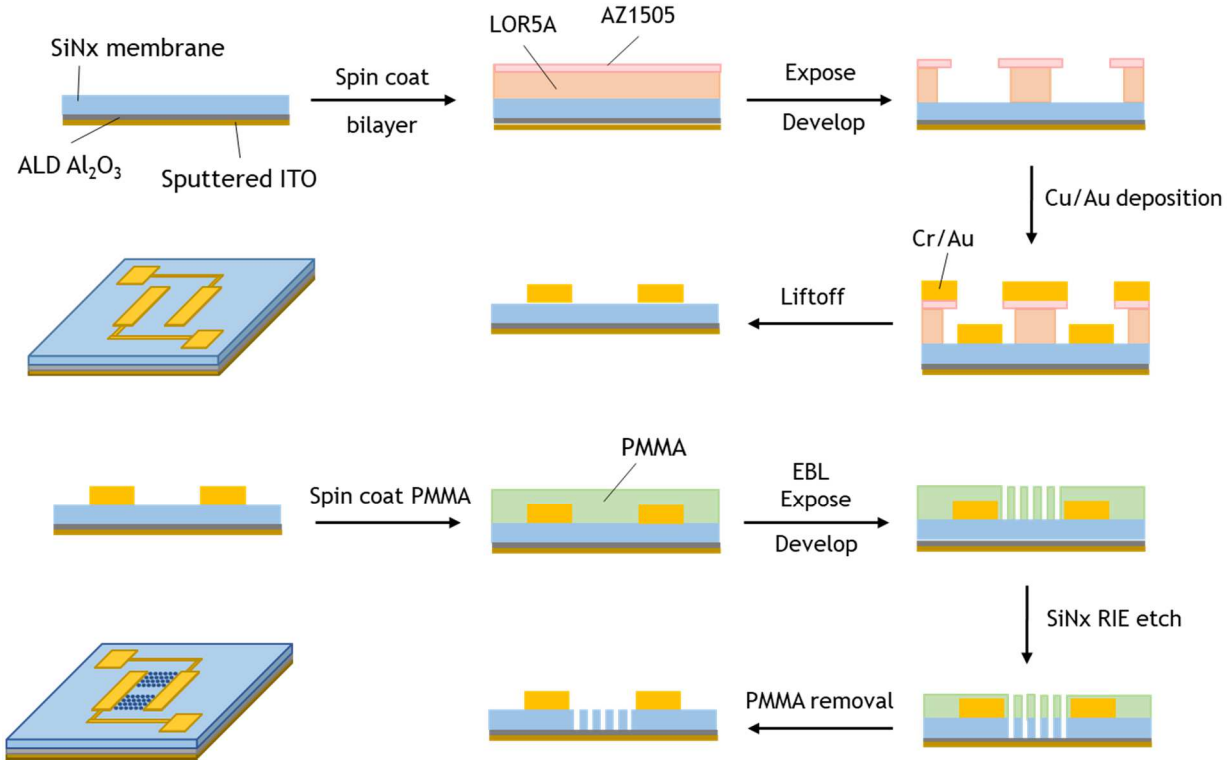

Figure 3.6. Fabrication of dual-mode optoelectronic biosensor.

3.4.2 CVD MoS_2 transfer

After the electrodes and hole arrays were fabricated, flakes of CVD-grown MoS_2 were transferred onto the devices by wet transfer. We first spin-coated PMMA (500 nm–1 μm thick) on as-grown MoS_2 flakes on a SiO_2/Si substrate. Next, the sample was left floating in a bath of 0.1 M NaOH to etch SiO_2, releasing the PMMA film from the underlying substrate. The floating PMMA film was carefully scooped up with a glass slide and released in three sequential DI water baths to

wash off any NaOH. The PMMA film was then scooped up from the last water bath with the patterned SiN membrane chip, and the sample was blown dry with a N_2 gun until the water droplets visually disappeared. Then the sample was left to further dry in a desiccator for at least 2 h. To remove PMMA, the sample was submerged in an acetone bath for 30 min, followed by a second acetone bath for 1 h. Finally, the sample was placed in an IPA bath for 10 min to remove acetone and blown dry. The finished device underwent a current annealing process prior to measurements. With constant $V_G = 10$ V, V_D was slowly increased from 0.1 V to 3 V and left for 2 min. Prior to sensing experiments, transferred MoS_2 flakes on the device were functionalized with wsMOR as described in main text.

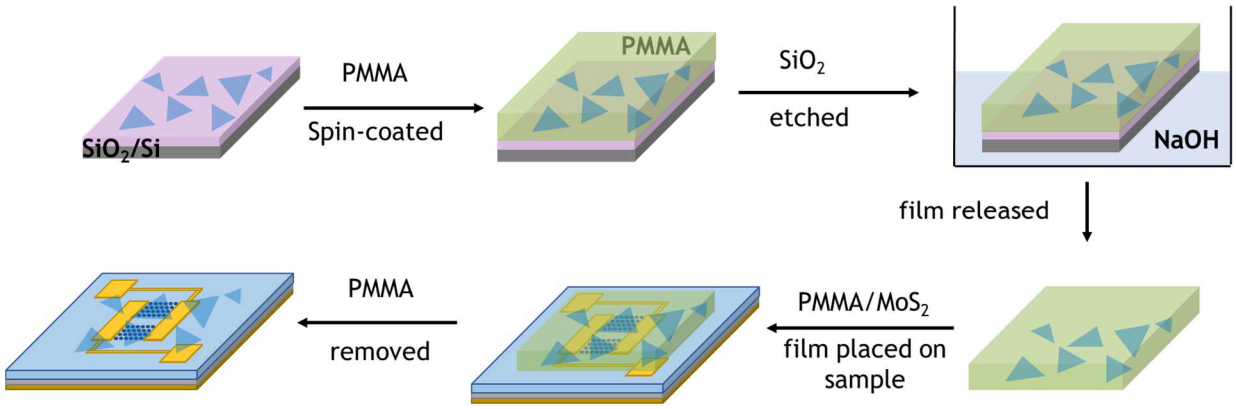

Figure 3.7: Wet transfer process of CVD-grown MoS_2.

3.4.3 Cleanliness of MoS_2 surface

To directly functionalize the MoS_2 surface, we need to make sure that the transferred flakes are free of residues that could be generated during processing. The MoS_2 transfer process used in this work is outlined in section 3.4.2.

To demonstrate the cleanliness, we probed the surface profile of as-grown and transferred MoS_2 via atomic force microscopy (AFM). Figure 3.8a and Figure 3.8b show clean and flat

surfaces of CVD-grown MoS_2 before PMMA transfer. The profile of the dotted line is presented in Figure 3.8c, showing a flake thickness of about 1 nm and flat surface. After a heatless transfer process, we again examined the surface of the transferred MoS_2 flakes. As shown in Figure 3.8d and Figure 3.8e, some wrinkles are visible as a result of the transfer, but the surfaces remain clean when PMMA was removed. Figure 3.8f shows the profile of the dotted line across the edge of the flake in Figure 3.8d.

For comparison, we repeated the process using a heat-assisted transfer process. The PMMA film was gradually heated to 150°C and kept at the temperature for 30 minutes. Then PMMA film was removed in acetone baths the same way as described in section 3.4.2. In Figure 3.9a, large residues can be seen on the flake. The profile in Figure 3.9b shows large bumps of 2-8 nm in height.

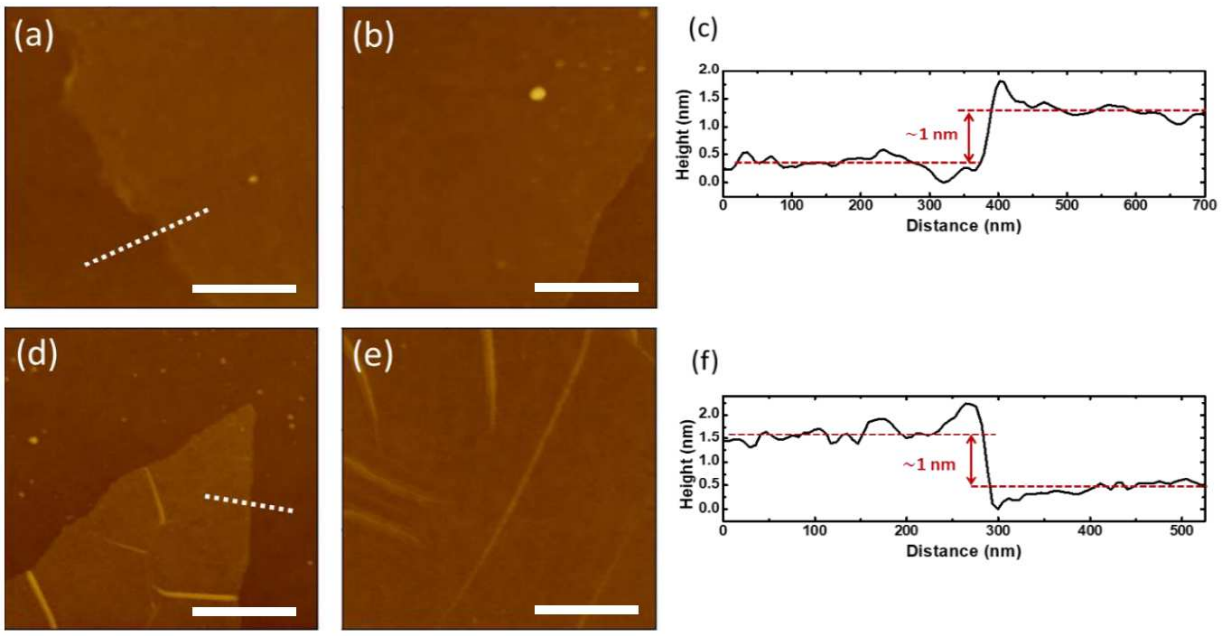

Figure 3.8: AFM characterization of MoS_2 surface after heat-less transfer.
(a,b) AFM image of as-grown CVD monolayer MoS_2. Profile across the dotted line in (a) is shown in (c). (d,e) AFM image of transferred MoS_2 via the low temperature method. Wrinkles as a result of transfer are visible, but the surface remains clean and flat comparable to the as-grown MoS_2. Profile across the dotted line in (d) is shown in (f). Scale bars, 500nm.

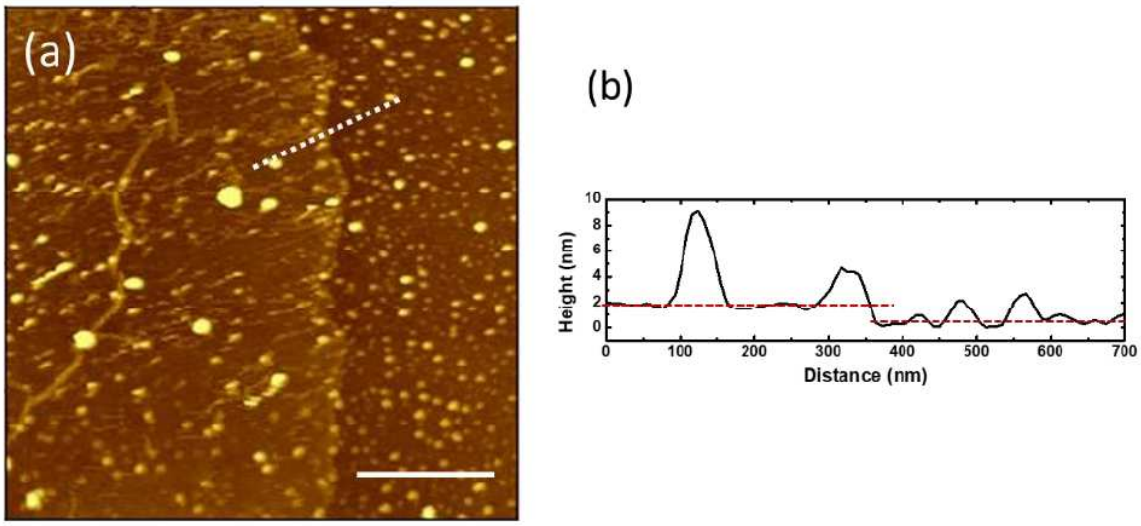

Figure 3.9: AFM characterization of PMMA residue on transferred MoS_2.
(a) AFM of transferred MoS_2 in which PMMA film was exposed to heat. PMMA residues can be seen after PMMA film was dissolved in acetone bath. (b) Profile across the dotted line in (a). Residues of heights 2-8 nm were observed. Scale bar, 500nm.

A small amount of residues taking up less than 1% of the surface area would not cause an appreciable degradation of the sensing performance. However, a large number of residues as a result of transfer processes could deteriorate the detection capability of any 2D material-based biosensors. Specifically for our dual-mode biosensor, the presence of residues, especially in large amount, can inhibit the direct functionalization of protein probes on MoS_2 surface, resulting in a lower density of immobilized probes for detection of target molecules.[69] Since our device relies on biomolecular interactions on MoS_2 surface, the sensing responses in both modes of operation scale proportionally with a fraction of target-bound probes. Having fewer number of probe binding sites available for detection would, therefore, negatively affect the linear range of operation, sensitivity and limit of detection of the biosensor.[77]

In addition to the decreased density of immobilized protein probes, PMMA residues themselves can further degrade the detection sensitivity by inducing doping effects and scattering loss in the nanoelectronic and nanophotonic operation, respectively. For FET-based sensing,

PMMA residues act as p-type dopants to MoS_2.[70] This results in decreased the charge density and increased the resistance in the MoS_2 channel.[78] In transmission measurements, the presence of residues reduces the quality factor of the Fano resonance peak due to scattering, broadening the width of the peak. This reduces the degree of reduced spectral shift during detection and limits the sensitivity of the biosensor.

3.5 Acknowledgements

Chapter 3, in full, is a reprint of the material as it appears in MoS_2-enabled dual-mode optoelectronic biosensor using a water soluble variant of μ-opioid receptor for opioid peptide detection. De-Eknamkul, Chawina; Zhang, Xingwang; Zhao, Meng-Qiang; Huang, Wenzhuo; Liu, Renyu; Johnson, A. T. Charlie; Cubukcu, Ertugrul. 2D Materials, 2020. The dissertation author was the primary researcher and author of this paper.

CHAPTER 4 - OPTICAL VOLTAGE SENSING OF ELECTROPHYSIOLOGICAL SIGNALS WITH MONOLAYER MoS_2

4.1 Introduction

The ability to monitor electrical activity of neural networks is crucial in understanding the coordinated communications of neurons. Electrode-based measurements and fluorescence-based reporters, especially calcium indicators, have long been the gold standard of extracellular electrophysiological recording. However, these traditional electrical and optical approaches often carry trade-offs between spatial flexibility, temporal resolutions, recording duration and cell perturbation. Microelectrode arrays (MEAs) detect ion induced voltage changes in the environment and allow simultaneous recording across multiple sites with sub-millisecond resolution. But as electrical readouts contain the sum of voltage signals from all surrounding sources, the ability to target and distinguish specific cells is restricted. The fixed and sparse recording sites in prefabricated electrode arrays also limit the spatial resolution and flexibility of measurements.[79] On the other hand, optical detection offers superior spatial control, imaging capability and cell-type specificity. Calcium indicators utilize a fluorescent molecular probe that changes its emission intensity with concentration of calcium ions.[80] Neural activity is detected as a sharp increase in fluorescence intensity as the local calcium ion concentration rises. Although this method is versatile and compatible with a wide range of neural populations, calcium transients are indirect markers of neural activity and do not fully embody the polarization phases of an action potential.[80,81] Molecular probes also suffer from slow kinetics, leading to temporal responses that are longer than the millisecond neuron dynamics.[82] Prolonged exposure to light can further cause photobleaching and generate phototoxic species that interfere with cellular functions, ultimately limiting the recording duration.

Given the drawbacks of each method, a label-free technique that directly coverts electrical signals into optical readouts can bridge the gap between electrode-based and fluorescence probe-based technologies. In recent years, several groups have employed low dimensional materials and structures as optical reporters to enable label-free electrophysiology.[83] Integration of nanoscale features can facilitate and enhance interactions between extracellular electric fields and light, providing a mechanism for optical transduction of electrical activity. A popular approach utilizes the voltage-tunable absorption of electrochromic materials to modulate the properties of incident light. One such material is poly(3,4-ethyl-enedioxythiophene) polystyrene sulfonate (PEDOT:PSS). Voltage fluctuations within the vicinity of PEDOT:PSS induce small changes in material absorption that can be detected optically as changes in reflectance, transmittance, or scattering. Improved voltage sensitivity can be achieved by employing prism-coupled total internal reflection configuration[84] or embedding plasmonic nanoantennas to increase scattering signals.[85] In a similar fashion, graphene's tunable absorption has been shown to respond to local electric fields.[86] Combined with a critically coupled planar waveguide, total reflectance change can be amplified to increase voltage sensitivity.[87,88] These works successfully demonstrated non-perturbative and label-free optical voltage sensors that interface with and transduce electrical signals from biological specimens. However, in their preliminary stages, label-free platforms still exhibit small fractional changes in optical signals and limited temporal resolution. They also often require complex optical systems that hinder their imaging capabilities. The search for nanoscale methods thus continues to find versatile platforms to effectively monitor electrical signals across neuron populations.

To this end, we introduce monolayer molybdenum disulfide (MoS_2) as a novel label-free optical voltage sensor exhibiting large optical changes, excellent spatiotemporal resolution, and

biocompatibility. In this first study, we characterized the voltage-dependent photoluminescence (PL) modulation of chemical vapor deposition (CVD) grown monolayer MoS_2 in a phosphate buffered saline (PBS) solution. We discussed exciton-trion conversion as the primary mechanism for PL intensity modulation. By applying an external voltage and measuring the PL response, we reported a voltage sensitivity at 1 kHz of 2.46 %/mV and 1.73 %/mV for negative and positive voltage changes, respectively, and estimated the minimum detectable voltage to be 9.4 $\mu V/\sqrt{Hz}$. The optical response exhibits a bandwidth of over 20 kHz thanks to the PL radiative lifetime of tens of picoseconds.[89,90] We further demonstrated MoS_2 PL imaging using one- and two-photon excitation, proving its direct compatibility with conventional fluorescence imaging systems. Lastly, we showed that the viability of human induced pluripotent stem cells (hiPSC) derived neuron cultures replated on MoS_2 devices. The findings in this study revealed the feasibility of monolayer MoS_2 as an all-optical label-free voltage sensor for real-time detection of neural activity.

4.2 Results and Discussions

Monolayer MoS_2 can be seen as a semiconducting analog of semi-metallic graphene and is distinguished from its multilayer forms by the characteristic direct electronic bandgap.[45] The presence of this direct bandgap transition gives monolayer MoS_2 an appreciable room-temperature PL emission. Because of the sub-nanometer thickness, the radiative properties of monolayer MoS_2 are dictated by the effects of quantum confinement, giving the PL emission sensitivity to the local fluctuations of external electric fields.[91,92] Combined with the fast temporal dynamics, MoS_2 PL emission provide a way to convert electrical activity into PL signals.

The dynamic tunability of MoS_2 PL originates from the exciton charging effects.[93] In a single layer MoS_2, photo-excited electrons and holes are constrained to the two-dimensional plane and experience enhanced electrostatic Coulomb interactions, forming bound electron-hole pairs known as excitons. Unlike excitons in the bulk semiconductors, these 2D-confined excitons are subjected to weaker dielectric screening from the lower permittivity environment. As a result, they exhibit a large binding energy of hundreds of meV, making them energetically stable even at room temperature.[94,95] Within tens of picoseconds after their formation, excitons decay via radiative electron-hole recombination to emit strong excitonic luminescence that we can detect using fluorescence spectroscopy. Comprised of one electron and one hole, an exciton bears a resemblance to an atom with hydrogenic states. This atom-like nature allows an exciton to accept an additional charge carrier, either an electron or hole, to form the equivalent of an ionized atom known as a trion.[96] For instance, a free electron can bind to a photo-excited exciton to form a negatively charged trion consisting of two electrons and one hole. The larger effective mass trions decay in a similar fashion to emit lower energy photons and much weaker luminescence than excitons, effectively reducing the total emission intensity. Probabilistically, both excitons and trions exist with different densities in MoS_2 depending on its intrinsic carrier concentration and surrounding charges. When monolayer MoS_2 is illuminated with a laser, the subsequent radiative process involves a combination of exciton and trion luminescence with different contributions to the total PL emission. Based on this concept, we characterized the response of MoS_2 PL to external voltages in an aqueous solution and evaluated its performance for electrophysiological recording applications.

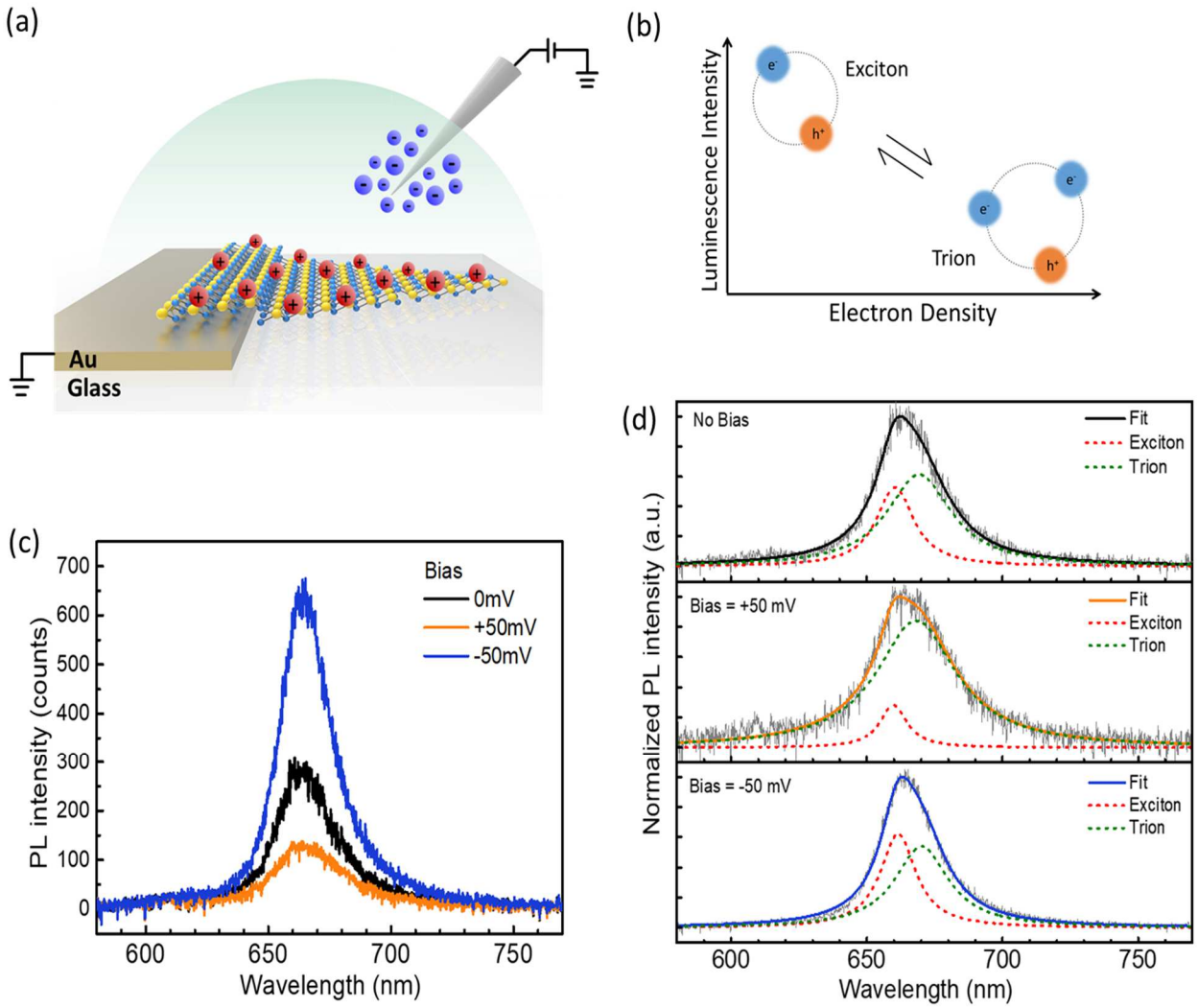

Figure 4.1: Voltage-dependent photoluminescence of monolayer MoS_2.
(a) Schematic of electrochemical gating of monolayer MoS_2 in PBS. (b) Conversion between photoexcited exciton and trion. At increased electron density, an exciton can bind to a free electron to form a less luminescence trion. The exciton-to-trion ratio determines the overall emission intensity. (c) MoS_2 PL spectra in PBS as a function of applied voltage. Black, orange and blue curves indicate a bias between the Ag/AgCl electrode and MoS_2 of 0 mV, 50 mV, and -50 mV, respectively. (d) Analysis of voltage-dependent PL spectrum with an applied bias. Exciton (red dotted lines) and trion (green dotted lines) luminescence contributions were extracted by fitting two Lorentzians. Solid black, orange and blue lines show the spectral fitting for 0 mV, 50 mV and -50 mV biases, respectively.

To demonstrate the feasibility of this mechanism, we performed a voltage-dependent PL spectroscopy on monolayer MoS_2 in a PBS solution. We used commercially available monolayer MoS_2 flakes grown by chemical vapor deposition (2D Semiconductors) where flake size ranging

from 10-50 μm with a median width of about 20 μm. We fabricated the test device by transferring a film of MoS_2 flakes from its original SiO_2/Si substrate via a polymer-assisted process, onto a glass coverslip with predefined gold electrodes. The electrodes were entirely encapsulated by 4 μm SU-8 except for a 10x10 μm opening for contacting individual MoS_2 flakes. Detailed fabrication process can be found in section 4.4.1. During experiments, the sample was covered in a large PBS droplet and a Ag/AgCl electrode was inserted into the solution. All PL spectra were obtained from MoS_2 samples in PBS unless indicated otherwise. We discuss the effect of PBS on the PL in section 4.4.2. As illustrated Figure 4.1a, the MoS_2/Au electrode, PBS, and Ag/AgCl electrode formed an ionic liquid field-effect capacitor structure that allowed us to apply external voltages on MoS_2 via electrochemical gating (section 4.4.3).[97–99] In Figure 4.1c, we applied DC biases through the Ag/AgCl electrode with respect to MoS_2 and measured the resulting PL spectra. We observed that the overall PL intensity varied substantially with the bias, decreasing and increasing with positive (orange) and negative (blue) voltages, respectively. The results are consistent with the electric field-induced movements of ion in an electrochemical cell. When a positive voltage is applied, the positive ions in PBS are repelled from the Ag/AgCl electrode and accumulated on the negatively charged MoS_2 surface.[100] This electric double layer (EDL) comprised primarily of positive ions in turn draws electrons onto MoS_2, increasing n-doping in the material. The increased electron density leads to formation of less luminescent trions and subsequently lowers the total PL intensity (Figure 4.1b). Conversely, a negative bias generates in p-doing and reduces electron density in MoS_2. This suppresses formation of trions in favor of more radiative excitons which manifests in the large increase in the total PL intensity. To verify this, we analyzed the PL spectra to quantify the excitonic and trionic contributions to the overall PL emission in each case. The slight spectral shift between exciton and lower energy trion

luminescence allowed us decompose each spectrum into two Lorentzian curves with spectral peaks at 660 nm and 670 nm, respectively.[95] The top panel in Figure 4.1d shows a large luminescence contribution from the negatively charged trions in the PL spectrum when no external voltage is applied. This is consistent with the n-doped nature of CVD-grown MoS_2 due to the inherent sulfur vacancy defects formed naturally during the growth process.[101,102] In the following panels, we see that the total PL intensity is dependent on the relative contribution of excitons and trions. The presence of a positive (negative) potential difference decreases the exciton (trion) density and increases the trion (exciton) density, as evident in the lower (higher) PL intensity measured. This unique luminescence manipulation mechanism gives us a way to probe the polarity of voltage fluctuations based on the relative change in the PL amplitudes.

Having evaluated the effect of external voltages on PL emission, we moved to characterize its response to high frequency voltages. Figure 4.2a shows the biasing and optical measurement schematics used to manipulate and record PL changes in real time. Here, we used an arbitrary function generator for applying periodic waveforms, an avalanche photodiode (APD) for measuring high frequency PL changes, and a DAQ for streaming and recording data at a high sampling rate up to 250 kS/s. In a recording, we continuously excited a MoS_2 flake using a 532 nm laser and applied a modulating bias between the Ag/AgCl electrode and MoS_2, while simultaneously probing the PL emission intensity. We first measured the PL response to a square wave bias modulating from 0 mV to a range of amplitudes (V_a) at 1 kHz, a frequency relevant to the electric field dynamics of neuronal action potentials. As seen in Figure 4.2b, the PL response exhibited the same waveform as the bias, increasing when V_a is negative and decreasing when V_a is positive. The amplitude of the PL response also increased with the magnitude of V_a, as can be seen in Figure 4.2c, where the fractional PL change ($\Delta F/F$) varied linearly as a function of V_a.

Using the slope of the linear fits, we extracted the sensitivity of MoS_2 PL to voltage changes and estimated the voltage detection limit to be 2.46 %/mV and 9.4 μV/√Hz for negative voltages, and 1.73 %/mV and 13 μV/√Hz for positive voltages, respectively (section 4.4.4).

To investigate the temporal response of MoS_2 PL, we varied the frequency of the bias. In Figure 4.2d, we show the PL response to square wave biases modulating between -5 mV and 5 mV at 100 Hz, 1 kHz and 10 kHz. Even at 10 kHz modulation, the PL response maintains a square waveform, closely following the shape of the applied voltage. This suggests the PL response time to voltage changes on the order of several microseconds. The temporal bandwidth was obtained by sweeping the frequency of a 10 mV_{pp} sinusoidal wave between 10 Hz and 80 kHz. As shown in Figure 4.2e, the response amplitude ΔF/F remained constant well beyond 1 kHz and exhibited a 3 dB cutoff frequency of over 50 kHz. The red solid line shows the simulated bandwidth calculated from a simplified equivalent circuit model and taking into account the 100 kHz bandwidth of the APD. This temporal response is sufficiently fast to keep up with the millisecond neuron dynamics, allowing us to directly convert neuronal signals into optical readouts. In Figure 4.2f, we mimicked the neuronal signals using an arbitrary function generator. The upper panel shows the applied action potential waveform with 12 mV_{pp} repeating every 5 ms. Each spike is less than 1 ms long and followed by a refractory period. The corresponding PL response is shown in the lower panel. Sharp spikes in the optical signal can be clearly observed. MoS_2's fast optical response and high voltage sensitivity, therefore, give us a means to optically read out extracellular electrical activity of neural populations. We note that the performance of the voltage sensor should be further investigated and improved by exploring the effects of chemical treatments and photonic nanostructures to enhance light absorption and PL emission.

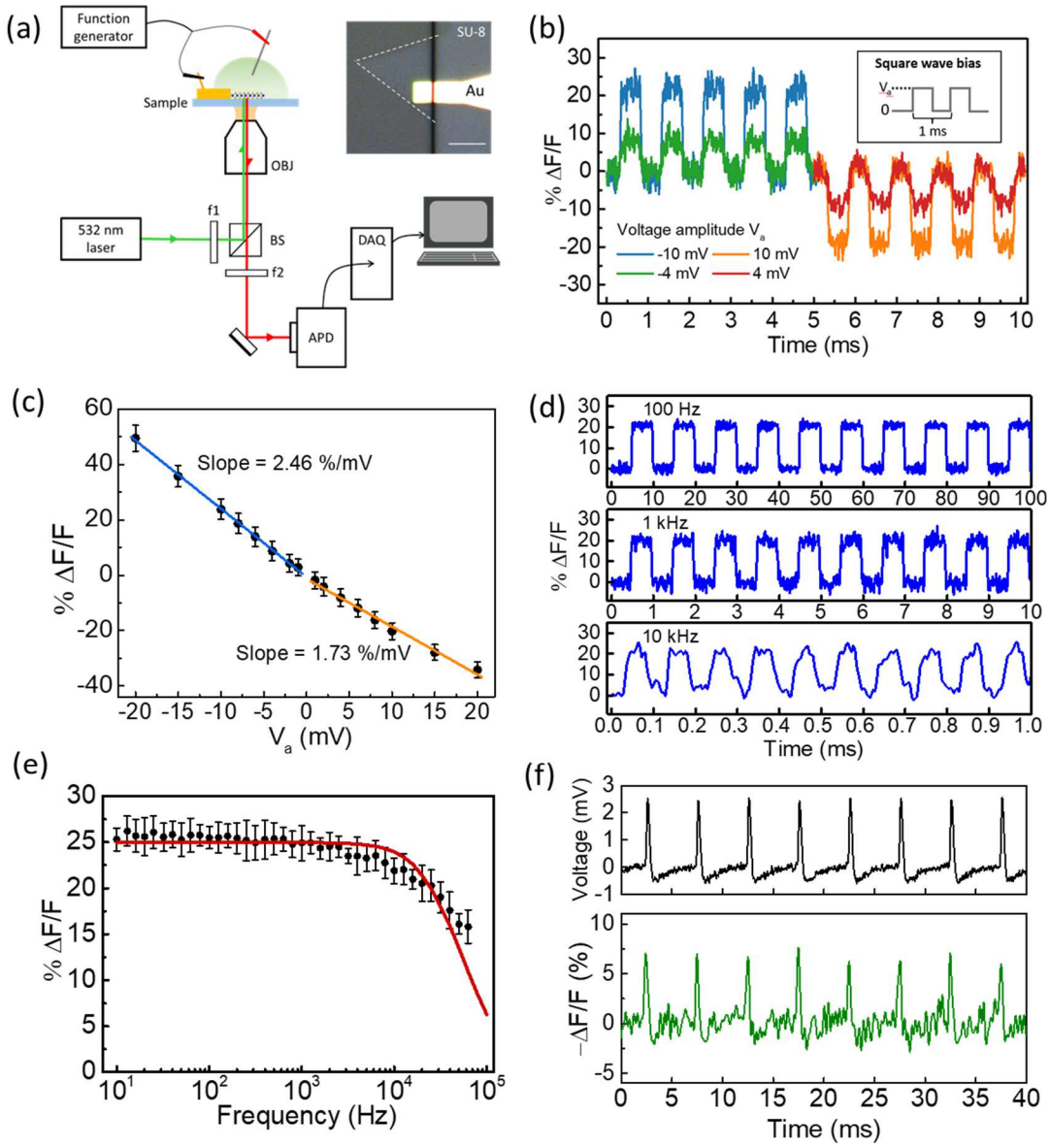

Figure 4.2: Characterization of MoS_2 PL response to high frequency voltage modulation. (a) Measurement schematic for frequency PL modulation. MoS_2 is excited using a 532 nm continuous wave laser focused onto the sample by a 1.4 NA oil immersion objective. The sample substrate is a 170 µm thick glass coverslip. Biases were applied between Ag/AgCl electrode and MoS2 in PBS. OBJ – Objective, BS – Beam splitter cube, f1 – Laser-line filter, f2 – Collection filter, APD – Avalanche photodiode, DAQ – data acquisition block. Subset, monolayer MoS_2 triangle on Au electrode. Scale bar 20 µm. (b) PL response to an applied square wave bias at 1 kHz, reported as percent change in luminescence intensity. The square wave bias modulated between 0 and V. The PL response to modulation amplitudes of -10 mV, -4 mV, 4 mV and 10 mV are shown in blue, green, red and orange, respectively. (c) PL response as a function of modulation amplitude. Error bars represent fitting errors. (d) PL response to a 10 mVpp square wave bias modulating at 10 Hz, 100 Hz and 1kHz. (e) Frequency dependent PL response to 10 mVpp sinusoidal wave at 10 Hz to 80 kHz modulation. Error bars show the standard deviation across six runs. Solid red line represents equivalent circuit simulation using parameters obtained from EIS measurements. (f) PL response (bottom) to applied neuronal waveform bias (top).

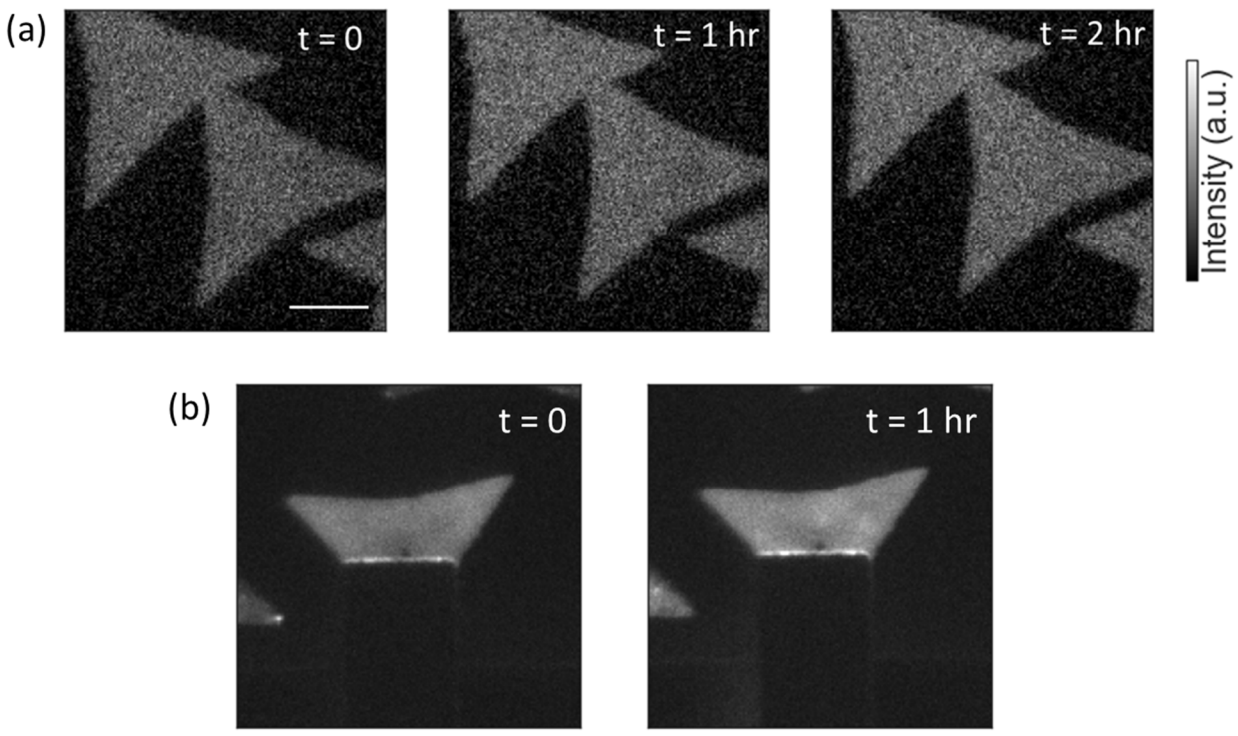

Figure 4.3: Photostability of monolayer MoS_2.
(a) From left to right, PL images of CVD grown MoS_2 on glass after 0, 1 and 2 hours of constant photo-illumination. Sample was illuminated using wide-field LED source filtered between 570-616 nm at 10 W/cm^2. Scale bar, 10 μm, (b) MoS_2 flake under constant voltage modulation between -5 mV and 5 mV at 1 Hz.

Next, we expanded this approach to demonstrate imaging capability with LED illumination and two-photon excitation. As a result of strongly bound 2D excitons, monolayer MoS_2 exhibits high absorption of visible photons with energies above the exciton resonance (660 nm).[103] This gives us a broad range of excitation wavelengths to work with. In this configuration, we illuminated MoS_2 flakes on a glass coverslip using an LED source through a 570-616 nm bandpass filter and 1.4 NA oil immersion objective. The PL images were captured by an EMCCD camera after a 634 nm long pass filter. To test the photostability of MoS_2 PL, we continuously illuminated the sample and measured the emission intensity (Figure 4.4a). The incident power was estimated to be 10 W/cm^2. The PL intensity did not decay over a period of two hours of constant light

exposure. In Figure 4.3b, we also subjected the sample to a constant voltage modulation at 1 Hz between -5 mV and 5 mV. We find that MoS_2 PL emission is highly resistant to photobleaching and photo-induced degradation, allowing for prolonged imaging duration with minimal phototoxicity to live cells. The single crystalline nature gives MoS_2 improved photostability and resistant to degradation compared to molecular dyes.[104]

Owing to its strong two-photon absorption,[105] monolayer MoS_2 is also luminescent under two-photon excitation. Two-photon excitation has been used to monitor neural activity both *in vitro* and *in vivo* due to suppressed background signal, deeper tissue penetration, reduced light scattering and minimized photobleaching.[106] Figure 4.4b shows two-photon fluorescence images of a single MoS_2 flake with an applied bias of -20 mV and 20 mV. The sample was excited at 1064 nm using a tunable ultrafast pulsed laser (Insight X3), with a pulse width of <120 fs and a repetition rate of 80 MHz. The emitted PL was collected by a water-immersion objective (NA = 0.8) and subsequently detected by a photomultiplier tube (PMT) through a 660/52 nm bandpass filter that covered the primary excitonic emission peak of monolayer MoS_2 (section 4.4.5). The two-photon PL response was consistent with that of the single-photon, with the emission intensity decreasing and increasing with positive and negative biases, respectively. The Galvo-Resonant scanner provided a maximum imaging frame rate of 400 Hz. Line scanning can be employed to further increase the frame rate for capturing higher frequency signals. We show in Figure 4.4c a kymograph of PL response under a 100 Hz square wave bias. The frame captures 40 ms (y-axis) of modulating PL signal (left) against a non-fluorescent substrate (right), with alternating bright and dark bands matching the switching voltages compared to the dark background. These results highlight the compatibility of MoS_2 PL to a range of excitation mechanisms and wavelengths.

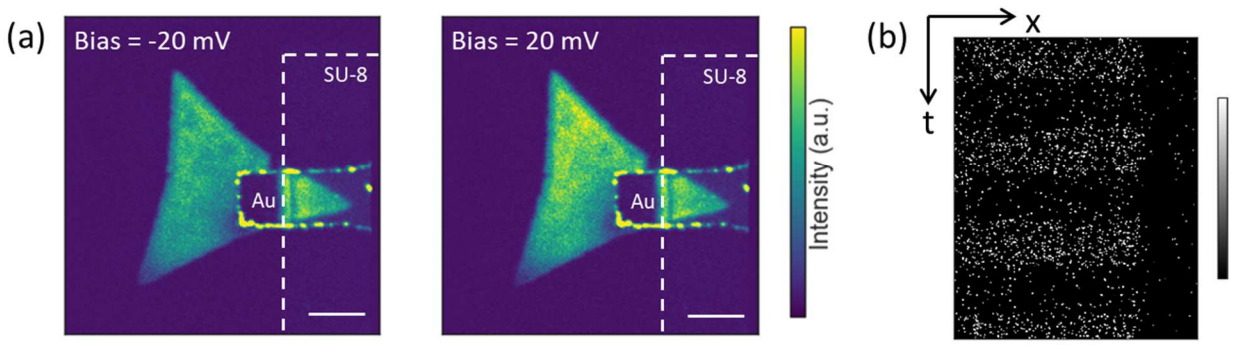

Figure 4.4: MoS_2 photoluminescence imaging.
(a) Two-photon PL image of monolayer MoS_2 flake under 20 mV (left) and -20 mV bias (right). (b) Kymographs or line scans showing 40 ms long snapshots of modulating two-photon PL against a non-fluorescent background. The bias is a square wave switching between -40 mV and 40 mV at 100 Hz.

Several studies have also shown MoS_2 nanosheets to be biocompatible with a variety of biological samples.[107–111] To evaluate the viability of cells on our sample, we dissociated and replated mature hiPSC-derived neuron cultures directly onto pre-fabricated MoS_2 on 22x22 mm glass coverslip (Figure 4.5a). To prepare a cell culture plate on the sample, we attached a 3D-printed 35 mm imaging dish with a 14 mm hole cut out using a UV curable optical adhesive (Figure 4.5b). The imaging dish was printed with biocompatible Acrylonitrile-Butadiene-Styrene (ABS) plastics. Neuronal cultures were derived from hiPSCs and differentiated for 4-5 weeks before dissociation and replating, following the procedures described in the method section of reference [112]. After replating, neurons were left to mature and reform connections on the sample for at least one week before imaging. Figure 4.5c shows an optical image of hiPSC-drived neurons on MoS_2 two weeks after replating. The culture exhibited typical morphology of neurons. We observed dense neuronal clustering and network connections, with axonal projections spanning across the substrate. MoS_2 flakes can be in the background where cell density is lower. Next, we evaluated the spontaneous activity of these neurons using a synthetic calcium indicator Oregon Green BAPTA-1 AM (OGB1, Figure 4.5d). Here, the imaging set up is an inverted epifluorescence

microscope with LED illumination filtered between 468-499 nm. The fluorescence signals were collected using a 514-557 nm band pass filter and captured on a sCMOS camera at 25 Hz. The culture was kept at room temperature throughout the imaging session. Neuronal cultures showed typical spontaneous calcium transients indicating that the neurons are healthy and viable on our MoS_2 platform (Figure 4.6).

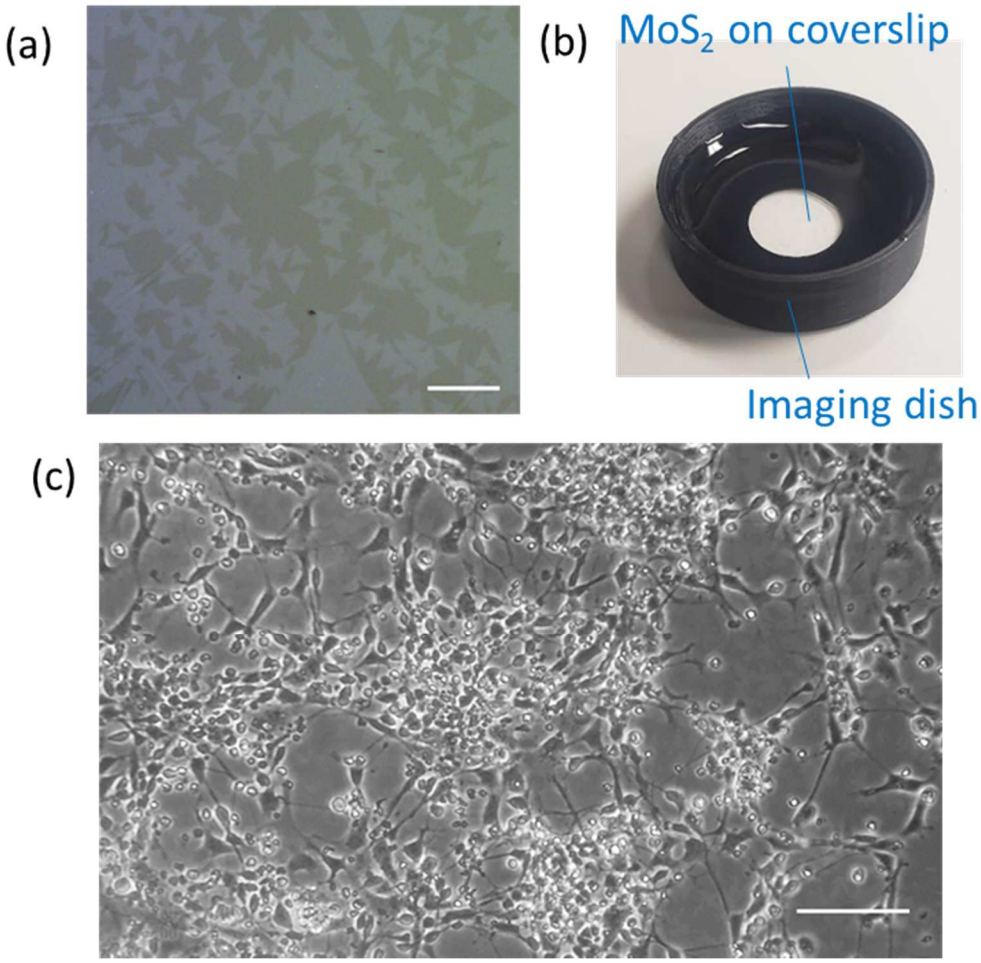

Figure 4.5: Biocompatibility of hiPSC-derived neurons on monolayer MoS_2.
(a) Optical image of transferred MoS_2 on glass coverslip. Scale bar, 40 µm, (b) 3D-printed imaging dish attached via UV curable optical adhesive to pre-fabricated monolayer MoS_2 on glass coverslip, (c) Neuron culture plated on MoS_2 after two weeks. Scale bar, 100 µm.

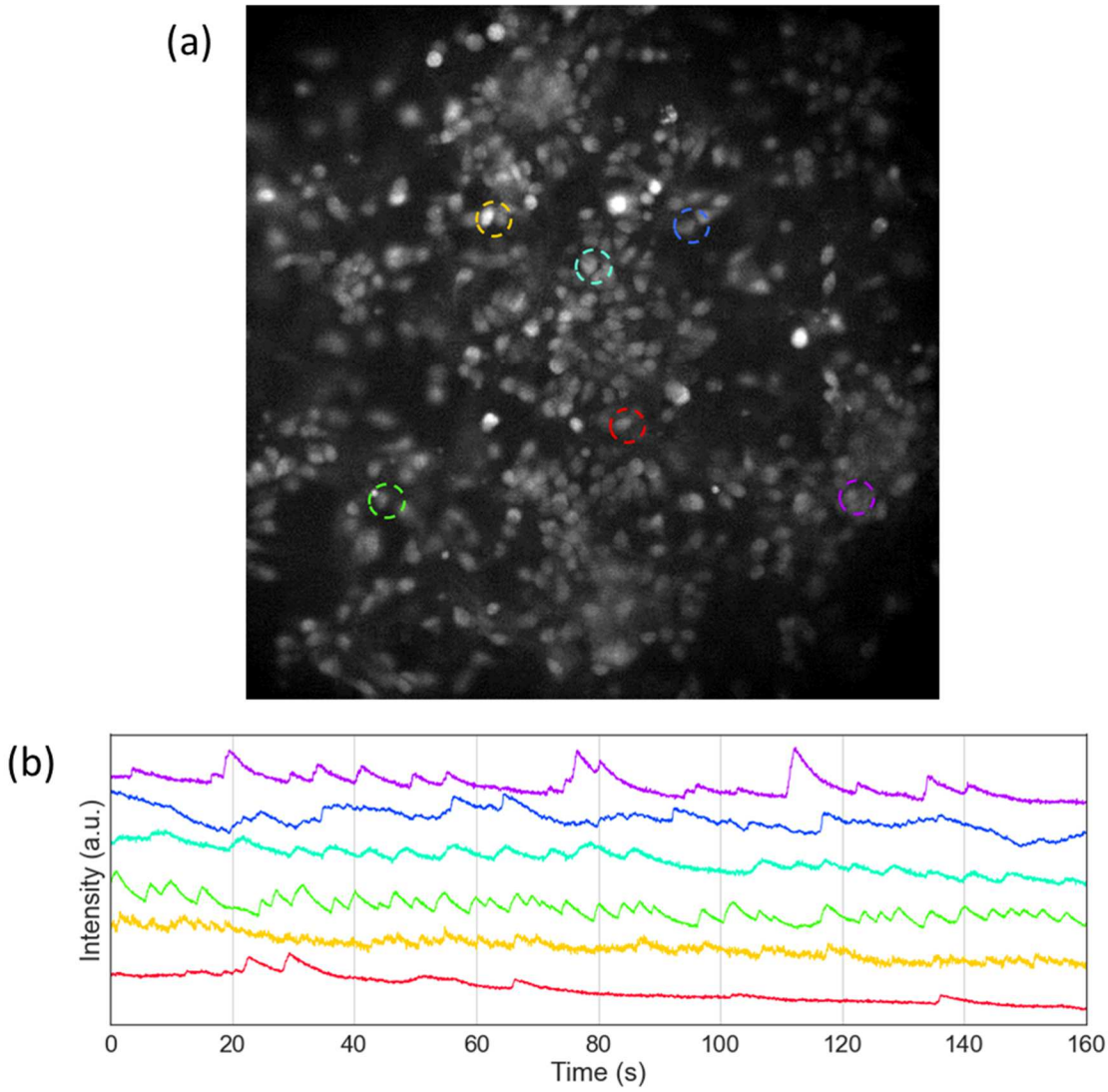

Figure 4.6: Assessment of neuron spontaneous activity using OGB1.
(a) OGB1 fluorescence image of neuronal network. Scale bar, 10 µm, (b) Calcium transients showing spontaneous neuronal activity, extracted from OGB1 fluorescence from regions highlighted in (a).

4.3 Conclusion

We present here a novel approach to label-free optical voltage sensing based on the PL emission of CVD-grown monolayer MoS_2. Light emission in monolayer MoS_2 originates from the radiative decay of photo-excited excitons and negative trions with different luminescent contributions depending on the surrounding charges. Because trion emission is much weaker, the

relative population of excitons and trions translates into the total PL emission by MoS_2. We leveraged this unique emission property to transduce voltage activity into optical signal. As a proof-of-principle work, we reported the excitonic PL's exceptional responsiveness to voltages, showing a large average fractional fluorescence change of 2% /mV or ~200% per 100 mV. The optical signal also exhibits picosecond response time that is reflected in the large temporal bandwidth of over 50 kHz. The use of material's inherent PL emission naturally provides fluorescence imaging capability and compatibility with a range of excitation sources and wavelengths. Lastly, we successfully maintained hiPSC-derived neuron cultures replated directly on MoS_2. Our findings showcase MoS_2 as a promising label-free optical platform for monitoring neural signals with good fluorescence contrast, temporal resolution, photostability and biocompatibility.

4.4 Methods

4.4.1 Au electrode fabrication and MoS_2 transfer

We first patterned Au electrodes on a 22x22 mm glass coverslip substrate. The coverslip was 170 μm thick, compatible with the oil immersion objective. We sputtered an adhesion layer of 5 nm Cr followed by 80 nm of Au films directly onto a clean coverslip. The sample was then patterned via photolithography using AZ1505 resists to define electrode area. After patterning, the unwanted Au/Cr areas became exposed and were etched away using Au and Cr etchants, producing a clean array of Au electrodes on the substrate. Next, we encapsulated most of the Au areas with a 4 μm thick layer of SU-8 using another photolithography step. This left us with insulated Au wires with exposed 10x10 μm^2 Au on one end for contacting MoS_2, and large pad for electrical connection on the other.

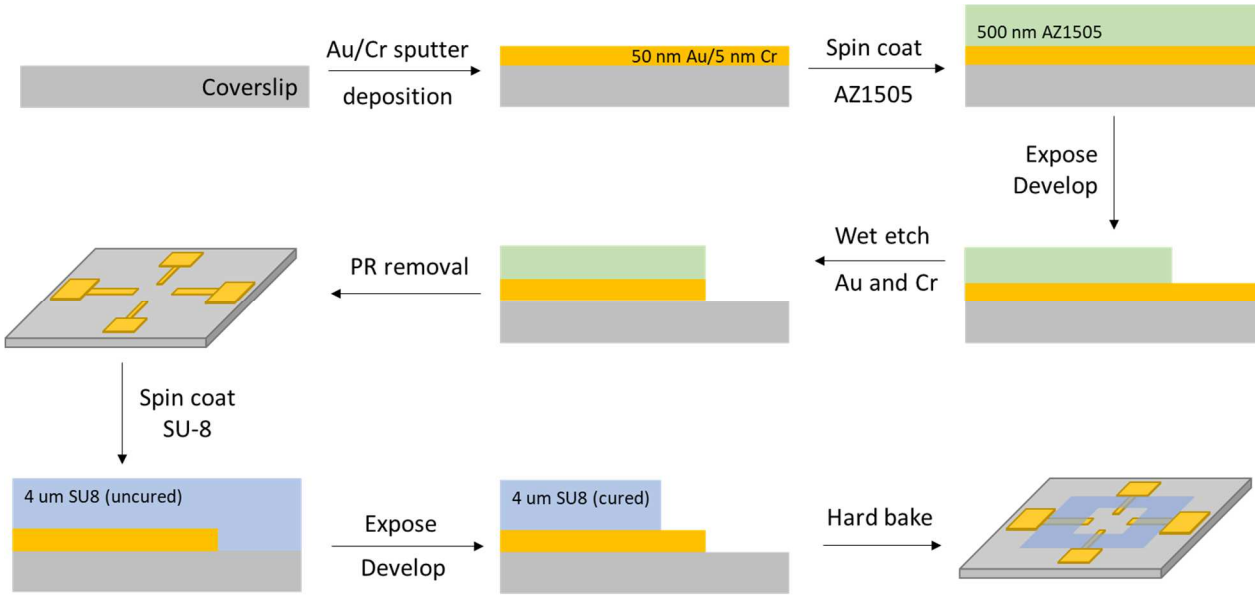

Figure 4.7: Fabrication of SU-8 encapsulated Au electrodes on glass coverslip.

CVD-grown MoS_2 flakes were transferred onto the prefabricated Au electrodes using a polymer-assisted process similar to that outlined in reference. We started with CVD-grown MoS_2 on SiO_2/Si purchased from 2D Semiconductors. We spun coat a thin layer of polystyrene (PS) film on top of the MoS_2 sample and left the film to completely dry for 5 minutes. The PS at the sample edges was gently scratched to remove PS edge bead and expose some underlying SiO_2. We then placed the sample to float in a hot 90°C 1M NaOH bath for 5-10 minutes. NaOH etched away the SiO_2 at the edges of the sample, opening small gaps between PS and the substrate. Once the edges of the PS started to detach, we transferred the sample to a DI water bath. The hydrophobic PS film should immediately delaminate, releasing MoS_2 flakes from the growth substrate. The floating MoS_2-containing PS film was transferred to float in two additional DI water baths to dissolve NaOH before finally being picked up by the target substrate. The sample was then heated at 80 °C for 5 minutes to evaporate residual water, and then at 120 °C for 1 hour to promote adhesion

between the PS/MoS_2 film and substrate. Finally, we dissolved the PS film in a toluene bath for 40 minutes. MoS_2 flakes were released from the PS film and remained on the substrate.

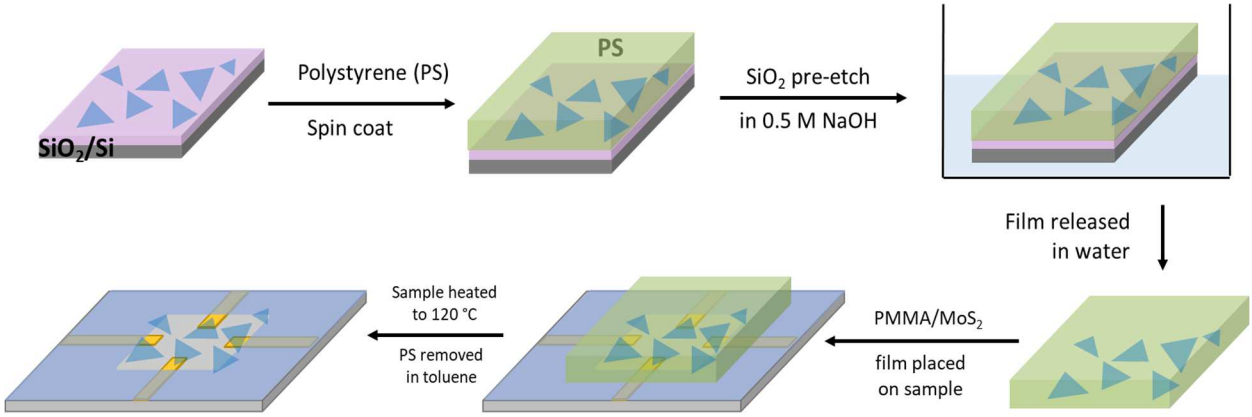

Figure 4.8: Transfer process of CVD-grown MoS_2.

4.4.2 MoS_2 photoluminescence in air and PBS

MoS_2 PL was measured before and after it was submerged in PBS (Figure 4.9). The monolayer was in contact with a prefabricated Au electrode. In PBS, the PL intensity significantly improved and the peak blue-shifted. This observation is consistent with electrostatic surface passivation of intrinsic MoS_2 defects, such as sulfur vacancies.[113] These defects are known to have n-doping effects on MoS_2. As an ionic liquid, PBS contains free ions that form an electric double layer on MoS_2 surface. Adsorption of ions results in reduced n-doping in MoS_2, which subsequently suppresses formation of trions upon photoexcitation. The higher exciton-to-trion ratio, therefore, increases the total PL emission intensity.

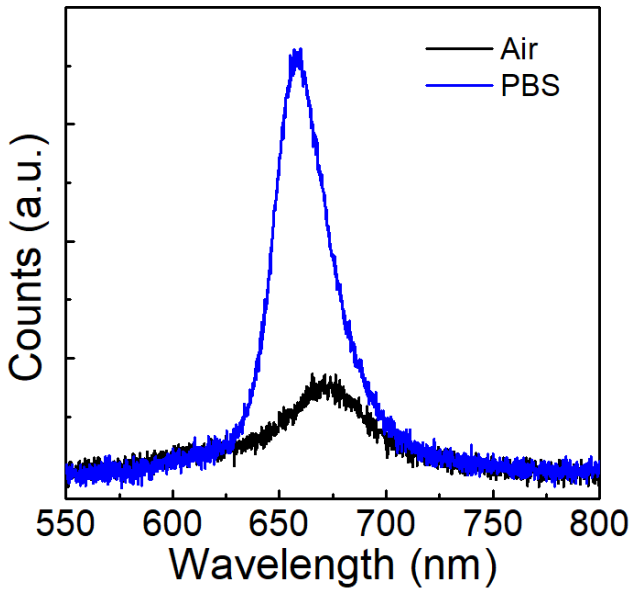

Figure 4.9: Photoluminescence spectrum of monolayer MoS_2 in air and PBS.

4.4.3 Photoluminescence modulation mechanism

We employed an electrochemical gating structure to apply an external voltage to MoS_2 (Figure 4.10). We used phosphate buffered saline as an ionic liquid containing Na^+, K^+, Cl^-, HPO_4^{2-} and H_2PO^{4-} ions. Voltage was applied between the Ag/AgCl electrode inserted into the solution, and a gold electrode in contact with MoS_2. When a positive bias is applied between the reference electrode and MoS_2, the positive ions in PBS are repelled away from the reference electrode and accumulated on top of MoS_2 surface. These charges attract more electrons into the flake and increase electron density. This then promotes trion formation and subsequently reduces total PL emission. And the opposite happens when a negative bias is applied. Negative ions are pushed towards MoS_2 surface, attracting more holes instead of electrons on to the material. As a result, trion formation is suppressed and the total PL emission increases.

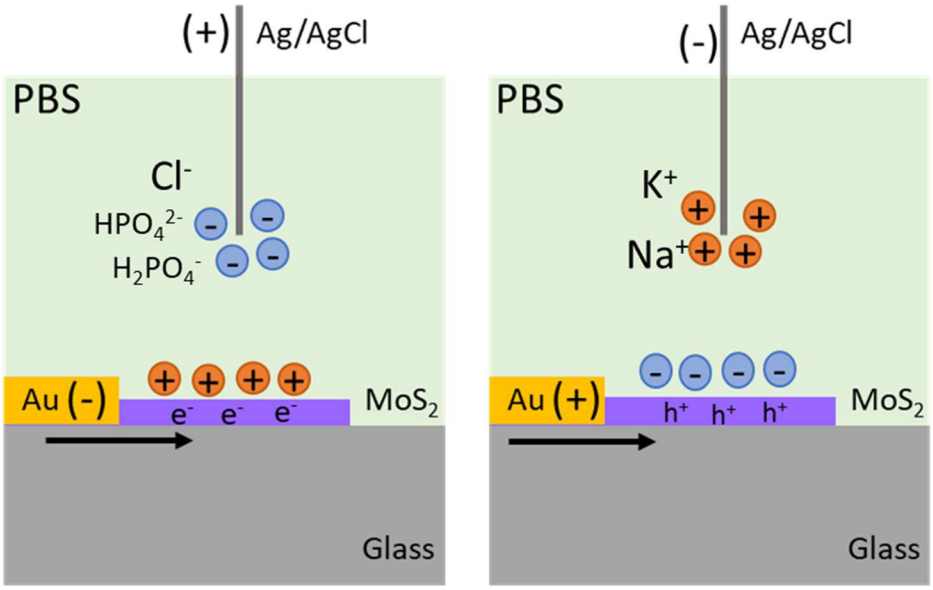

Figure 4.10: Photoluminescence modulation via electrochemical gating.

4.4.4 Estimation of voltage detection limit

The limit of detection can be calculated from the slope, α_V, in Figure 2b. For SNR = 1,

$$V_{LOD} = \left(\frac{1}{\alpha_V}\right)\frac{\Delta F}{F}\Big|_{noise} = \left(\frac{1}{\alpha_V}\right)\frac{NEP}{F_0} \quad \left[\frac{mV}{\sqrt{Hz}}\right] \tag{S-17}$$

where F_0 is the PL intensity, and NEP is the noise equivalent power of the PL signal that is made of the detector noise, NEP_0, and shot noise,

$$NEP = \sqrt{(NEP_0)^2 + 2h\nu F_0} \quad \left[\frac{W}{\sqrt{Hz}}\right] \tag{S-18}$$

To find NEP and NEP_0, we measured the PL signal and background noise in V using the APD at a sampling rate of 250 kS/s in V/√Hz. Assuming the photon energy at the PL peak, $h\nu$ = 1.88 eV, the conversion gain of the APD at 660 nm of 1.85×10^9 V/W, we calculated from equation S-2 the NEP and NEP_0 to be 7.0 fW/√Hz and 5.5 fW/√Hz, respectively. Using equation S-17 and the

slopes extracted from Figure 4.2c, we estimated the limit of detection to be 9.4 μV/√Hz for negative voltages and 13 μV/√Hz for positive voltages.

4.4.5 Imaging MoS_2 photoluminescence with two-photon excitation

For two-photon fluorescence microscopy (Figure 4.11), we used an ultrafast femtosecond pulsed laser (Insight X3) with a broad tuable range of 680-1300 nm. The pulse width is <120 fs with a repetition rate of 80 MHz. The input laser beam was modulated across the sample via Galvo-Resonant scanners at a maximum frame rate of 400 fps (Thorlabs). The sample was excited through a water-immersion objective (NA = 0.8) and emission was detected by photomultiplier tubes (PMT) through a 525/50 nm (channel A) and 660/52 nm (channel B) bandpass filters (Semrock).

For PL imaging, we chose an excitation wavelength of 1064 nm and incident power of about 10 mW. PL emission was collected in channel B filtered between 634-686 nm to cover the main exciton peak at around 660 nm. Figure 4.12a shows a two-photon PL image of a monolayer MoS_2 flake on an encapsulated Au electrode. Applying positive and negative biases results in a decrease and increase in emission intensity as shown in Figure 4.4a and Figure 4.12.

Because of the lack of inversion symmetry in monolayer MoS_2, the material has been shown to exhibit strong second-harmonic generation (SHG).[114,115] With an excitation wavelength of λ, SHG at λ/2 can be observed in channel A (500-550 nm) for 1000 nm<λ<1100 nm. Conveniently, emission peak of loaded OGB1 also falls within this range. We leveraged the spectral overlap of MoS_2 SHG and OGB-1 to simultaneously image live neurons and MoS_2. As shown in Figure 4.13a, we scanned the sample using 1000 nm excitation to image both neurons and MoS_2 in the same frame. The neuron cluster shows a significant spatial overlap with MoS2 flakes, proving the material's biocompatibility with neuron cultures. Next in Figure 4.13b, we

lowered the objective by 6 µm to focus on the plane of the substrate. This gives us an approximate vertical distance between the neuron layer and MoS_2.

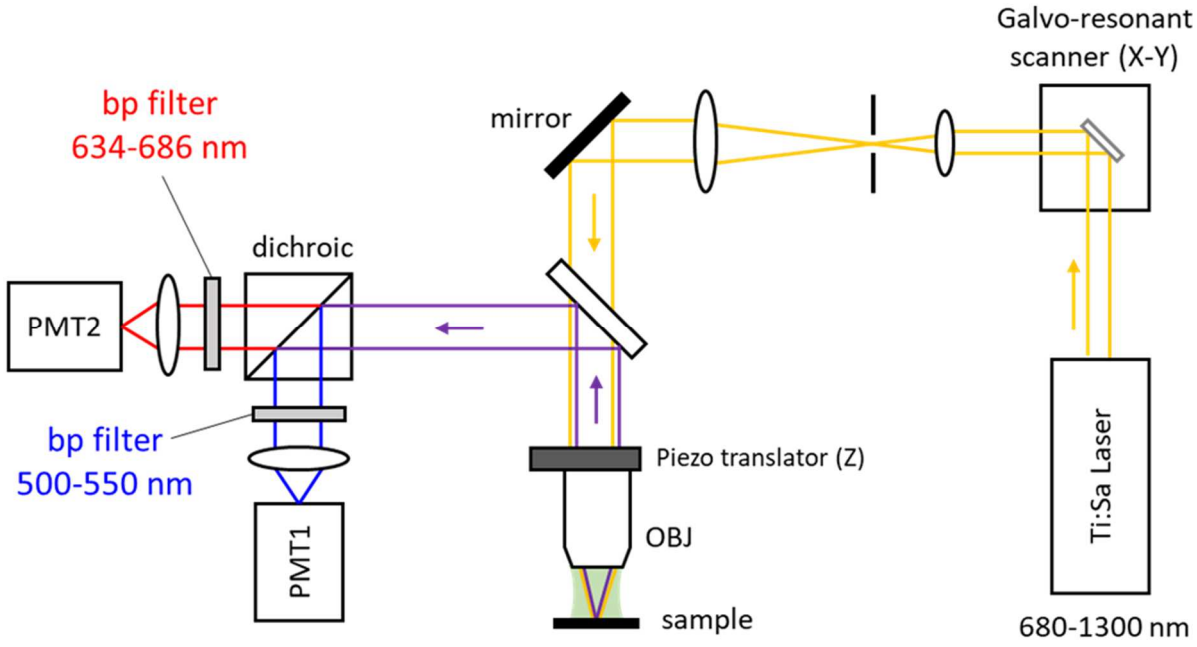

Figure 4.11: Two-photon microscopy set up.
OBJ – objective, PMT – photomultiplier tube, bp – band pass.

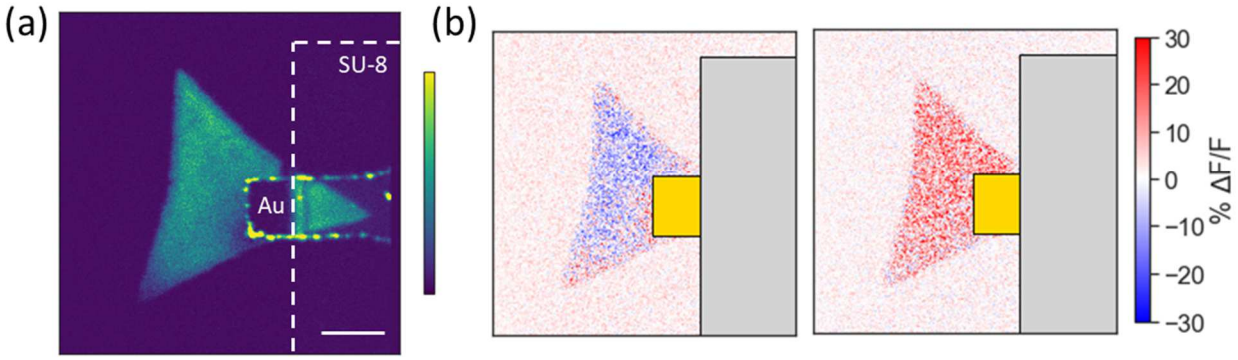

Figure 4.12: MoS_2 photoluminescence imaging and modulation with two-photon excitation.
(a) Two-photon PL image excited by 1064 nm pulsed laser measured between 634-686 nm. Scale bar, 10 µm. (b) PL change as upon application of +20 mV (left) and -20 mV (right) bias between submerged Ag/AgCl electrode and MoS_2.

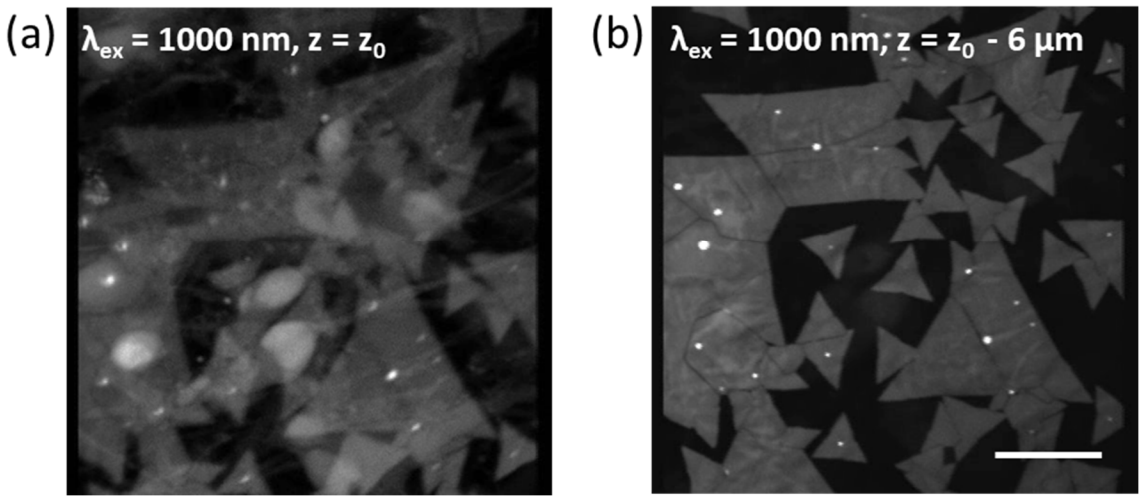

Figure 4.13: Imaging OGB1-loaded neurons and MoS_2 second harmonic generation. (a) OGB1 imaging and MoS_2 SHG using 1000 nm excitation, measured between 500-550 nm. (b) MoS_2 SHG obtained using the same imaging parameters but with a focal plane 6 um below that of (a). Scale bar, 20 µm.

4.4.6 Photoluminescence modulation without Au electrode

When MoS_2 is placed near an active neuron, its surface charge changes as the neuron generates a flow of positively charged ions across the cell membrane. We studied the effect of this local electric fields on the MoS_2 PL by utilizing a 2 µm monopolar platinum/iridium (Pt/Ir) microelectrode (MicroProbes) to generate an electrical impulse micrometers away from the MoS_2 surface. We first modeled the electric field distribution in this scenario using COMSOL Multiphysics. The simulation was set up in a 2D axisymmetric space with PBS filling the upper half space ($z>0$) and MoS_2/glass in the lower half. An electric potential of 40 mV was applied between the microelectrode tip ($r < 2$ µm) at a vertical distance h from MoS_2 and a reference potential placed at r = 500 µm. Figure 4.14b shows a simulated 2D potential map (color scale) and electric field distribution (arrows) produced by a microelectrode placed at h = 6 µm. On the MoS_2 surface ($z \approx 0$ µm), the electric fields are primarily out-of-plane. This suggests that the presence of the electrical impulse causes an accumulation of positive ions on the MoS_2 surface, which would

consequently induce a change in MoS_2's PL intensity. Experimentally, we used a micromanipulator to align the microelectrode tip to the center of a single MoS_2 flake, and a piezo actuator to control the height (h) of the electrode tip from the sample surface. We applied a 100 ms long 40 mV square pulse between the microelectrode and a Ag/AgCl electrode placed several millimeters away in the solution. As seen in Figure 4.14b, we measured the PL change as the vertical distance z varied between 1 and 20 μm. The voltage pulse resulted in an overall increase in the PL intensity, but the magnitude of the response decayed as the microelectrode moved away from the MoS_2 surface. The induced surface charge on the MoS_2 is proportional to the electric field due to the existence of EDL at the MoS_2/PBS interface. We can then calculate the normalized surface charge by taking the surface-average of electric field values right above the MoS_2 surface for different values of h. The simulated result is shown in red in Figure 4.14c and in good agreement with the experimental results.

In this microelectrode configuration (Figure 4.14a), we showed that MoS_2 PL could also be modulated without a direct electrical contact through ion adsorption at the MoS_2 surface. Other studies have also reported MoS_2 PL modification in an aqueous solution in response to the solution pH, citing the changing adsorbates and surrounding medium as the dominant factor.[116,117] When submerged in PBS, both cations and anions interact with MoS_2 and influence the formation of trion during photoexcitation. Cations are readily adsorbed on MoS_2 due to its negative surface charge from the atomic sulfur layer and sulfur vacancy sites.[118] Adsorption of cations effectively suppresses trion formation that results in enhanced PL emission. At the same time, anions can coordinate to Mo atoms and act as a n-doping reagent to facilitate trion formation.[119] This competition for adsorption sites ultimately determines the relative exciton and trion densities that control the PL emission intensity. Applying a positive voltage pulse through the microelectrode

causes cations to move towards MoS_2. This momentarily increases cation adsorption and subsequently PL emission intensity. We note that PL modulation via ion adsorption also occurs when MoS_2 is directly biased via a Au electrode, but the effect is outweighed by the movement of electrons as a result of electrochemical gating.

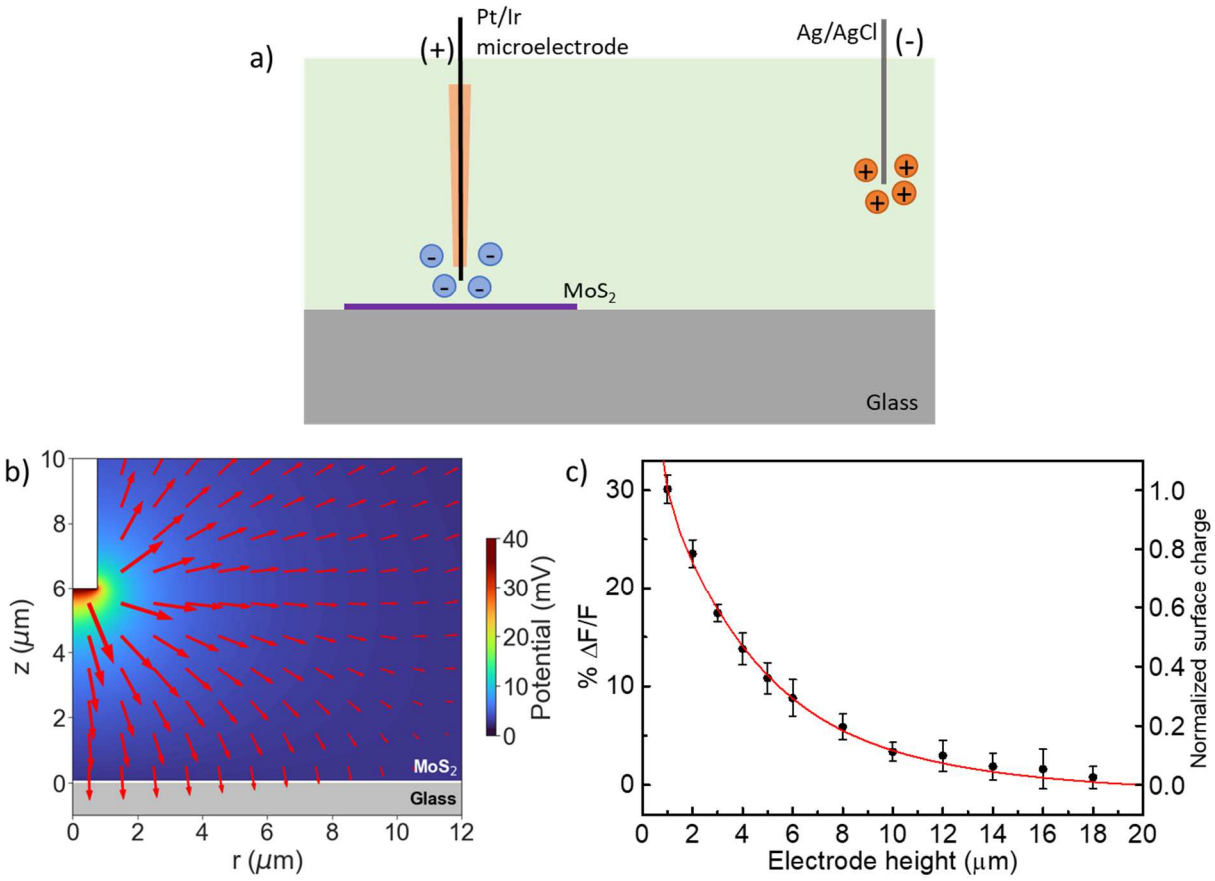

Figure 4.14: Photoluminescence modulation via local electric field.
(a) Photoluminescence modulation without electrical contact. Schematic shows a positive bias applied between Pt/Ir microelectode and Ag/AgCl. (b) COMSOL simulation of electric field and potential distributions induced by applying a 40 mV bias through a 2 µm microelectrode placed 6 µm above MoS_2, with respect to a reference potential placed at r = 500 µm. (c) PL response as a function of electrode height, h, to a 40 mV electrical impulse applied between the 2 µm Pt/Ir microelectrode and a Ag/AgCl reference electrode. Error bars represent the standard deviation of ten responses. Red solid line shows the normalized surface charge as a function of electrode height, which is proportional to the simulated averaged electric field at MoS_2.

4.4.7 Simulation of electric field and potential distribution using COMSOL Multiphysics

The distance between the electrode tip and the MoS_2 flake has a significant impact on how much PL can be changed with the applied voltage. To find out this dependence, we use Electric Currents Module in COMSOL Multiphysics to simulate the potential map and the electric field when an electrode tip is placed near the MoS_2 flake on top of a SiO_2 substrate. The simulation is performed in a 2D axisymmetric space. The upper space ($z>0$) is filled with PBS, whose electrical conductivity is 1.6 S/m and relative permittivity is 78.5. The electrode tip has radius of 0.75 um and electric potential of 40 mV at its bottom surface; the MoS_2 flake has radius of 20 um and is defined to have floating potential; the ground is at r = 500 um.

In the simulation, we sweep the distance h between the tip electrode and the MoS_2 flake from 0.5 um to 20 um with 0.5 um interval. Fig. a shows an example when h = 6 um. The floating potential of the flake is 2.6 mV in this case. The electrical field vectors are represented by red arrows in log scale, which are pointing from the electrode tip to the central part of the flake with a decreasing magnitude in the radial direction. Due to the existence of electric double layer at the MoS_2/PBS interface, the induced surface charge on the flake is proportional to the electrical field. Thus, we calculate the normalized surface charge by taking the surface-average of the electrical field that is very close to the MoS_2 flake. Simulated result is plotted in red line as shown in Figure 4.14b, which is in good agreement with the experimental result of PL measurement.

4.5 Acknowledgements

Chapter 4, in part, is currently being prepared for submission for publication of the material as it appears in Optical voltage sensing of electrophysiological signals with monolayer MoS_2. De-Eknamkul, Chawina; Kim, Jeonghoon; Huang, Wenzhuo; Ren, Yundong; Wilson, Madison; Puppo, Francesca; Patne, Meenashki; Muotri, Alysson R.; Kuzum, Duygu; Cubukcu, Ertugrul. The dissertation author and Jeonghoon Kim were the primary investigator and author of this material.

REFERENCES

1. Zhao, W. *et al.* Evolution of Electronic Structure in Atomically Thin Sheets of WS_2 and WSe_2. *ACS Nano* **7**, 791–797 (2013).

2. Splendiani, A. *et al.* Emerging photoluminescence in monolayer MoS_2. *Nano Lett.* **10**, 1271–1275 (2010).

3. Xiao, J., Zhao, M., Wang, Y. & Zhang, X. Excitons in atomically thin 2D semiconductors and their applications. *Nanophotonics* **6**, 1309–1328 (2017).

4. Chernikov, A. *et al.* Exciton binding energy and nonhydrogenic Rydberg series in monolayer WS2. *Phys. Rev. Lett.* **113**, 1–5 (2014).

5. Mak, K. F. *et al.* Tightly bound trions in monolayer MoS 2. *Nat. Mater.* **12**, 207–211 (2013).

6. Shang, J. *et al.* Observation of excitonic fine structure in a 2D transition-metal dichalcogenide semiconductor. *ACS Nano* **9**, 647–655 (2015).

7. Latini, S., Olsen, T. & Thygesen, K. S. Excitons in van der Waals heterostructures: The important role of dielectric screening. *Phys. Rev. B - Condens. Matter Mater. Phys.* **92**, 1–13 (2015).

8. Alpeggiani, F., Gong, S. H. & Kuipers, L. Dispersion and decay rate of exciton-polaritons and radiative modes in transition metal dichalcogenide monolayers. *Phys. Rev. B* **97**, 1–11 (2018).

9. Low, T. *et al.* Polaritons in layered two-dimensional materials. *Nat. Mater.* **16**, 182–194 (2017).

10. Zhang, X. *et al.* Guiding of visible photons at the angstrom thickness limit. *Nat. Nanotechnol.* **14**, 844–850 (2019).

11. Khurgin, J. B. Two-dimensional exciton–polariton—light guiding by transition metal dichalcogenide monolayers. *Optica* **2**, 740 (2015).

12. Liu, X. *et al.* Strong light-matter coupling in two-dimensional atomic crystals. *Nat. Photonics* **9**, 30–34 (2014).

13. Lundt, N. *et al.* Optical valley Hall effect for highly valley-coherent exciton-polaritons in an atomically thin semiconductor. *Nat. Nanotechnol.* **14**, 770–775 (2019).

14. Chen, Y. J., Cain, J. D., Stanev, T. K., Dravid, V. P. & Stern, N. P. Valley-polarized exciton-polaritons in a monolayer semiconductor. *Nat. Photonics* **11**, 431–435 (2017).

15. Schaibley, J. R. *et al.* Valleytronics in 2D materials. *Nat. Rev. Mater.* **1**, (2016).

16. Zhu, B., Zeng, H., Dai, J., Gong, Z. & Cui, X. Anomalously robust valley polarization and valley coherence in bilayer WS 2. (2014). doi:10.1073/pnas.1406960111

17. Gong, S. H., Alpeggiani, F., Sciacca, B., Garnett, E. C. & Kuipers, L. Nanoscale chiral valley-photon interface through optical spin-orbit coupling. *Science (80-.).* **359**, 443–447 (2018).

18. Jones, A. M. *et al.* Optical generation of excitonic valley coherence in monolayer WSe 2. **8**, 6–10 (2013).

19. Hao, K. *et al.* Direct measurement of exciton valley coherence in monolayer WSe 2. *Nat. Phys.* **12**, 677–682 (2016).

20. Sun, L. *et al.* Separation of valley excitons in a MoS 2 monolayer using a subwavelength asymmetric groove array. *Nat. Photonics* **13**, 180–184 (2019).

21. Yang, Z., Aghaeimeibodi, S. & Waks, E. Chiral light-matter interactions using spin-valley states in transition metal dichalcogenides. *Opt. Express* **27**, 21367 (2019).

22. Wang, S. *et al.* Coherent Coupling of WS $_2$ Monolayers with Metallic Photonic Nanostructures at Room Temperature. *Nano Lett.* **16**, 4368–4374 (2016).

23. Hunsperger, R. G. Integrated optics: Theory and technology: Sixth edition. *Integr. Opt. Theory Technol. Sixth Ed.* 1–513 (2009). doi:10.1007/b98730

24. Wang, S. S., Moharam, M. G., Magnusson, R. & Bagby, J. S. Guided-mode resonances in planar dielectric-layer diffraction gratings. *J. Opt. Soc. Am. A* **7**, 1470 (1990).

25. Wang, S. S. & Magnusson, R. Theory and applications of guided-mode resonance filters. *Appl. Opt.* **32**, 2606 (1993).

26. Zhang, X. *et al.* Guiding of visible photons at the ångström thickness limit. *Nat. Nanotechnol.* **14**, 844–850 (2019).

27. Zhao, W. *et al.* Evolution of electronic structure in atomically thin sheets of ws 2 and wse2. *ACS Nano* **7**, 791–797 (2013).

28. Berkdemir, A. *et al.* Identification of individual and few layers of WS2 using Raman Spectroscopy. *Sci. Rep.* **3**, 1–8 (2013).

29. Wolff, C., Busch, K. & Mortensen, N. A. Modal expansions in periodic photonic systems with material loss and dispersion. *Phys. Rev. B* **97**, 104203 (2018).

30. Castellanos-Gomez, A. *et al.* Laser-thinning of MoS 2: On demand generation of a single-layer semiconductor. *Nano Lett.* **12**, 3187–3192 (2012).

31. Hu, F. *et al.* Imaging exciton-polariton transport in MoSe 2 waveguides. *Nat. Photonics* **11**, 356–360 (2017).

32. Hu, F. *et al.* Imaging propagative exciton polaritons in atomically thin WSe2 waveguides. *Phys. Rev. B* **100**, 2–7 (2019).

33. Fan, S. & Joannopoulos, J. D. Analysis of guided resonances in photonic crystal slabs. *Phys. Rev. B - Condens. Matter Mater. Phys.* **65**, 1–8 (2002).

34. Magnusson, R., Wang, S. S., Black, T. D. & Sohn, A. Resonance Properties of Dielectric Waveguide Gratings: Theory and Experiments at 4-18 Ghz. *IEEE Trans. Antennas Propag.* **42**, 567–569 (1994).

35. Gaylord, T. K. & Moharam, M. G. Analysis and Applications of Optical Diffraction by Gratings. *Proc. IEEE* **73**, 894–937 (1985).

36. Norton, S. M., Erdogan, T. & Morris, G. M. Coupled-mode theory of resonant-grating filters. **14**, 629–639 (1997).

37. Castellanos-Gomez, A. *et al.* Deterministic transfer of two-dimensional materials by all-dry viscoelastic stamping. *2D Mater.* **1**, 011002 (2014).

38. Lu, J. *et al.* Improved photoelectrical properties of MoS2 films after laser micromachining. *ACS Nano* **8**, 6334–6343 (2014).

39. Venkatakrishnan, A. *et al.* Microsteganography on WS2 Monolayers Tailored by Direct Laser Painting. *ACS Nano* **11**, 713–720 (2017).

40. Sarkar, D. *et al.* MoS_2 field-effect transistor for next-generation label-free biosensors. *ACS Nano* **8**, 3992–4003 (2014).

41. Lee, J. *et al.* Two-dimensional layered MoS_2 biosensors enable highly sensitive detection of biomolecules. *Sci. Rep.* **4**, 7352 (2015).

42. Wang, L. *et al.* Functionalized MoS_2 nanosheet-based field-effect biosensor for label-free sensitive detection of cancer marker proteins in solution. *Small* **10**, 1101–1105 (2014).

43. Shan, J. *et al.* High sensitivity glucose detection at extremely low concentrations using a MoS_2-based field-effect transistor. *RSC Adv.* **8**, 7942–7948 (2018).

44. Radisavljevic, B., Radenovic, A., Brivio, J., Giacometti, V. & Kis, A. Single-layer MoS_2 transistors. *Nat. Nanotechnol.* **6**, 147–150 (2011).

45. Wang, Q. H., Kalantar-Zadeh, K., Kis, A., Coleman, J. N. & Strano, M. S. Electronics and optoelectronics of two-dimensional transition metal dichalcogenides. *Nat. Nanotechnol.* **7**, 699–712 (2012).

46. Jariwala, D., Sangwan, V. K., Lauhon, L. J., Marks, T. J. & Hersam, M. C. Emerging device applications for semiconducting two-dimensional transitional metal dichalcogenides. *ACS Nano* **8**, 1102–1120 (2014).

47. Mei, J. *et al.* Molybdenum disulfide field-effect transistor biosensor for ultrasensitive detection of DNA by employing morpholino as probe. *Biosens. Bioelectron.* **110**, 71–77 (2018).

48. Park, H. *et al.* Label-free and recalibrated multilayer MoS_2 biosensor for point-of-care diagnostics. *ACS Appl. Mater. Interfaces* **9**, 43490–43497 (2017).

49. Zhang, W., Ganesh, N., Block, I. D. & Cunningham, B. T. High sensitivity photonic crystal biosensor incorporating nanorod structures for enhanced surface area. *Sensors Actuators, B Chem.* **131**, 279–284 (2008).

50. Guo, Y. *et al.* Real-time small molecule binding detection using a label-free photonic crystal biosensor. *Anal. Chem. proceeding* **82**, 5211–5218 (2010).

51. Inan, H. *et al.* Photonic crystals: emerging biosensors and their promise for point-of-care applications. *Chem. Soc. Rev.* **46**, 366–388 (2017).

52. Butun, S. *et al.* Quantifying plasmon-enhanced light absorption in monolayer WS_2 films. *ACS Appl. Mater. Interfaces* **9**, 15044–15051 (2017).

53. Zhu, A. Y., Yi, F., Reed, J. C., Zhu, H. & Cubukcu, E. Optoelectromechanical multimodal biosensor with graphene active region. *Nano Lett.* **14**, 5641–5649 (2014).

54. Oh, J. *et al.* Carbon nanotube-based dual-mode biosensor for electrical and surface plasmon resonance measurements. *Nano Lett.* **10**, 2755–2760 (2010).

55. Lee, Y.-H. *et al.* Synthesis of large-area MoS_2 atomic layers with chemical vapor deposition. *Adv. Mater.* **24**, 2320–2325 (2012).

56. Smithe, K. K. H., Suryavanshi, S. V., Muñoz Rojo, M., Tedjarati, A. D. & Pop, E. Low variability in synthetic monolayer MoS_2 devices. *ACS Nano* **11**, 8456–8463 (2017).

57. Zhao, X. *et al.* Characterization of a computationally designed water-soluble human μ-opioid receptor variant using available structural information. *Anethesiology* **121**, 866–875 (2014).

58. Lerner, M. B. *et al.* Scalable production of highly sensitive nanosensors based on graphene functionalized with a designed G protein-coupled receptor. *Nano Lett.* **14**, 2709–2714 (2014).

59. Naylor, C. H. *et al.* Scalable Production of Molybdenum Disulfide Based Biosensors. *ACS Nano* **10**, 6173–6179 (2016).

60. Limonov, M. F., Rybin, M. V., Poddubny, A. N. & Kivshar, Y. S. Fano resonances in photonics. *Nat. Photonics* **11**, 543–554 (2017).

61. Wu, C. *et al.* Fano-resonant asymmetric metamaterials for ultrasensitive spectroscopy and identification of molecular monolayers. *Nat. Mater.* **11**, 69–75 (2011).

62. Yi, F. *et al.* Voltage tuning of plasmonic absorbers by indium tin oxide. *Appl. Phys. Lett.* **102**, (2013).

63. Tong, X., Ashalley, E., Lin, F., Li, H. & Wang, Z. M. Advances in MoS_2-based field effect transistors (FETs). *Nano-Micro Lett.* **7**, 203–218 (2015).

64. Xie, X. *et al.* Low-frequency noise in bilayer MoS_2 transistor. *ACS Nano* **8**, 5633–5640 (2014).

65. Schmidt, H. *et al.* Transport properties of monolayer MoS_2 grown by chemical vapour deposition. *Nano Lett.* **14**, 1909–1913 (2014).

66. Huang, M., Yanik, A. A., Chang, T. & Altug, H. Sub-wavelength nanofluidics in photonic crystal sensors. *Opt. Express* **17**, 24224–24233 (2009).

67. Ping, J. *et al.* All-electronic quantification of neuropeptide-receptor interaction using a bias-Free functionalized graphene microelectrode. *ACS Nano* **12**, 4218–4223 (2018).

68. Frederickson, R. C. Enkephalin pentapeptides--a review of current evidence for a physiological role in vertebrate neurotransmission. *Life Sci.* **21**, 23–42 (1977).

69. Chen, T. *et al.* Label-free detection of DNA hybridization using transistors based on CVD grown graphene. *Biosens. Bioelectron.* **41**, 103–109 (2013).

70. Liang, J. *et al.* Impact of post-lithography polymer residue on the electrical characteristics of MoS2 and WSe2 field effect transistors. *Adv. Mater. Interfaces* **6**, 1801321 (2019).

71. He, G. *et al.* Conduction mechanisms in CVD-grown monolayer MoS_2 transistors: from variable-range hopping to velocity saturation. *Nano Lett.* **15**, 5052–5058 (2015).

72. Wang, S. *et al.* Shape evolution of monolayer MoS_2 crystals grown by chemical vapor deposition. *Chem. Mater.* **26**, 6371–6379 (2014).

73. Late, D. J., Liu, B., Matte, H. S. S. R., Dravid, V. P. & Rao, C. N. R. Hysteresis in single-layer MoS_2 field effect transistors. *ACS Nano* **6**, 5635–5641 (2012).

74. Bornhorst, J. A. & Falke, J. J. *Purification of proteins using polyhistidine affinity tags*. *Methods in Enzymology* **326**, (2000).

75. Chen, Z. R., Irvine, R. J., Somogyi, A. A. & Bochner, F. Mu receptor binding of some commonly used opioids and their metabolites. *Life Sci.* **48**, 2165–2171 (1991).

76. Volpe, D. A. *et al.* Uniform assessment and ranking of opioid Mu receptor binding constants for selected opioid drugs. *Regul. Toxicol. Pharmacol.* **59**, 385–390 (2011).

77. Heak, J., Yung, I., Jin, D., Yeong, B. & Jang, M. Enhancement of protein detection performance in field-effect transistors with polymer residue-free graphene channel. *Carbon N. Y.* **62**, 312–321 (2013).

78. Lin, W.-H. *et al.* A direct and polymer-free method for transferring graphene grown by chemical vapor deposition to any substrate. *ACS Nano* **8**, 1784–1791 (2014).

79. Jun, J. J. *et al.* Fully integrated silicon probes for high-density recording of neural activity. *Nature* **551**, 232–236 (2017).

80. Grienberger, C. & Konnerth, A. Imaging Calcium in Neurons. *Neuron* **73**, 862–885 (2012).

81. Ledochowitsch, P. *et al.* On the correspondence of electrical and optical physiology in in vivo population-scale two-photon calcium imaging. *bioRxiv* 1–32 (2019). doi:10.1101/800102

82. Peterka, D. S., Takahashi, H. & Yuste, R. Imaging Voltage in Neurons. *Neuron* **69**, 9–21 (2011).

83. Garcia-Etxarri, A. & Yuste, R. Time for NanoNeuro. *Nat. Methods* **18**, 1287–1293 (2021).

84. Alfonso, F. S. *et al.* Label-free optical detection of bioelectric potentials using electrochromic thin films. *Proc. Natl. Acad. Sci. U. S. A.* **117**, 17260–17268 (2020).

85. Habib, A. *et al.* Electro-plasmonic nanoantenna: A nonfluorescent optical probe for ultrasensitive label-free detection of electrophysiological signals. *Sci. Adv.* **5**, (2019).

86. Wang, F. *et al.* Gate-variable optical transitions in graphene. *Science (80-.).* **320**, 206–209 (2008).

87. Horng, J. *et al.* Imaging electric field dynamics with graphene optoelectronics. *Nat. Commun.* **7**, 1–15 (2016).

88. Balch, H. B. *et al.* Graphene Electric Field Sensor Enables Single Shot Label-Free Imaging of Bioelectric Potentials. *Nano Lett.* **21**, 4944–4949 (2021).

89. Wang, H., Zhang, C. & Rana, F. Surface Recombination Limited Lifetimes of Photoexcited Carriers in Few-Layer Transition Metal Dichalcogenide MoS2. *Nano Lett.* **15**, 8204–8210 (2015).

90. Moody, G., Schaibley, J. & Xu, X. Exciton dynamics in monolayer transition metal dichalcogenides [Invited]. *J. Opt. Soc. Am. B* **33**, C39–C49 (2016).

91. Manzeli, S., Ovchinnikov, D., Pasquier, D., Yazyev, O. V. & Kis, A. 2D transition metal dichalcogenides. *Nat. Rev. Mater.* **2**, (2017).

92. Ross, J. S. *et al.* Electrical control of neutral and charged excitons in a monolayer semiconductor. *Nat. Commun.* **4**, 1–6 (2013).

93. Ross, J. S. *et al.* Electrical control of neutral and charged excitons in a monolayer semiconductor. *Nat. Commun.* **4**, 1473–1476 (2013).

94. Ramasubramaniam, A. Large excitonic effects in monolayers of molybdenum and tungsten

dichalcogenides. *Phys. Rev. B - Condens. Matter Mater. Phys.* **86**, 1–6 (2012).

95. Berghäuser, G. & Malic, E. Analytical approach to excitonic properties of MoS 2. *Phys. Rev. B - Condens. Matter Mater. Phys.* **89**, 1–6 (2014).

96. Mak, K. F. *et al.* Tightly bound trions in monolayer MoS 2. *Nat. Mater.* **12**, 207–211 (2013).

97. Wang, F. *et al.* Ionic Liquid Gating of Suspended MoS2 Field Effect Transistor Devices. *Nano Lett.* **15**, 5284–5288 (2015).

98. Li, Z., Chang, S. W., Chen, C. C. & Cronin, S. B. Enhanced photocurrent and photoluminescence spectra in MoS2 under ionic liquid gating. *Nano Res.* **7**, 973–980 (2014).

99. Perera, M. M. *et al.* Improved Carrier Mobility in. 4449–4458 (2013).

100. Jiang, J. *et al.* 2D electric-double-layer phototransistor for photoelectronic and spatiotemporal hybrid neuromorphic integration. *Nanoscale* **11**, 1360–1369 (2019).

101. Hong, J. *et al.* Exploring atomic defects in molybdenum disulphide monolayers. *Nat. Commun.* **6**, 1–8 (2015).

102. Lien, D. H. *et al.* Electrical suppression of all nonradiative recombination pathways in monolayer semiconductors. *Science (80-.).* **364**, 468–471 (2019).

103. Mukherjee, B. *et al.* Complex electrical permittivity of the monolayer molybdenum disulfide (MoS_2) in near UV and visible. *Opt. Mater. Express* **5**, 447 (2015).

104. Zhang, W., Matsuda, K. & Miyauchi, Y. Photostability of Monolayer Transition-Metal Dichalcogenides in Ambient Air and Acidic/Basic Aqueous Solutions. *ACS Omega* **4**, 10322–10327 (2019).

105. Li, Y. *et al.* Giant two-photon absorption in monolayer MoS2. *Laser Photonics Rev.* **9**, 427–434 (2015).

106. Stosiek, C., Garaschuk, O., Holthoff, K. & Konnerth, A. In vivo two-photon calcium imaging of neuronal networks. *Proc. Natl. Acad. Sci. U. S. A.* **100**, 7319–7324 (2003).

107. Wang, N. *et al.* Synthesis of strongly fluorescent molybdenum disulfide nanosheets for cell-targeted labeling. *ACS Appl. Mater. Interfaces* **6**, 19888–19894 (2014).

108. Wang, S. *et al.* Biocompatible PEGylated MoS2 nanosheets: Controllable bottom-up synthesis and highly efficient photothermal regression of tumor. *Biomaterials* **39**, 206–217 (2015).

109. Kaur, J. *et al.* Biological interactions of biocompatible and water-dispersed MoS2 nanosheets with bacteria and human cells. *Sci. Rep.* **8**, 1–15 (2018).

110. Shah, P., Narayanan, T. N., Li, C. Z. & Alwarappan, S. Probing the biocompatibility of

MoS2 nanosheets by cytotoxicity assay and electrical impedance spectroscopy. *Nanotechnology* **26**, (2015).

111. Carrow, J. K. *et al.* Photothermal modulation of human stem cells using light-responsive 2D nanomaterials. *Proc. Natl. Acad. Sci. U. S. A.* **117**, 13329–13338 (2020).

112. Puppo, F. *et al.* All-Optical Electrophysiology in hiPSC-Derived Neurons With Synthetic Voltage Sensors. *Front. Cell. Neurosci.* **15**, 1–11 (2021).

113. Atallah, T. L. *et al.* Electrostatic Screening of Charged Defects in Monolayer MoS2. *J. Phys. Chem. Lett.* **8**, 2148–2152 (2017).

114. Kumar, N. *et al.* Second harmonic microscopy of monolayer MoS2. *Phys. Rev. B - Condens. Matter Mater. Phys.* **87**, 1–6 (2013).

115. Malard, L. M., Alencar, T. V., Barboza, A. P. M., Mak, K. F. & De Paula, A. M. Observation of intense second harmonic generation from MoS2 atomic crystals. *Phys. Rev. B - Condens. Matter Mater. Phys.* **87**, 1–5 (2013).

116. Seki, T., Ihara, T., Kanemitsu, Y. & Hayamizu, Y. Photoluminescence of CVD-grown MoS2 modified by pH under aqueous solutions toward potential biological sensing. *2D Mater.* **7**, (2020).

117. Tezuka, S. *et al.* In situ bioimaging of Lactobacillus by photoluminescence of MoS2. *2D Mater.* **7**, (2020).

118. Bretscher, H. *et al.* Rational Passivation of Sulfur Vacancy Defects in Two-Dimensional Transition Metal Dichalcogenides. *ACS Nano* **15**, 8780–8789 (2021).

119. Li, Z. *et al.* Mechanistic insight into the chemical treatments of monolayer transition metal disulfides for photoluminescence enhancement. *Nat. Commun.* **12**, (2021).